
FLOWR.ROOT – A FLOW MATCHING BASED FOUNDATION MODEL FOR JOINT MULTI-PURPOSE STRUCTURE-AWARE 3D LIGAND GENERATION AND AFFINITY PREDICTION

Julian Cremer^{1,*}, Tuan Le¹, Mohammad M. Ghahremanpour², Emilia Slugocka^{3,6},
Filipe Menezes^{4,5,*}, Djork-Arné Clevert¹

¹Machine Learning & Computational Sciences, Pfizer Worldwide R&D, Berlin, Germany

²Computational Chemistry, Medicine Design, Pfizer Worldwide R&D, Cambridge, USA

³Doctoral School of Medical and Health Sciences, Jagiellonian University Medical College, Cracow, Poland

⁶Department of Physicochemical Drug Analysis, Faculty of Pharmacy, Jagiellonian University Medical College, Cracow, Poland

⁴Institute of Structural Biology, Molecular Targets and Therapeutics Center, Helmholtz Munich, Neuherberg, Germany

⁵TUM School of Natural Sciences, Department of Bioscience, Bayerisches NMR Zentrum,
Technical University of Munich, Garching, Germany

*Corresponding authors. Email: julian.cremer@pfizer.com, filipe.menezes@helmholtz-munich.de

ABSTRACT

We present FLOWR.ROOT, an $SE(3)$ -equivariant flow-matching model for pocket-aware 3D ligand generation with joint potency and binding affinity prediction and confidence estimation. The model supports *de novo* generation, interaction- and pharmacophore-conditional sampling, fragment elaboration and replacement, and multi-endpoint affinity prediction (pIC_{50} , pK_i , pK_d , pEC_{50}). Training combines large-scale ligand libraries with mixed-fidelity protein–ligand complexes, refined on curated co-crystal datasets and adapted to project-specific data through parameter-efficient finetuning. The base FLOWR.ROOT model achieves state-of-the-art performance in unconditional 3D molecule and pocket-conditional ligand generation, producing geometrically realistic, low-strain structures with high efficiency. On HiQBIND, the pre-trained and finetuned model demonstrates highly accurate affinity predictions, and outperforms recent state-of-the-art methods such as Boltz-2 on the FEP+/OpenFE benchmark with substantial speed advantages. However, we show that addressing unseen structure–activity landscapes requires domain adaptation; parameter-efficient LoRA finetuning yields marked improvements on diverse proprietary datasets and PDE10A. Joint generation and affinity prediction enable inference-time scaling through importance sampling, steering design toward higher-affinity compounds. Case studies validate this: selective CK2 α ligand generation against CLK3 shows significant correlation between predicted and quantum-mechanical binding energies. Scaffold elaboration on ER α , TYK2, and BACE1 demonstrates strong agreement between predicted affinities and QM calculations while confirming geometric fidelity. By integrating structure-aware generation, affinity estimation, property-guided sampling, and efficient domain adaptation, FLOWR.ROOT provides a comprehensive foundation for structure-based drug design from hit identification through lead optimization.

1 Introduction

Diffusion- and flow-based generative models have become central tools for learning complex data distributions and have recently enabled rapid progress in generative chemistry and structure-based drug design (SBDD) [Ho et al., 2020b, Song et al., 2021, Rombach et al., 2022, Lipman et al., 2023, Liu et al., 2022, Albergo and Vanden-Eijnden, 2023, Albergo et al., 2023, Hooeboom et al., 2022, Vignac et al., 2023, Le et al., 2023, Schneuing et al., 2023, Guan et al., 2023, Cremer et al., 2024, Abramson et al., 2024, Campbell et al., 2024, Irwin et al., 2024, Cremer et al., 2025]. One key subfield is pocket-conditional ligand generation, where $SE(3)$ -equivariant models generate ligands directly in the protein binding site [Schneuing et al., 2023, Guan et al., 2023]. Subsequent work has improved chemical validity and

pose quality and explored pre-training and inference-time guidance to steer sampling toward desired objectives [Le et al., 2023, Wang et al., 2024, Cremer et al., 2024]. Complementary to *de novo* design, fragment-based approaches support practical lead optimization; however, combining pocket conditioning with flexible fragment elaboration and editing (e.g., scaffold replacement or fragment growing under interaction constraints) within a single generative backbone remains challenging [Imrie et al., 2020, Voloboev, 2024, Zhang et al., 2024, Lee et al., 2025, Guo et al., 2023, Igashov et al., 2024, Cremer et al., 2025].

Beyond generation, the utility of proposed ligands depends on reliable potency and binding affinity prediction to prioritize candidates during iterative design. Classical scoring functions (e.g., docking) are computationally efficient but can be insufficiently accurate, whereas more elaborate physics-based methods such as FEP and ABFE are typically more reliable but too costly to apply at the scale of modern generative campaigns [Trott and Olson, 2010, Friesner et al., 2004, Jones et al., 1997, Wang et al., 2015, Mey et al., 2020, Mobley and Klimovich, 2012, Alibay et al., 2022, Feng et al., 2022a, Ries et al., 2024]. Machine learning scoring functions improve throughput but may suffer from dataset bias and limited generalization [Jiménez et al., 2018, Volkov et al., 2022, Valsson et al., 2025]. Co-folding approaches such as Boltz-2 can reach high accuracy on selected targets, but require structure prediction per query and, due to decoupled training, may limit co-adaptation between pocket geometry and affinity [Passaro et al., 2025].

These considerations motivate models that jointly learn (conditional) structure generation and affinity prediction in a protein pocket context. Joint modeling supports in-distribution ranking of generated structures and enables inference-time steering (e.g., via importance sampling) without relying on external scoring functions [Cremer et al., 2024]. At the same time, drug discovery campaigns are characterized by assay- and series-specific structure–activity relationships (SARs) that often differ from public training data. Consequently, strong benchmark performance does not necessarily translate to a new project without adaptation; efficient finetuning and, where appropriate, preference-based alignment [Schneuing et al., 2025], can help align the model to the relevant local SAR landscape.

Training such models is further constrained by the scarcity of high-quality protein–ligand complexes with reliable affinity annotations relative to ligand-only resources. This motivates multi-stage training strategies that exploit large-scale, lower-fidelity data to learn broad chemical and structural priors, followed by refinement on curated experimental datasets to improve structural accuracy and affinity prediction [Irwin et al., 2020, Bolton et al., 2011, Wang et al., 2005, 2025, Durairaj et al., 2024, Zhu et al., 2025, Backenköhler et al., 2024, Lemos et al., 2025].

In this work, we present FLOWR.ROOT, a foundational framework for structure-based generative chemistry designed to address the full continuum from large-scale pre-training through project-specific adaptation. The framework unifies *de novo*, interaction- and pharmacophore-, as well as fragment-conditioned ligand generation with multi-endpoint affinity prediction and per-sample confidence estimation—to our knowledge, the first model to jointly train these capabilities within a single architecture. FLOWR.ROOT employs a three-stage training strategy that systematically leverages datasets of varying fidelity: (1) large-scale pre-training on billions of ligands and millions of protein–ligand complexes with diverse affinity labels, (2) refinement on curated, higher-quality structural data, and (3) project-specific adaptation via parameter-efficient Low-Rank Adaptation (LoRA) [Hu et al., 2022] and multi-objective guidance through importance sampling. This joint training paradigm enables affinity prediction to actively shape the generative trajectory without reliance on external scoring functions, while supporting rapid adaptation to project-specific data distributions. The framework further introduces flexible fragment-conditional generation modes—including local fragment growing and replacement supporting spatially targeted modifications, while affinity-guidance allows to effectively sample and rank local chemical spaces. Together, these capabilities position FLOWR.ROOT as a comprehensive and continuously evolving companion throughout early-stage drug discovery campaigns, from hit identification through lead optimization.

2 Results

2.1 Overview of FLOWR.ROOT

FLOWR.ROOT is a unified framework for structure-based drug design that jointly trains pocket-aware 3D ligand generation with multi-endpoint affinity prediction and confidence estimation (Fig. 1). The framework addresses key challenges in computational drug discovery: generating chemically valid, geometrically realistic ligands within protein binding sites; accurately predicting potency and binding affinity across diverse assay types; supporting flexible generation modes from *de novo* design to targeted fragment modifications; and enabling efficient adaptation to project-specific structure-activity relationships. A comprehensive overview is given in Appendix A.

The model is built on an $SE(3)$ -equivariant flow matching backbone that learns a mixed continuous/discrete transport map, transforming a prior distribution (noise or fragment anchors for coordinates, uniform for categorical features) to the target ligand distribution within a given protein pocket. The architecture comprises two main components: a pocket encoder that processes full-atom protein features through equivariant self-attention layers, generating invariant and

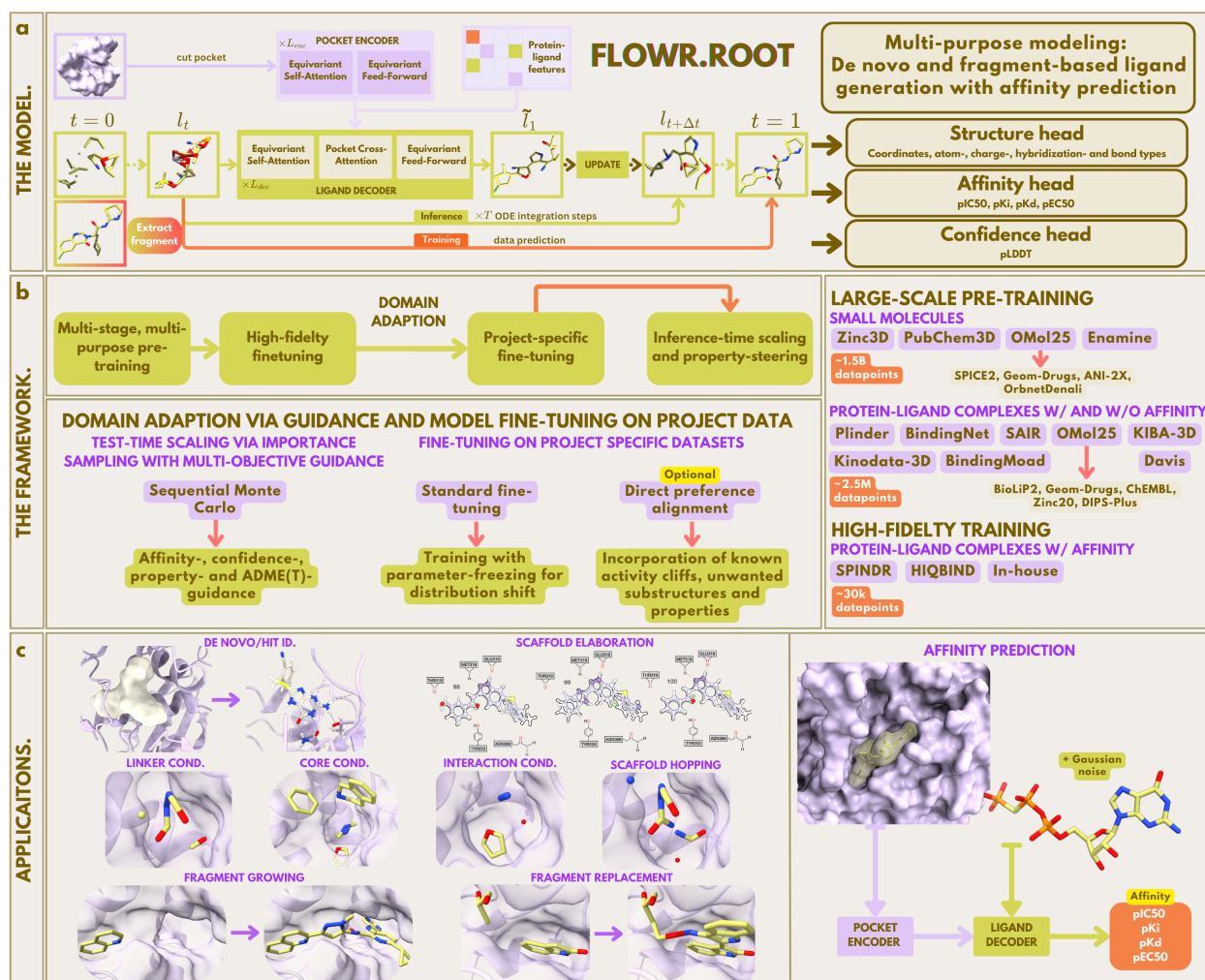


Figure 1: Overview of the FLOWR.ROOT framework for joint structure-aware ligand generation and affinity prediction. **a** The FLOWR.ROOT model is built on an $SE(3)$ -equivariant flow matching backbone that learns a transport map transforming noise (or fragment anchors) into ligand structures within protein pockets. The architecture comprises an equivariant pocket encoder processing protein pocket features, and a ligand decoder processing ligands, while ligand-pocket interactions are integrated via equivariant cross-attention. A structure head predicts atomic coordinates, atom types, bond orders, charges, and hybridization states, a multi-affinity head predicts affinity with separate predictors for pIC₅₀, pK_i, pK_d, and pEC₅₀, and a confidence head provides pLDDT-based uncertainty estimation. **b** The FLOWR.ROOT framework consists of three stages combining multi-stage training with finetuning and domain adaptation. Training follows a three-stage paradigm exploiting data of varying fidelity. Large-scale pre-training on ~ 1.5 B small molecule conformations is followed by training on mixed-fidelity ~ 2.5 M protein-ligand complexes with and without affinity labels. Then, the model is finetuned on curated high-fidelity co-crystal datasets to sharpen structural accuracy and affinity prediction, followed by project-specific domain adaptation through parameter-efficient finetuning, or direct preference alignment, and inference-time scaling via importance sampling with multi-objective guidance. **c** FLOWR.ROOT supports multiple ligand generation modes within a single backbone: ligand-only and pocket-conditional *de novo* generation, interaction/pharmacophore-conditional generation for preserving specific protein-ligand contacts, scaffold hopping and elaboration, and local fragment growing/replacement. Given a protein pocket and a bound ligand, FLOWR.ROOT can also be used to predict potency and binding affinity.

equivariant representations; and a ligand decoder that employs equivariant self-attention for intra-ligand dependencies followed by cross-attention to integrate pocket context. Protein pockets are extracted using a 7\AA cutoff radius around binding sites, balancing computational tractability with interaction coverage. The ligand decoder features three output heads that serve complementary purposes. The *structure head* predicts atomic coordinates, atom types, bond orders, partial charges, and hybridization states. The *multi-affinity head* comprises four separate predictors for pIC₅₀, pK_i, pK_d,

and pEC_{50} —explicitly avoiding treatment of heterogeneous affinity labels as interchangeable. The *confidence head* provides pLDDT-based uncertainty estimation for generated structures.

Training follows a three-stage paradigm that exploits data of varying fidelity to address the scarcity of high-quality experimental complexes: *Stage 1* builds broad generative priors across chemical and structural distributions. The model trains on $\sim 1.5\text{B}$ small molecule conformations (ZINC3D, PubChem3D, Enamine REAL, OMol25) for chemical coverage, and $\sim 2.5\text{M}$ mixed-fidelity protein-ligand complexes with and without affinity labels from both computational sources (BindingNet, SAIR, KIBA-3D, Davis-3D, Kinodata-3D) and experimental sources (Plinder, BindingMOAD). *Stage 2* adapts pre-trained weights to curated, drug-like datasets. We use SPINDR and HiQBind for multi-target finetuning, teaching the model fine details of protein-ligand interactions and binding affinity from high-quality co-crystal structures. *Stage 3* bridges the gap between public data and project-specific structure-activity landscapes through multiple strategies: inference-time scaling via importance sampling guides generation toward desired properties (affinity, ADME/T, synthetic accessibility); parameter-efficient finetuning enables rapid adaptation while avoiding catastrophic forgetting. This multi-stage paradigm addresses a fundamental limitation: strong benchmark performance does not guarantee generalization to novel structure-activity landscapes. Real-world drug discovery requires understanding nuanced SAR across related molecules within specific binding sites—richness uniquely captured by dense bioactivity data that differs substantially from sparse public datasets. Rather than expecting universal generalization, FLOWR.ROOT is designed as an adaptive companion that refines through sustained interaction with project-specific data.

The model is trained using mean squared error (MSE) loss for coordinates and categorical cross-entropy (CE) losses for atom types, charges, hybridization, and bond types. In addition, we introduce explicit geometric supervision through bond length and bond angle losses. The bond length loss penalizes deviations in predicted inter-atomic distances for bonded pairs. The bond angle loss uses Huber loss over valid angle triplets to preserve local molecular geometry while remaining robust to outliers. These auxiliary losses significantly reduce strain energies in generated structures. For training the affinity head, invariant and equivariant features from ligand, pocket, and their interactions via the ligand decoder’s latent representations are extracted, and gated equivariant blocks combine invariant and equivariant tensors, followed by multi-layer perceptrons (MLPs) that produce aggregated ligand, pocket, and interaction embeddings. Task-specific heads then predict each affinity type separately, with Huber loss for robust training. This design explicitly models the distinct experimental setups underlying IC_{50} , K_i , K_d , and EC_{50} measurements rather than treating them as interchangeable.

FLOWR.ROOT supports multiple generation modes within a single backbone, enabling flexible application across hit identification and lead optimization: (1) *de novo* pocket-conditional generation for exploring novel chemical matter; (2) *interaction/pharmacophore-conditional* generation for preserving or enforcing specific protein-ligand contacts; (3) *scaffold hopping and elaboration* for core and R-group replacement; and (4) *local fragment growing and replacement* for targeted structural modifications. For the latter two modes, we use a flexible prior placement strategy that shifts the generative prior from the zero center-of-mass to the local replacement site, enforcing locality in partial modifications and enabling precise control over which atoms to replace while preserving the remainder of the molecule. In addition, FLOWR.ROOT supports inference-time steering via importance sampling to sample from conditional distributions allowing for single- and multi-objective optimization without retraining, for example, steering toward higher predicted affinities while maintaining sample diversity.

To train FLOWR.ROOT, we leveraged a diverse collection of datasets. A detailed description of all datasets used in this work, including preprocessing and curation pipelines, dataset statistics, and chemical space analyses, is provided in Appendix A.5. In short, all protein-ligand complexes undergo rigorous preprocessing using Schrödinger’s LigPrep and PrepWizard, including protonation state determination at physiological pH, protein preparation with side chain completion, and constrained minimization. Protein pockets are extracted using a 7\AA cutoff radius around reference ligands. Crucially, if not stated otherwise, throughout all protein-ligand datasets we kept a consistent dataset split following the provided Plinder [Durairaj et al., 2024] train, validation and test set splits to avoid data leakage. Plinder employs comprehensive similarity metrics (protein sequence, pocket-level Jaccard, interaction-level PLIP, and ligand-level Tanimoto) to ensure minimal leakage and high-quality, non-redundant testing. To our knowledge, this represents the most rigorous publicly available splitting strategy for structure-based modeling.

2.2 Unconditional and Pocket-Conditional Generation

We first establish the improvements conferred by the architectural changes incorporated into FLOWR.ROOT. To this end, we demonstrate the expressiveness of the ligand decoder backbone for unconditional 3D molecule generation on the well-established GEOM-DRUGS dataset, comparing against recent state-of-the-art models including EQGAT-DIFF [Le et al., 2023], SEMLAFLOW [Irwin et al., 2024], ADiT [Joshi et al., 2025], MEGALODON [Reidenbach et al., 2024], and FLOWMOL3 [Dunn and Koes, 2025]. Here, our non-pretrained base model, FLOWR.ROOT^{base}, achieves 0.94 ± 0.02 PoseBusters-validity (mean), surpassing all baselines including the recently released FLOWMOL3

Table 1: **Evaluation and comparison of FLOWR.ROOT with PILOT and FLOWR on SPINDR.** Benchmark comparison of the non-pretrained FLOWR.ROOT^{base} model against FLOWR and the diffusion-based PILOT model on the SPINDR test dataset. We sample 100 ligands per target across models. The evaluation includes PoseBusters-validity (PB-valid), strain energy calculated using GenBench3D, and AutoDock-Vina scores (kcal/mol). Additionally, we report the Wasserstein distance of the generated ligands’ bond angles (BondA.W1), bond lengths (BondL.W1) and dihedral angles (DihedralW1) distributions relative to those in the SPINDR test set. Ligand sizes for all models are sampled uniformly with a -10%/+10% margin around the respective reference ligand size. All values are mean values across ligands and targets and we denote standard deviations across targets as subscripts.

MODEL	PB-VALID \uparrow	STRAIN ENERGY \downarrow	VINA SCORE \downarrow	VINA SCORE ^{MIN} \downarrow	BONDA.W1 \downarrow	BONDL.W1 [10 ⁻²] \downarrow	DIHEDRALW1 \downarrow
PILOT	0.79 \pm 0.21	120.10 \pm 71.61	-6.30 \pm 0.96	-6.68 \pm 1.07	1.82	0.42	5.52
FLOWR	0.93 \pm 0.22	90.05 \pm 52.18	-6.93 \pm 0.92	-7.22 \pm 0.92	1.08	0.35	3.88
FLOWR.ROOT ^{BASE}	0.97 \pm 0.10	50.36 \pm 34.59	-7.52 \pm 0.84	-7.71 \pm 0.85	0.60	0.43	3.62
TEST SET	0.99 \pm 0.04	43.27 \pm 41.85	-7.69 \pm 0.00	-7.88 \pm 0.00	-	-	-

model (0.92 \pm 0.07), with a median relaxation energy of 3.65 \pm 0.2 kcal/mol and a median relaxation RMSD of only 0.07 \pm 0.02 Å—demonstrating high geometric precision. Complete benchmark results and comparisons are provided in Table 3.

For pocket-conditional ligand generation, we benchmark on CROSSDOCKED2020, where FLOWR.ROOT^{base} achieves a mean PoseBusters-validity of 0.97 \pm 0.22 and a mean strain energy of 67.13 \pm 53.05 kcal/mol, which both is substantially lower than all competing models, including FLOWR (mean PoseBusters-validity of 0.92 \pm 0.22 and mean strain energy of 87.83 \pm 74.30 kcal/mol) as well as the next best model PILOT (mean PoseBusters-validity of 0.83 \pm 0.33 and strain energy of 110.48 \pm 87.47 kcal/mol), and the highest mean AutoDock-Vina score of -7.76 \pm 0.55 kcal/mol (vs. -6.29 \pm 1.56 and -5.73 \pm 1.72 kcal/mol). Complete benchmark results and comparisons are provided in Table 4.

2.3 Pocket-Conditional Ligand Generation: SPINDR

Next, we evaluate FLOWR.ROOT’s ability to generate valid, physically plausible ligands, but on the more challenging test set of the SPINDR dataset. We compare the non-pretrained FLOWR.ROOT^{base} model with FLOWR and the diffusion-based PILOT model. Table 1 reveals that FLOWR.ROOT^{base} significantly outperforms both FLOWR and PILOT across all metrics. FLOWR.ROOT^{base} achieves a mean PoseBusters-validity of 0.97 \pm 0.10, nearing the test set reference (0.99 \pm 0.04). Additionally, the strain energy statistics significantly decreases to 50.36 \pm 34.59 kcal/mol, further demonstrating the model’s ability to generate chemically valid and energetically favorable ligands. FLOWR.ROOT^{base} also performs better in docking accuracy, with a mean Vina score of -7.52 \pm 0.84 kcal/mol.

In addition, we analyzed a wide range of complementary metrics (Table 5). FLOWR.ROOT^{base} achieves 100% novelty (1.00 \pm 0.00) with high diversity (0.83 \pm 0.10) and uniqueness (0.89 \pm 0.18) rates, comparable to FLOWR, while demonstrating consistent and substantial performance improvements across fragment-conditional generation modes, including scaffold hopping and pharmacophore-conditional generation.

2.4 Affinity prediction: HIQBIND

A central part of FLOWR.ROOT is its joint structure–affinity modeling. In Fig. 2 we provide a detailed analysis of affinity prediction performance on the HIQBIND test set. The affinity head of FLOWR.ROOT provides accurate predictions across various affinity types, including pIC₅₀, pK_i, and pK_d. For pIC₅₀, the model achieves a Pearson correlation of 0.92 \pm 0.03 and an R² of 0.85 \pm 0.06, while for pK_i and pK_d we get Pearson correlations of 0.76 \pm 0.13 and 0.57 \pm 0.20, respectively. When aggregating predictions across all affinity types (median), the model achieves RAE 0.58 \pm 0.06, RMSE 1.18 \pm 0.18, R² 0.57 \pm 0.10, Kendall τ 0.60 \pm 0.06, and Pearson 0.76 \pm 0.07. Note, reported values are mean values across four seed runs \pm the mean 95% confidence interval (CI) across seeds. These results confirm that the affinity head, trained jointly with structure generation, provides accurate and reliable potency estimates with robust performance across different experimental affinity labels. Probing the FLOWR.ROOT^{base} model trained solely on HIQBIND without pre-training, we observe substantially worse performance across all metrics with RAE 0.70 \pm 0.13, RMSE 1.95 \pm 0.24, R² 0.39 \pm 0.13, Kendall τ 0.49 \pm 0.09, and Pearson 0.63 \pm 0.10 underlining the importance of the proposed large-scale pre-training pipeline. Note, in both cases we strictly follow the Plinder dataset split minimizing information leakage between train and test also when pre-training.

Beyond predictive accuracy, FLOWR.ROOT enables property-guided generation via inference-time steering. Fig. 3 illustrates the effect of importance sampling-based steering on the predicted affinity distribution of generated ligands on the HIQBIND test set. Without guidance, the mean predicted pIC₅₀ is 5.60 \pm 1.11. As the steering duration increases

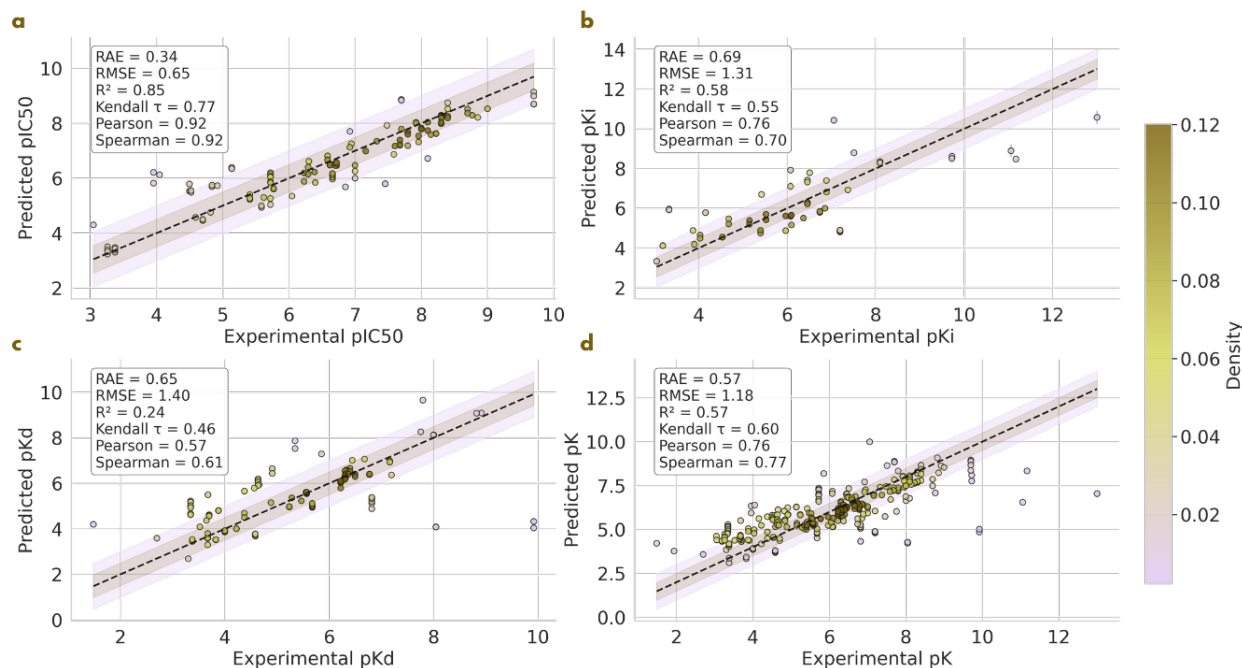


Figure 2: **Affinity prediction performance of FLOWR.ROOT on the HIQBIND test dataset** Correlation plot of FLOWR.ROOT-predicted pIC₅₀ vs. experimental pIC₅₀ binding affinities across protein-ligand complexes on the HIQBIND test set (based on Plinder splits), with shaded regions indicating 0.5 and 1 kcal/mol error boundaries, respectively, and color denoting density of predictions (the darker the denser). Error bars are reported as standard deviations from four seed runs. **a** Correlation with experimental pIC₅₀ affinities. **b** Correlation with experimental pK_i affinities. **c** Correlation with experimental pK_d affinities, and **(d)** shows the correlation results if the median of all predicted affinities is used.

(from 0.3 to 0.5 of the trajectory), the mean predicted pIC₅₀ shifts progressively to higher values (5.75, 5.84, 6.02), while the standard deviation remains stable. This demonstrates that the model can be effectively biased toward predicted higher-affinity ligands during generation.

In Fig. 3, we show the distribution of important chemical properties comparing unguided with guided (0.5 steering duration) samples across targets on the HIQBIND test set. While the distribution of SA scores shows a slight decrease towards lower scores for guided samples, we find that the overall druglikeness increases substantially with a mean Lipinski score of 4.30 ± 1.04 for the unguided to 4.68 ± 0.65 for the guided samples. Interestingly, we find that guidance consolidates the sample space, leading to mostly more compact distributions. This can also be seen in the chemical space comparison in Fig. 3b–c, where we overlay the chemical spaces of the un-guided and guided samples using both PCA and UMAP on molecular fingerprints.

Lastly, we also analyze geometric validity and sample diversity as steering intensity increases. For unguided versus guided samples, we observe a mean PoseBusters-validity of 0.93 ± 0.20 versus 0.91 ± 0.22 , mean strain energy of 48.46 ± 32.29 versus 54.42 ± 36.17 kcal/mol, mean Vina score of -7.41 ± 0.86 vs. -7.50 ± 0.85 , and mean per-target diversity of 0.79 ± 0.09 versus 0.79 ± 0.10 . While we observe a slight decrease in PoseBusters-validity and increase in strain energies, the diversity of the samples remains the same, so we can rule out a potential mode collapse when using guidance. In addition, we see a slight decrease in Vina scores on guided samples, demonstrating that we can maintain physically realistic structures while optimizing for affinity.

2.5 Affinity prediction: SCHRODINGER FEP+ AND OPENFE

Next, we evaluate the performance of the affinity prediction module of FLOWR.ROOT using the Schrodinger FEP+/OpenFE IndustryBenchmark datasets [OpenFE, a], comparing FLOWR.ROOT to state-of-the-art methods. These benchmarks offer a robust test of the model’s prediction capabilities with experimentally determined binding affinities across various targets and affinity types for protein-ligand complexes.

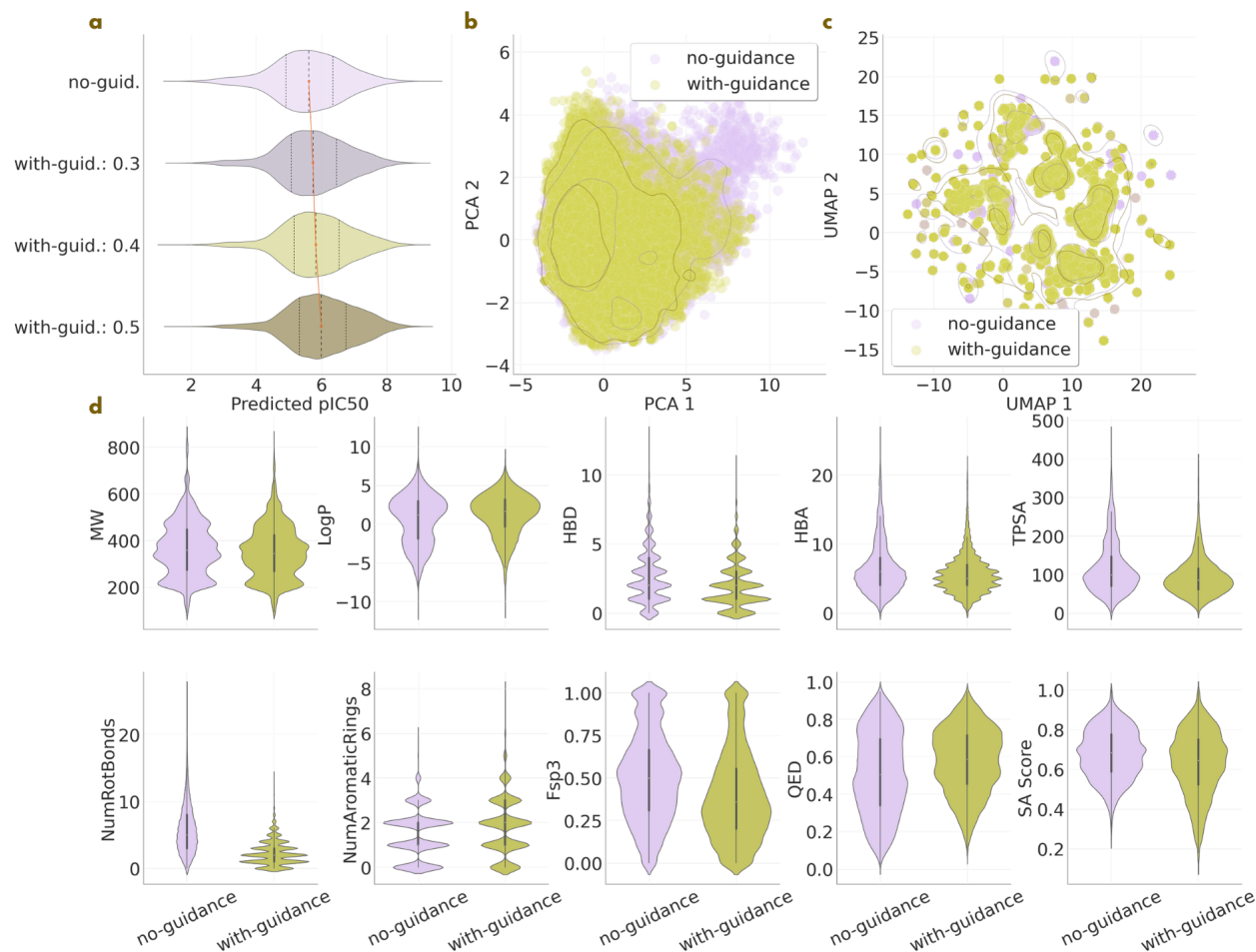


Figure 3: **Evaluation of FLOWR.ROOT on inference-time steering performance using affinity-guided importance sampling on the HIQBIND test dataset.** **a** Comparing the distribution of pIC_{50} predictions of generated ligands across test set targets between un-guided, and mild to strongly guided steering (0.3-0.5 guidance strength). **b** Depiction of chemical space comparison between un-guided and guided samples (0.5) via PCA analysis showing first two principal components. **c** Depiction of chemical space comparison between un-guided and guided samples (0.5) via 2D UMAP analysis. **d** Distribution comparison between un-guided and guided samples (0.5) regarding different chemical properties, namely molecular weight (MW), $\log P$, number of hydrogen donors (HBD) and acceptors (HBA), topological surface area (TPSA), number of rotatable bonds (NumRotBonds) and aromatic rings (NumAromaticRings), fraction of sp^3 carbons (Fsp3), druglikeness (QED) and synthesizability (SA Score).

In Fig. 4a, we present the scatter plot for FLOWR.ROOT-predicted combined affinity predictions (median over pK_d , pK_i , and pIC_{50}) versus experimental binding affinities. The plot indicates strong correlation with minimal deviation, suggesting that FLOWR.ROOT can successfully predict binding affinities across a broad range of protein-ligand complexes. In Fig. 4b, we show the performance of FLOWR.ROOT using various error and correlation metrics in comparison to OpenFE, FEP+, AEV-PLIG and Boltz-2. FLOWR.ROOT achieves an RMSE of 0.93 ± 0.05 kcal/mol, with a Pearson correlation of 0.86 ± 0.02 and a Kendall τ of 0.65 ± 0.03 . These results surpass those of FEP+ (RMSE = 0.83 ± 0.04 , Pearson = 0.76 ± 0.03) and OpenFE (RMSE = 1.19 ± 0.08 , Pearson = 0.66 ± 0.04), as well as those of Boltz-2 (Kendall τ = 0.46, Pearson = 0.62) and AEV-PLIG (RMSE = 1.35, Kendall τ = 0.36). Note, reported values for FLOWR.ROOT are mean values across four seed runs \pm the mean 95% CI. For FEP+ and OpenFE, the mean \pm 95% CI is shown [OpenFE, b], while Boltz-2 and AEV-PLIG do not provide confidence intervals.

FLOWR.ROOT outperforms physics-based models, namely OpenFE and FEP+, on almost all error and correlation metrics and significantly outperforms recent state-of-the-art ML-based models AEV-PLIG and Boltz-2 across all metrics. Notably, FLOWR.ROOT achieves this while being 3x faster than AEV-PLIG, 200x faster than Boltz-2, and over 10000x faster than OpenFE and FEP+. However, we also want to emphasize that the Schrodinger FEP+/OpenFE dataset is likely significantly overlapping with the training data in terms of ligand and target space. While this applies to

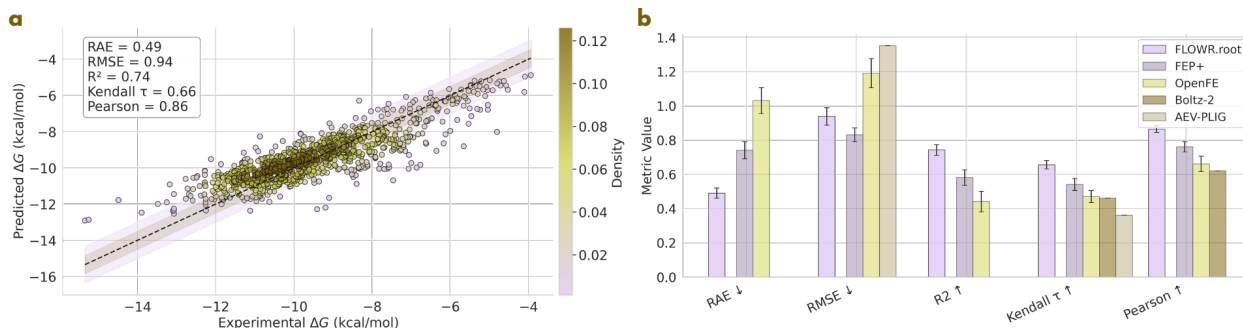


Figure 4: **Affinity prediction performance of FLOWR.ROOT on the FEP+/OpenFE Industry Benchmark dataset.** **a** Correlation plot of FLOWR.ROOT-predicted binding affinities as median over pK_d , pK_i and pIC_{50} in kcal/mol and respective correlation mean values, with shaded regions indicating 0.5 and 1 kcal/mol error boundaries, and color denoting density of predictions (the darker the more dense), vs. experimental binding affinities across protein-ligand complexes. Error bars are reported as standard deviations from four seed runs. **b** Mean values of different correlation metrics with error bars indicating the 95% confidence interval comparing FLOWR.ROOT with FEP+, OpenFE, AEV-PLIG and Boltz-2.

AEV-PLIG and Boltz-2 as well allowing for a somewhat fair comparison, we do not expect these results to indicate significant generalization capabilities.

2.6 Domain Adaptation via Finetuning: In-House Data

Next, we investigate the performance of FLOWR.ROOT on proprietary project-specific data. We evaluate four diverse pharmaceutical projects spanning inflammatory and neurodegenerative disease, to oncology, each encompassing distinct protein targets and ligand chemical spaces ranging from conventional small molecules to molecular degraders. Dataset sizes vary across projects: Project 1 comprises 1,073 compounds, Project 2 contains 730 compounds, Project 3 includes 229 compounds, and Project 4 contains 618 compounds. Projects 1–3 are annotated with pIC_{50} values, while Project 4 uses pEC_{50} measurements.

Pharmaceutical projects typically generate substantially more bioactivity data than co-crystal structures. To leverage existing assay data, we developed a structure generation workflow using OpenEye’s docking tools [OpenEye Scientific Software, d]. Measured compounds were first matched to existing co-crystal ligands via maximum common substructure (MCS) alignment and assigned to protein structures with the highest MCS similarity. Depending on the TanimotoCombo similarity between the query molecule and reference ligand (threshold $TC \geq 1.5$, computed via ROCS overlays [OpenEye Scientific Software, b] on up to 800 Omega-generated conformers [OpenEye Scientific Software, a]), we employed either Hybrid or ShapeFit docking. Docked poses were subsequently minimized using OpenEye’s Szybki with the ff14sb force field [Maier et al., 2015, OpenEye Scientific Software, c], and poses with positive interaction energies were discarded. The top pose was selected based on RMSD to the reference ligand.

We evaluate both Boltz-2 and FLOWR.ROOT in zero-shot settings on held-out test sets comprising 100 randomly selected complexes per project (80 for Project 3 due to its smaller size), with the remaining samples used for training and validation. As shown in Fig. 5a–b, both models fail to generalize to these unseen bioactivity spaces, yielding negligible or negative correlations between predicted and experimental potencies. Specifically, Boltz-2 yields strongly negative R^2 across all projects; for FLOWR.ROOT, R^2 values are -1.58 ± 0.64 (Project 1), -0.67 ± 0.45 (Project 2), -0.10 ± 0.26 (Project 3), and -0.13 ± 0.12 (Project 4). These results highlight a fundamental limitation: zero-shot generalization across arbitrary structure–activity landscapes is unrealistic given the inherent complexity of structure–activity relationships.

However, FLOWR.ROOT distinguishes itself through its capacity for straightforward yet effective finetuning, enabling adaptation to the underlying data distribution and improved modeling of the structure–activity landscape. We finetuned the model using Low-Rank Adaptation (LoRA) [Hu et al., 2022], where weight updates are parameterized as $\Delta W = BA$ with $B \in \mathbb{R}^{d \times r}$ and $A \in \mathbb{R}^{r \times k}$, using rank $r = 16$ and scaling factor $\alpha = 32$. This configuration yields approximately 3.3M trainable parameters, representing approximately 9% of the full model weights. Models were trained for 200 epochs with validation on 50 held-out samples. Since our proprietary datasets comprise pIC_{50} - and pEC_{50} -annotated data points, only the respective affinity head and the backbone were finetuned.

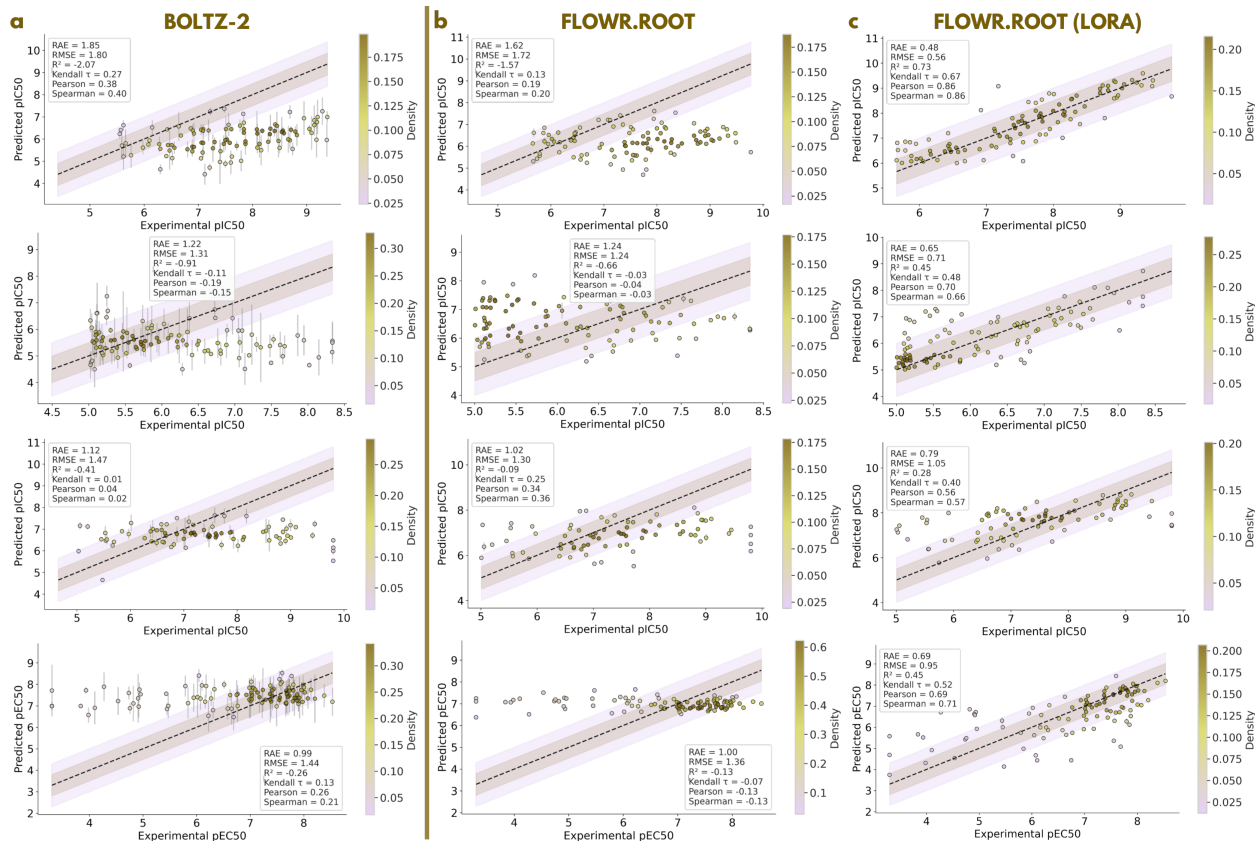


Figure 5: Evaluation of the affinity prediction performance of FLOWR.ROOT on a diverse set of unseen in-house structure—activity datasets with and without LoRA-finetuning. We evaluate and compare Boltz-2, FLOWR.ROOT and LoRA-finetuned FLOWR.ROOT on root absolute error (RAE), root mean squared error (RMSE), R-squared (R^2), Kendall τ , Pearson and Spearman correlation. Each dot in the scatter denotes the mean value extracted from two (Boltz-2) and four seed runs (FLOWR.ROOT). Error bars denote the respective standard deviation. Each row corresponds to a different project (Projects 1–4), spanning distinct protein targets of distinct therapeutic areas, ligand spaces (from small molecules to degraders), and structure-activity relationship (SAR) landscapes. Dataset sizes range from 229 to 1,073 compounds with pIC_{50} (Projects 1–3) or pEC_{50} (Project 4) annotations. **a** Boltz-2 predictions. **b** Zero-shot FLOWR.ROOT predictions. **c** LoRA-finetuned FLOWR.ROOT predictions.

As shown in Fig. 5c, LoRA-finetuned FLOWR.ROOT achieves strong performance across all four projects: Project 1 ($R^2 = 0.73 \pm 0.11$, Pearson $r = 0.86 \pm 0.05$), Project 2 ($R^2 = 0.45 \pm 0.21$, Pearson $r = 0.70 \pm 0.12$), Project 3 ($R^2 = 0.28 \pm 0.16$, Pearson $r = 0.56 \pm 0.13$), and Project 4 ($R^2 = 0.45 \pm 0.20$, Pearson $r = 0.69 \pm 0.11$). All reported values denote mean values across four seed runs \pm the mean 95% CI.

These findings underscore a critical observation: while achieving broad coverage of chemical space through ligand generation presents manageable challenges (see Fig. 15 and Fig. 16), generalizing across structure–activity landscapes constitutes a fundamentally more complex problem. The consistent success of LoRA-finetuned FLOWR.ROOT across four therapeutically and chemically distinct projects, and both IC_{50} and EC_{50} endpoints—combined with the failure of both Boltz-2 and FLOWR.ROOT to generalize despite strong public benchmark performance, supports our position that SBDD models should function as adaptive tools requiring calibration to project-specific SAR patterns. Thus, rather than expecting models to generalize universally from a single training phase, continuous refinement should be regarded as an integral component of the discovery process. Model utility grows through sustained interaction with project-specific data, positioning generative models as adaptive companions rather than standalone tools.

2.7 Domain Adaptation via Finetuning: PDE10A Benchmark

Next, to complement our in-house validation, we evaluate on the publicly available PDE10A benchmark dataset introduced by Tosstorff et al. [2022]. This high-quality dataset comprises 1,162 Phosphodiesterase-10A (PDE10A)

Table 2: **Evaluation of the affinity prediction performance of FLOWR.ROOT with and without LoRA-finetuning on PDE10A.** Benchmark comparison on the PDE10A dataset [Tosstorff et al., 2022] comprising 1,162 inhibitors with experimentally determined pIC_{50} values. We adapt the four split strategies: random split and three temporal splits (2011, 2012, 2013) that assess prospective prediction capability. Results compare the 2D3D hybrid method from Tosstorff et al. [2022], Boltz-2, zero-shot FLOWR.ROOT, and LoRA-finetuned FLOWR.ROOT. We report root mean squared error (RMSE) as well as Spearman correlation (Spear.) metrics following [Tosstorff et al., 2022]. Subscripts denote 95% bootstrap confidence intervals.

MODEL	RANDOM		TEMP. 2011		TEMP. 2012		TEMP. 2013	
	RMSE	SPEAR.	RMSE	SPEAR.	RMSE	SPEAR.	RMSE	SPEAR.
2D3D HYBRID	0.85 \pm .11	0.72 \pm .07	0.81 \pm .07	0.57 \pm .09	1.25 \pm .14	0.56 \pm .12	0.95 \pm .15	0.61 \pm .18
BOLTZ-2	0.85 \pm .09	0.75 \pm .07	0.83 \pm .07	0.59 \pm .08	0.73 \pm .09	0.83 \pm .06	0.95 \pm .22	0.74 \pm .15
FLOWR.ROOT	1.14 \pm .11	0.67 \pm .08	0.94 \pm .10	0.64 \pm .09	1.03 \pm .12	0.68 \pm .11	1.03 \pm .22	0.70 \pm .16
FLOWR.ROOT ^{LoRA}	0.32 \pm .06	0.97 \pm .01	0.33 \pm .06	0.93 \pm .03	0.43 \pm .10	0.93 \pm .04	0.44 \pm .16	0.95 \pm .04

inhibitors with experimentally determined IC_{50} values, curated from a former Roche PDE10A project with consistent assay conditions. The benchmark includes multiple evaluation strategies: a random split and three temporal splits (2011, 2012, 2013) that partition compounds by date, thereby simulating realistic prospective prediction scenarios encountered in drug discovery campaigns.

Table 2 presents results comparing the 2D3D hybrid QSAR method from Tosstorff et al. [2022], Boltz-2, zero-shot FLOWR.ROOT, and LoRA-finetuned FLOWR.ROOT. LoRA-finetuned FLOWR.ROOT consistently achieves the best performance across all splits and metrics. On the random split, LoRA finetuning yields $RMSE = 0.31 \pm 0.06$ and $Spearman = 0.96 \pm 0.01$, substantially outperforming Boltz-2 and the 2D3D hybrid method. Importantly, this strong performance is maintained on the more challenging temporal splits that assess prospective prediction capability: for temporal 2013, LoRA-finetuned FLOWR.ROOT achieves $RMSE = 0.44 \pm 0.17$ and $Spearman = 0.95 \pm 0.04$

Note, the 2D3D HYBRID approach proposed in Tosstorff et al. [2022] is a trained model on the respective split. Further, PDE10A is a well-studied target, thus is present in public databases and likely overlaps with Boltz-2’s comprehensive training data, making this an unreliable evaluation of true generalization. Nevertheless, these results further demonstrate and underline the effectiveness of parameter-efficient domain adaptation via LoRA finetuning within the FLOWR.ROOT framework, consistently transforming unreliable zero-shot predictions into accurate affinity estimates. In Fig. 16 and Fig. 17, we demonstrate the fragment growing mode of LoRA-finetuned FLOWR.ROOT applied to a co-crystal structure (PDB ID: 5SF4) from the PDE10A dataset. The generated ligands are annotated with affinity predictions to enable subsequent ranking and selection, illustrating the potential utility of our proposed framework in structure-based drug design workflows.

2.8 Case studies

To demonstrate the practical utility and versatility of FLOWR.ROOT for structure-based drug design, we present three case studies that systematically evaluate different aspects of the framework’s capabilities. First, we investigate multi-objective optimization through a kinase selectivity study, where we simultaneously maximize binding affinity for the on-target kinase $CK2\alpha$ while minimizing off-target activity against CLK3. This case study demonstrates how FLOWR.ROOT can address one of the most challenging aspects of kinase drug discovery—achieving selectivity among structurally homologous ATP-binding sites.

Second, we benchmark the framework’s conditional ligand generation performance against quantum mechanical binding energy calculations using TYK2 kinase, $ER\alpha$ and BACE1 as model systems. These validation studies assess the correlation between FLOWR.ROOT-predicted binding affinities and computationally demanding QM binding energies, while providing mechanistic insights into the structural features that govern binding affinity in the generated ligands.

2.9 Ligand Selectivity: $CK2\alpha$ and CLK3

The human kinome consists of over 500 kinases [Manning et al., 2002] that share conserved catalytic domain structures, particularly in their ATP-binding sites, where most competitive inhibitors bind. This structural homology, while functionally important for cellular signaling pathways, presents a major challenge for kinase selectivity—the ability of small molecule inhibitors to achieve potent inhibition of specific kinase targets while avoiding off-target interactions with structurally similar kinases. To demonstrate the capability of our framework for multi-objective optimization, we

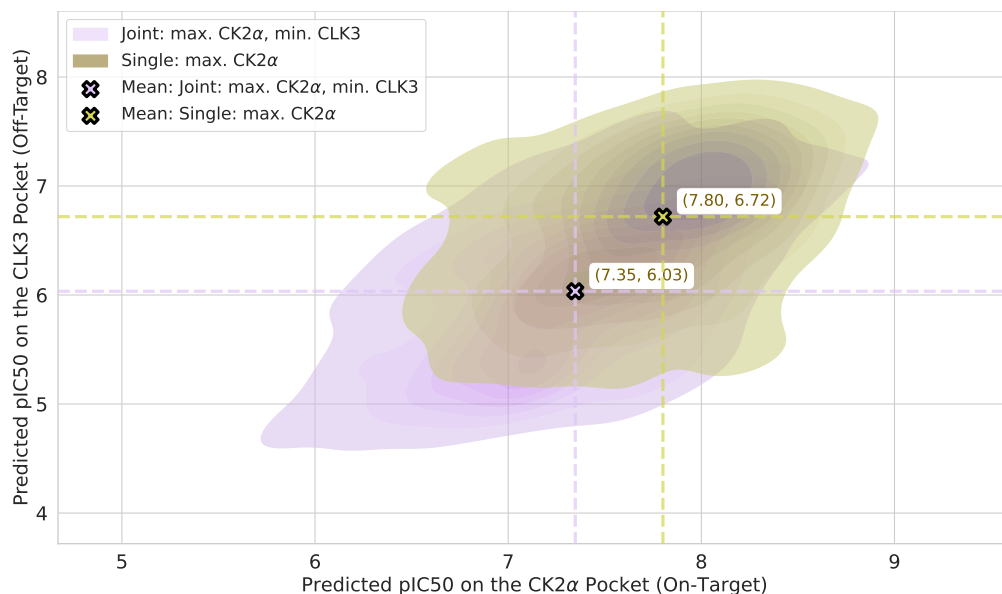


Figure 6: **Evaluation of FLOWR.ROOT on affinity-guided selectivity optimization of CK2 α and CLK3.** Kernel density estimation plot comparing joint optimization (purple, maximizing CK2 α while minimizing CLK3) versus single optimization (green, maximizing CK2 α only) on predicted pIC50 values. Black X markers show mean values with dashed reference lines. Joint optimization achieves improved selectivity with lower off-target CLK3 activity (mean pIC50 = 6.03 vs. 6.72) while maintaining comparable on-target CK2 α potency, demonstrating kinase selectivity optimization.

perform a selectivity study targeting selectivity between CK2 α (on-target, PDB: 3pe1) and CLK3 (off-target, PDB: 6khf).

We compare two optimization strategies using importance sampling: joint optimization that simultaneously maximizes the predicted binding affinity on CK2 α while minimizing CLK3 affinity formulated as dual-objective, versus the single optimization which only maximizes CK2 α . We generated 1,000 ligands for each set using the protein pockets from PDB 3pe1 [Battistutta et al., 2011] and 6khf [Lee et al., 2019] after rotational alignment.

Our results show that joint optimization successfully achieves improved selectivity profiles compared to single-target optimization. The joint approach generated ligands with significantly lower off-target CLK3 activity (mean pIC50 = 6.03) compared to single optimization (mean pIC50 = 6.72), while maintaining comparable on-target CK2 α potency as shown in the distribution plots in Fig. 6 with mean pIC50 of 7.35 for the joint set on CK2 α .

We further benchmark our approach using an alternative protocol. To this end, we took the 1,000 FLOWR.ROOT-generated ligands from the joint optimization and performed QM binding energy calculations. We excluded all complexes for which CLK3 binding energies were above 40.0 kcal/mol, as these resulted from structural clashes (Å5.6 % of all complexes). Fig. 7a shows a scatter plot of CK2 α against CLK3 binding energies. The scatter shows a linearized correlation shifted towards lower CK2 α binding energies, corroborating the success of the approach. Though other statistical metrics were calculated, we stress the calculated RMSE of 25.06 kcal/mol for this correlation. As RMSE measures deviation from the identity line, a large value implies selectivity towards one kinase, which from the data we conclude is CK2 α . Further, we record several outliers from linearity, which result from the fact that FLOWR.ROOT tries to further penalize ligands in the CLK3 pocket. In this task, however, the most relevant metric is the relative binding energy of a given ligand towards the pockets of each kinase. Fig. 7b shows the distribution of relative binding energies in these two kinases. The distribution, peaked at about -17.0 kcal/mol, is skewed, with a quick decay towards higher relative binding energies (less selective) and a slower decay on lower relative binding energies (more selective) further validating our approach.

It is particularly interesting to analyze ligands that minimize and maximize the relative binding energies between the two kinases. Fig. 7c-e compare a CK2 α -selective ($\Delta\Delta E_{bind} = -58.18$ kcal/mol) against a CLK3 binder ($\Delta\Delta E_{bind} = +18.00$ kcal/mol), indicating the mechanisms, with which FLOWR.ROOT tried to accomplish selectivity. Two major protein-ligand interactions were explored. On one hand, the interaction with the kinases' hinge. In both cases, the hydrogen bond between the generated ligand and L238 of CLK3 shows a suboptimal angular orientation.

Conversely, the CK2 α -selective binder shows a quasi-optimal hydrogen bond orientation with CK2 α 's H115, with the angle $H - \hat{N}_{ar} - C_{ar}$ reaching a value of 114.2°. In the case of the CLK3-selective binder, the equivalent angle with CK2 α 's main chain H of H115 goes up to 137.9°. Additional weakening of the hydrogen bond to CK2 α 's hinge is achieved by increasing the $H - \hat{N}$ distance, which goes from 2.77 Å in the CK2 α -selective binder to 2.97 Å in the CLK3-selective one.

The second mechanism is related to interactions with H160. In previous work [Grygier et al., 2023], we identified H160 as a critical residue conferring sub-nM affinity of the inhibitor silmitasertib to CK2 α . Here too, we observe that FLOWR.ROOT explores interactions with this residue to achieve selectivity. On the CK2 α -selective binder, FLOWR.ROOT orients the ligand's phenyl substituent to optimize a T-stack interaction. On the CLK3-selective binder, a similar substituent is rotated to yield a short, repulsive contact. This is possible because the side chain of E287, the residue in a similar position in CLK3, points in another direction.

We conclude that, in order to achieve selectivity between two similar kinases, FLOWR.ROOT exploited two previously identified elements of selectivity. This concerns the hinge region of kinases, where better binders show shorter hydrogen bond distances and more adequate angles. Simultaneously, FLOWR.ROOT also explored lipophilic interactions with the two kinases, optimizing a T-stack with a residue critical for the high potency of drugs currently in clinical trials. We stress that none of these interactions could have been passed to the model during training or in guiding selectivity.

2.10 TYK2, ER α , and BACE1

As shown in previous sections, FLOWR.ROOT generates novel chemical matter conditioned on a protein pocket. The generated molecules are chemically reasonable and are not heavily strained, unlike previous generative models. Additionally, the predicted affinity data reliably reproduces experimental distributions. In this section, we benchmark how the whole FLOWR.ROOT workflow behaves on the task of conditional ligand generation. To this end, we chose the TYK2 kinase, ER α , and BACE1 as targets from the Schrodinger FEP+ dataset.

Testing whether the FLOWR.ROOT-generated ligands are good binders requires effective metrics. In this case, we chose to benchmark the FLOWR.ROOT poses using QM binding energy analysis. QM calculations on protein-ligand complexes offer scoring functions; therefore we aimed at finding a correlation between QM binding energies and the median of predicted binding affinities.

We first look at the example of the TYK2 kinase (Fig. 8a-c). We find a good correlation between the QM-calculated binding energies and the FLOWR.ROOT-predicted median affinities, with an R^2 of 0.70, a Pearson correlation coefficient of 0.84, a Kendall τ of 0.45, RMSE of 0.19, and RAE of 0.57. From a chemical viewpoint, it is more interesting to compare the structures of the best and worst FLOWR.ROOT-predicted ligands. We see that, despite some common features, the model generalizes effectively the hinge-binding motif, and the solvent-exposed residue of the ligand. Importantly, all ligands retained the hydrogen bond acceptor to V981, a critical hinge residue already in the original ligand structure. Binding to a kinase's hinge is very important in kinase inhibition, kept by FLOWR.ROOT-generated chemical matter. Interestingly, no ligand improved the hydrogen-bond geometry with P982, despite some variations in the chemotypes exhibited by the hinge-binding heads. The major differences take place in how specific interactions are exploited. Particularly critical for the best binder in this series is the π -stack interaction established with Y980. But also the fact that this ligand protects the least lipophilic halogens from solvent exposure. We also calculated ligand deformation energies, which for this series lie between 19.32 kcal/mol and 44.29 kcal/mol.

A similar correlation was obtained for ER α (Fig. 8d-f), however, in this case, all the statistical metrics improved: The R^2 is 0.81, the Pearson correlation coefficient is 0.90, the Kendall τ is 0.68, RMSE is 0.17 and RAE 0.46. Some variability is expected between systems, and in the case of ER α we observe less outliers than in the TYK2 example. In the case of ER α , we observed that FLOWR.ROOT retained most of the ligand's structure, improving mostly the interactions with the residue H524. In the structure of the original ligand there is a poorly-oriented hydrogen bond with H524, which is effectively corrected even in the case of the worst binder: the FLOWR.ROOT-generated ligands exhibited better geometries for this hydrogen bond. Similar to the case of the TYK2 kinase, we calculated ligand deformation energies, which were between 24.36 kcal/mol and 38.30 kcal/mol.

Finally, we also analysed a benchmark on BACE1 (Fig. 8g-i), where we obtained the best correlation of this series between FLOWR.ROOT-predicted affinities and the QM calculated ones. This is seen in the lowest RAE and RMSE coupled with the highest R^2 , Pearson correlation coefficient, and Kendall τ of this series of benchmarks. We see that in all cases the ligands retain a water-mediated hydrogen bond with F108, which results in high affinities overall. The major differences are in the nature of the nitrogen-containing group near Y71, which seems to favour more lipophilic groups, but also the substituents in the aromatic ring T-stacking the residue W115. We note that the T-stack interaction is favoured by electron-rich phenyl rings, which is not the case of the worst binder in the series. This seems then to be one of the major effects controlling affinity to BACE1.

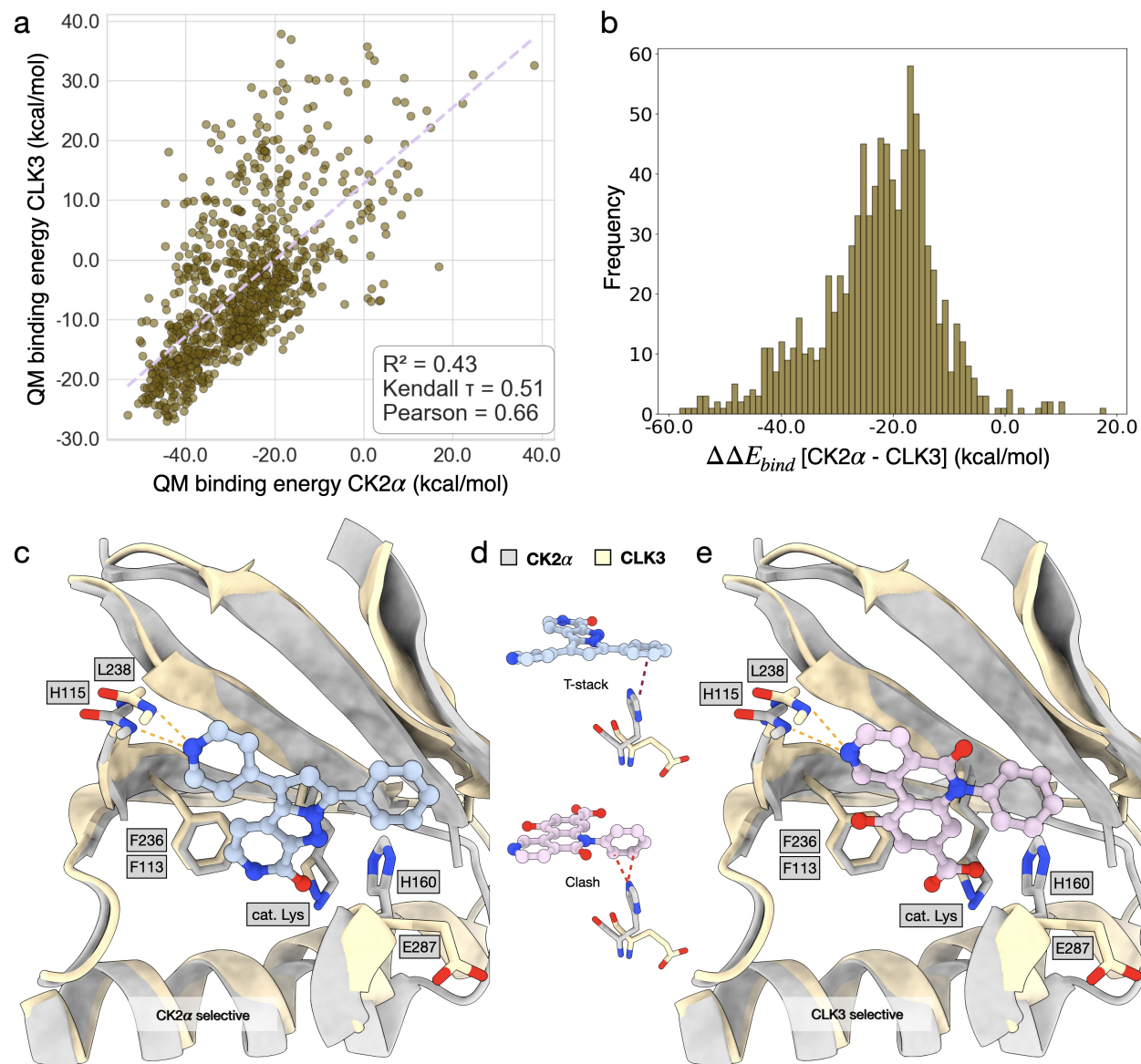


Figure 7: Quantum mechanical analysis of FLOWR.ROOT on selective ligand design on CK2 α and CLK3 a Quantum mechanical-calculated binding energy for CLK3 vs. CK2 α . Ligands for which the binding energy is higher than 40.0 kcal/mol were excluded from the plot ($\approx 5\%$). The plot shows systematically lower binding energies for CK2 α , indicating selectivity. **b** The distribution of the difference in binding energies for all investigated ligands. The skewed distribution peaks at about -17.0 kcal/mol. **c** Example of a CK2 α -selective ligand and its interaction patterns with the kinases' pockets. **e** Example of a CLK3-selective ligand and its interaction patterns with the kinases' pockets. **d** Interactions of the two ligands with the residue H160.

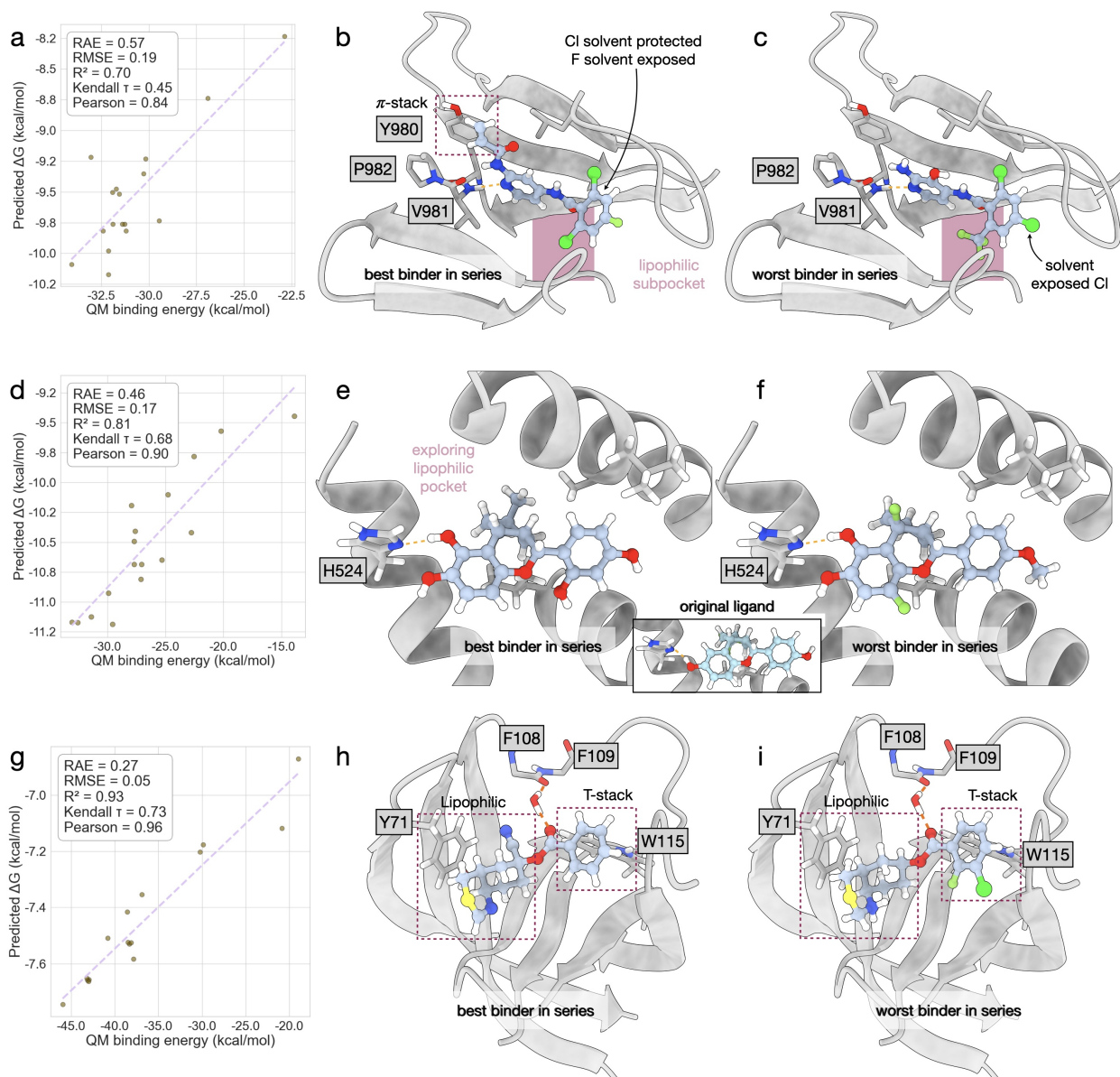


Figure 8: FLOWR.ROOT binding affinity validation using quantum mechanical calculations on TYK2, ER α and BACE1. Benchmark cases of the TYK2 kinase (**a-c**), ER α (**d-f**), and BACE1 (**g-i**). **a** correlation plot between FLOWR.ROOT predicted affinities and the quantum mechanical binding energies for TYK2. **b** example of the best binder in the series and its interactions with the pocket. **c** example of the worst binder in the series and its interactions with the pocket. **d** correlation plot between FLOWR.ROOT predicted affinities and the quantum mechanical binding energies for ER α . **e** example of the best binder in the series and its interactions with the pocket. **f** example of the worst binder in the series and its interactions with the pocket. **g** correlation plot between FLOWR.ROOT predicted affinities and the respective quantum mechanical binding energies. **h** example of the best binder in the series and its interactions with the pocket. **i** example of the worst binder in the series and its interactions with the pocket.

3 Discussion

In this work, we introduced FLOWR.ROOT, a foundational framework for structure-based generative chemistry that unifies multi-mode ligand generation with binding affinity prediction and domain adaptation within a single E(3)-equivariant flow matching architecture. The framework supports *de novo* design, interaction-guided generation, and fragment-based elaboration, enabling applications spanning from early-stage hit identification to late-stage lead optimization. By coupling structural prediction with dedicated affinity heads and confidence estimation, FLOWR.ROOT directly integrates affinity estimation into the generative trajectory, allowing property-guided molecule design through inference-time steering. Our three-stage training paradigm—large-scale pre-training on billions of ligands and millions of mixed-fidelity protein-ligand complexes, refinement on curated high-fidelity datasets, and project-specific adaptation—enables the model to capture broad chemical diversity while remaining efficiently adaptable to specialized structure-activity landscapes.

Our comprehensive evaluation demonstrates that FLOWR.ROOT advances the state of the art across multiple dimensions spanning from unconditional molecule to structure-aware ligand generation consistently outperforming recent diffusion- and flow-based approaches. For affinity prediction, FLOWR.ROOT achieves robust correlation with experimental measurements across diverse assay types, matching or exceeding the performance of computationally expensive physics-based and clearly outperforming ML-based methods while operating orders of magnitude faster. Critically, the model predictions maintain reliability across both public benchmarks and project-specific datasets when followed by targeted parameter-efficient finetuning, demonstrating practical utility in real-world medicinal chemistry workflows.

Quantum mechanical validation studies on TYK2 kinase, ER α , and BACE1 provide evidence of FLOWR.ROOT’s capacity to generate chemically meaningful ligands and binding poses. Strong correlations between model-predicted affinities and rigorous QM binding energies—coupled with mechanistic analysis revealing that generated ligands systematically exploit key structural motifs such as hinge-binding interactions, hydrogen bond geometries, and aromatic stacking—demonstrate that the model has internalized fundamental principles of protein-ligand interactions. Our kinase selectivity study between CK2 α and CLK3 further illustrates that through affinity-guided generation, FLOWR.ROOT can help finding selectivity mechanisms. Overall, FLOWR.ROOT provides a concrete step toward the vision of establishing continuously evolving frameworks that refine their understanding through sustained interaction with project-specific data, offering a foundational yet adaptable architecture that generalizes broadly, and adapts flexibly to specialized domains integrating well into medicinal chemistry workflows.

Nevertheless, important limitations remain. The reliance on public datasets, despite extensive curation, introduces biases from noisy affinity measurements, overrepresented protein families, and uneven chemical diversity. While higher-fidelity datasets partially mitigate these issues, their limited scale constrains model calibration, particularly for underexplored targets. Project-specific adaptation, though powerful, requires carefully chosen objectives and sufficient assay data; otherwise, models risk overfitting to narrow distributions. Additionally, FLOWR.ROOT requires the binding pocket to be known and preferably in a holo conformation, leaving the challenge of modeling protein pocket flexibility to future work. Finally, the predictions of FLOWR.ROOT remain *in silico* approximations that cannot substitute for experimental validation.

Looking forward, several directions appear promising. Expanding project-level adaptation to include reinforcement learning or active learning frameworks with both physics-based and experimental feedback may enable continuous refinement during discovery campaigns. Further, enhancing synthetic accessibility estimation and coupling to reaction-based generative models would improve downstream feasibility, ensuring that generated molecules are not only potent but also synthetically accessible.

Data Availability

All datasets used in this study are publicly available and can be downloaded from Google Drive at https://drive.google.com/drive/folders/1NWpzTY-BG_9C4zXZndWlKwdu7UJNCYj8.

Code Availability

The source code for FLOWR.ROOT is publicly available on GitHub at github.com/jule-c/flowr_root. The pretrained model checkpoint can be downloaded from Google Drive at https://drive.google.com/drive/folders/1NWpzTY-BG_9C4zXZndWlKwdu7UJNCYj8.

Acknowledgments

F.M. acknowledges support from Helmholtz Munich. E.S. acknowledges support from Jagiellonian University Medical College.

Author Contributions

J.C. conceived the study; developed the methodology; performed experiments, validation, formal analysis; implemented the software; curated the data; created the visualizations; and wrote the original draft of the manuscript. T.L. assisted with experiments. M.M.G. contributed to study design. E.S. assisted with data preparation. F.M. performed validation, formal analysis; created visualizations and wrote the original draft of the manuscript. D.-A.C. provided supervision. All authors reviewed and edited the manuscript.

Competing Interests

J.C., T.L., M.M.G and D.-A.C. are employees of Pfizer Inc. All authors declare no competing interests.

Supplementary Information

A Methods

This section outlines the methodology employed in our framework, FLOWR.ROOT, for generative structure-aware ligand modeling and binding affinity prediction. We provide a detailed description of the architecture and key components, including framework details about the three-stage training process, the generative modes available for ligand design, and the affinity prediction capabilities. We also discuss the strategies for confidence estimation, inference-time scaling via importance sampling, and domain adaptation as main application in practical drug discovery workflows.

A.1 FLOWR.ROOT

FLOWR.ROOT is built on the recently proposed FLOWR architecture, an $SE(3)$ -equivariant flow matching model that learns a mixed continuous/discrete transport map. This map transforms a prior distribution (e.g., random noise or fragment anchors for coordinates) to the target ligand distribution within a given protein pocket [Cremer et al., 2025]. The model consists of two main components: a pocket encoder and a ligand decoder.

Protein pockets are extracted from holo structures by cutting residues within a defined radius around the binding site. We use a 7Å cutoff radius, which represents a practical compromise between computational tractability and interaction coverage. This cutoff fully encompasses hydrogen bonds directly relevant to ligand binding (which decay rapidly beyond 5.5–6Å), captures vibrational entropy contributions from direct protein-ligand interactions, and includes conformational entropy changes in the binding pocket. While long-range electrostatic effects are system-dependent (primarily affecting charged ligands), the 7Å cutoff provides sufficient coverage for neutral ligands and partial cancellation occurs for charged species. Water-mediated interactions are treated implicitly, consistent with many previous ML approaches. The cutoff is a configurable parameter that can be adjusted at both training and inference time.

These pockets are then encoded using an equivariant self-attention module followed by equivariant feed-forward layers, generating a set of invariant and equivariant protein features [Cremer et al., 2025]. The ligand decoder processes noisy ligand coordinates, partial charges, atom types, bond orders, and hybridization states through equivariant self-attention modules, which capture intra-ligand dependencies. A cross-attention layer then integrates contextual information from the pocket features to the hidden ligand features. The pocket encoder processes features on a full-atom basis through $SE(3)$ -equivariant self-attention layers using invariant residue embeddings, equivariant coordinate features, and pairwise fully-connected distance information between all pocket atoms. Via fully-connected, equivariant cross-attention, the ligand decoder interacts with the invariant and equivariant pocket encodings for ligand generation. For additional details, we refer to Cremer et al. [2025].

In FLOWR.ROOT, the ligand decoder has three output heads: (1) a structure head that predicts atomic coordinates, atom types, bond orders, charges, and hybridization states; (2) an affinity head comprising of four separate potency and binding affinity heads—specifically, for IC_{50} , pK_i , pK_d , and pEC_{50} prediction—and (3) a confidence head that provides uncertainty estimation based on pLDDT [Abramson et al., 2024]. Importantly, these heads serve distinct yet complementary purposes: the structure head generates geometrically valid ligand conformations within the protein pocket, while the affinity head provides potency and binding affinity estimates that enable (1) in-distribution evaluation of generated structures, (2) inference-time steering toward higher-affinity compounds via importance sampling, and (3) domain adaptation of both structure and affinity prediction through joint finetuning. This joint training paradigm thus facilitates coherent, in-distribution property-guided generation without requiring external scoring functions—avoiding distribution mismatch and additional computational overhead—while supporting effective domain adaptation.

Importantly, FLOWR.ROOT builds upon the multi-task training framework of FLOWR [Cremer et al., 2025], yet extends it substantially to support four generative modes within a single backbone: (1) *de novo* and, (2) interaction-conditional generation for preserving or enforcing pharmacophoric patterns, (3) scaffold hopping and elaboration, and (4) fragment growing and replacement. Notably, with the latter two FLOWR.ROOT supports specifying which atoms to replace while preserving the remainder of the molecule. To enforce locality in these partial modifications, we introduce a flexible prior placement strategy that shifts the generative prior from the zero center-of-mass to the local replacement site. This multi-mode capability enables flexible application across hit identification and hit-to-lead and lead optimization with targeted structural modifications.

The core challenge in protein-ligand modeling, however, lies not just in generation, but in accurately predicting protein-ligand interactions and potency. The sparsity of experimental binding data—where most ligand-protein combinations remain unexplored—poses a significant obstacle to improving these predictions. While broad-coverage datasets encompass a wide spectrum of protein targets, they are intrinsically sparse, with few ligands tested systematically across different biological contexts. This imbalance leads to biased datasets, which explains why 3D machine and

deep learning models—often relying only on protein or ligand descriptors and ignoring interaction patterns—can perform surprisingly well on affinity prediction benchmarks like PDBbind [Volkov et al., 2022]. Real-world drug discovery requires understanding nuanced SAR across hundreds or even thousands of related molecules within the same binding site—a richness uniquely captured by dense bioactivity landscapes. These landscapes encode redundancy and critical phenomena like activity cliffs, where small structural changes can lead to significant shifts in bioactivity due to interaction changes. This motivates the multi-stage training approach of FLOWR.ROOT: starting with sparse, lower-fidelity data to learn broad 3D chemistry and binding principles, and progressively refining the model with denser, higher-fidelity and project-specific datasets that capture subtle SAR patterns essential for effective hit expansion to lead optimization. This multi-stage pipeline is intended to closely mirror the practical needs of early drug discovery campaigns, addressing the limitations imposed by data sparsity in current 3D affinity prediction models. The FLOWR.ROOT framework consists of three stages:

Stage 1: Large-scale pre-training. This stage builds a general-purpose generative prior across chemical and structural distributions, with a broad bioactivity landscape, albeit with varying quality and predictive relevance. The model is trained on a mixture of:

- **Small molecules in vacuum** (~ 1.5 B datapoints from ZINC3D, PubChem3D, Enamine, OMol25) to ensure broad chemical coverage.
- **Protein–ligand complexes with and without affinity labels** (~ 2.5 M datapoints from Plinder, BindingMoad, BindingNet, SAIR, KIBA-3D, Kinodata-3D, OMol25), which capture protein-ligand structural diversity, in parts annotated with affinity data. This dataset is split into lower- and higher-fidelity categories. We classify complexes with computational origin (i.e., BindingNet, SAIR, KIBA-3D, Kinodata-3D) as lower-fidelity and those stemming from co-crystal data (i.e., Plinder, BindingMoad) as higher-fidelity, with the exception of the high-confidence subset of BindingNet, which is treated as higher-fidelity.

Stage 2: High-fidelity finetuning. Pre-trained weights are adapted to thoroughly curated, drug-like, high-quality affinity datasets. In this work, we use SPINDR and HIQBIND (~ 30 k complexes) as datasets for multi-target finetuning. However, this stage can be used to finetune FLOWR.ROOT on diverse, high-quality in-house data, if available, which teaches the model the fine details of protein-ligand interactions and binding affinity.

Stage 3: Project-specific domain adaptation. This ensures that FLOWR.ROOT can bridge the gap between large-scale, noisy public data and small-scale, high-quality, dense in-assay data, producing distributions that align with specific discovery campaigns. Different domain adaptation strategies are used to finetune and steer the pre-trained FLOWR.ROOT model:

- **Inference-time scaling and property steering:** Importance sampling and path reweighting guide the model toward desired properties such as affinity, ADME/T, or synthetic accessibility.
- **Direct preference alignment:** The model is finetuned with project-specific preferences, such as avoiding known liability motifs or penalizing activity cliffs (future work).
- **Finetuning:** Parameter-efficient finetuning, namely Low-Rank Adaption (LoRA) [Hu et al., 2022], helps avoid catastrophic forgetting while aligning the model to project-specific structure-activity modes.

A.2 Training and Inference

Following the methodology of Cremer et al. [2025], we adopted the training and parameterization scheme from FLOWR.MULTI. Specifically, we employed a 4-layer pocket encoder with $d_{\text{inv}}^{\text{enc}} = 256$ and a 12-layer ligand decoder with $d_{\text{inv}}^{\text{dec}} = 384$. The equivariant feature dimension was set to $d_{\text{equi}} = 128$ for both the pocket encoder and ligand decoder. For latent attention, we utilized a latent size of 64 with 32 attention heads. Overall, FLOWR.ROOT has approximately 33 million trainable parameters. Throughout this work, the model has been trained on one NVIDIA H100 node comprising eight H100 GPUs.

To further enhance model stability and generalization, we incorporated residual coordinate and subsequent edge updates using Gaussian radial basis expansions [Le et al., 2023], applied to the layer-wise latent message-passing outputs of the FLOWR model backbone [Cremer et al., 2025]. Additionally, we included distance and cross-product computations between latent equivariant node features within the message-passing layers, which we found to improve model performance. Specifically, in the pairwise interactions between nodes, given the equivariant queries $q_{\text{equi}} \in \mathbb{R}^{B \times N_q \times 3 \times d_{\text{equi}}}$ and keys $k_{\text{equi}} \in \mathbb{R}^{B \times N_{kv} \times 3 \times d_{\text{equi}}}$, we define the pairwise difference tensor as

$$\mathbf{D} = \mathbf{Q}[:, :, \mathbf{1}, :] - \mathbf{K}[:, \mathbf{1}, :, :],$$

and compute the distance features as

$$\mathbf{S} = |\mathbf{D}|_2 \in \mathbb{R}^{B \times N_q \times N_k \times d}.$$

The pairwise cross product tensor is defined as

$$\mathbf{C} = \mathbf{Q}[:, :, \mathbf{1}, :] \times \mathbf{K}[:, \mathbf{1}, :, :],$$

where \times denotes the vector cross product over the 3-vector dimension, resulting in

$$\mathbf{C} \in \mathbb{R}^{B \times N_q \times N_k \times 3 \times d}.$$

Both \mathbf{S} and \mathbf{C} are stacked to the existing pairwise message tensor as additional features.

The model structure output comprises predictions for atomic coordinates, atom types, charge, hybridization, bond types, bond lengths and bond angles. The overall loss function reads:

$$\begin{aligned} \mathcal{L}_{total} = & \underbrace{\lambda_c \text{MSE}(\mathbf{X}_{pred}, \mathbf{X}_{true})}_{\text{Coordinate loss}} + \underbrace{\lambda_t \text{CE}(\mathbf{A}_{pred}, \mathbf{A}_{true})}_{\text{Atom type loss}} + \underbrace{\lambda_{ch} \text{CE}(\mathbf{Q}_{pred}, \mathbf{Q}_{true})}_{\text{Charge loss}} + \\ & \underbrace{\lambda_h \text{CE}(\mathbf{H}_{pred}, \mathbf{H}_{true})}_{\text{Hybridization loss}} + \underbrace{\lambda_b \text{CE}(\mathbf{B}_{pred}, \mathbf{B}_{true})}_{\text{Bond type loss}} + \underbrace{\lambda_{bl} \mathcal{L}_{bond length}}_{\text{Bond length loss}} + \underbrace{\lambda_{ba} \mathcal{L}_{bond angle}}_{\text{Bond angle loss}} \end{aligned}$$

with λ_i denoting the respective loss weighting. To encourage geometrically accurate bond lengths, we compute the mean squared error between predicted and ground truth distances for all bonded atom pairs:

$$\mathcal{L}_{bond length} = \frac{1}{|\mathcal{B}|} \sum_{(i,j) \in \mathcal{B}} \left(\|\mathbf{x}_i^{pred} - \mathbf{x}_j^{pred}\|_2 - \|\mathbf{x}_i^{true} - \mathbf{x}_j^{true}\|_2 \right)^2 \quad (1)$$

where \mathcal{B} denotes the set of bonded atom pairs extracted from the bond adjacency matrix, considering only the upper triangle to avoid redundancy. To preserve local molecular geometry, we penalize deviations in bond angles for all valid triplets (i, j, k) where atom j is bonded to both atoms i and k . For each triplet, the bond angle θ_{ijk} is computed as:

$$\theta_{ijk} = \arccos \left(\frac{(\mathbf{x}_i - \mathbf{x}_j) \cdot (\mathbf{x}_k - \mathbf{x}_j)}{\|\mathbf{x}_i - \mathbf{x}_j\|_2 \cdot \|\mathbf{x}_k - \mathbf{x}_j\|_2} \right) \quad (2)$$

The bond angle loss is then defined using the Huber loss for robustness:

$$\mathcal{L}_{bond angle} = \frac{1}{|\mathcal{A}|} \sum_{(i,j,k) \in \mathcal{A}} \text{Huber}_\delta \left(\theta_{ijk}^{pred} - \theta_{ijk}^{true} \right) \quad (3)$$

where \mathcal{A} is the set of valid angle triplets, and the Huber loss with threshold δ is defined as:

$$\text{Huber}_\delta(x) = \begin{cases} \frac{1}{2}x^2 & \text{if } |x| \leq \delta \\ \delta \left(|x| - \frac{1}{2}\delta \right) & \text{otherwise} \end{cases} \quad (4)$$

We use $\delta = 0.5$ radians to balance sensitivity to small deviations while remaining robust to outliers.

FLOWR.ROOT jointly models both continuous (coordinates) and discrete (atom types, bond orders, charges, hybridizations) molecular features. For coordinates, we employ continuous flow matching [Tong et al., 2024], while discrete flow models [Campbell et al., 2024] are used for categorical variables. The model is trained to recover the original ligand l_1 from a noisy ligand l_t by learning the conditional distribution $p_{1|t}^\theta(l_1|l_t, t; \mathcal{P})$, minimizing mean squared error for coordinates and cross-entropy loss for categorical features. Given a pocket structure \mathcal{P} , novel ligands are generated by iteratively refining an initial noisy ligand $l_0 \sim p_{\text{noise}}$. The generative process follows a learned vector field v_t^θ for continuous features and a discrete integration scheme for categorical attributes [Campbell et al., 2024, Cremer et al., 2025].

Anisotropic and reference-ligand-based prior strategies Standard flow matching employs an isotropic Gaussian $\mathcal{N}(\mathbf{0}, \mathbf{I})$ as the source distribution p_0 . In partial generation modes—scaffold hopping, scaffold elaboration, linker inpainting, core growing, and fragment growing—a fixed molecular substructure provides geometric context that constrains where new atoms should be placed. An isotropic prior distributes probability mass without directional bias, forcing the learned velocity field v_t^θ to perform long-range, direction-dependent transport to reach the target region. A distinguishing property of flow matching, in contrast to diffusion models where the terminal distribution is determined by the noise schedule, is that p_0 need not be a standard Gaussian: any distribution from which efficient sampling is possible suffices [Tong et al., 2024]. The velocity field is trained to transport whatever p_0 is supplied toward p_1 , enabling

per-sample prior selection and even mixed isotropic and anisotropic batches within a single training step. FLOWR.ROOT exploits this flexibility by constructing task-specific anisotropic Gaussian priors whose covariance encodes the spatial extent and directionality of the generation context.

Two complementary covariance constructions are employed. The *shape-based covariance* captures the spatial extent of a set of reference atom coordinates. Given a set of N reference atom coordinates $\{\mathbf{r}_i\}_{i=1}^N$ (variable atoms or the full molecule, depending on the generation mode), the centered coordinate matrix is

$$\bar{\mathbf{X}} = \mathbf{X} - \frac{1}{N} \mathbf{1} \mathbf{1}^\top \mathbf{X}, \quad \mathbf{X} \in \mathbb{R}^{N \times 3}, \quad (5)$$

and the sample covariance is

$$\mathbf{C} = \frac{1}{N-1} \bar{\mathbf{X}}^\top \bar{\mathbf{X}}. \quad (6)$$

Eigendecomposing $\mathbf{C} = \mathbf{V} \text{diag}(\lambda_1, \lambda_2, \lambda_3) \mathbf{V}^\top$ with $\lambda_1 \geq \lambda_2 \geq \lambda_3 \geq 0$, the eigenvalues are first normalized to satisfy $\sum_k \tilde{\lambda}_k = 3$:

$$\tilde{\lambda}_k = \lambda_k \cdot \frac{3}{\sum_j \lambda_j}, \quad (7)$$

then clamped to $[\lambda_{\min}, \lambda_{\max}]$ and re-normalized to restore the trace constraint. The shape-based covariance is

$$\Sigma_{\text{shape}} = \mathbf{V} \text{diag}(\lambda_1^*, \lambda_2^*, \lambda_3^*) \mathbf{V}^\top. \quad (8)$$

This construction is applied in scaffold hopping and core growing (using the variable-atom coordinates as reference), as well as in scaffold elaboration and linker inpainting (using the full-molecule coordinates to capture the spatial extent of the entire ligand).

The *directional covariance* encodes a preferred growth direction from a fixed fragment toward a target region. Given the center of mass of the fixed fragment \mathbf{c}_{src} and a target center \mathbf{c}_{tgt} (the prior center or the center of mass of the variable atoms), the unit direction is

$$\mathbf{d} = \frac{\mathbf{c}_{\text{tgt}} - \mathbf{c}_{\text{src}}}{\|\mathbf{c}_{\text{tgt}} - \mathbf{c}_{\text{src}}\|_2}. \quad (9)$$

An orthonormal basis $\{\mathbf{v}_2, \mathbf{v}_3, \mathbf{d}\}$ is obtained via Gram–Schmidt orthogonalization, yielding a rotation matrix $\mathbf{R}_{\text{dir}} = [\mathbf{v}_2 \mid \mathbf{v}_3 \mid \mathbf{d}] \in SO(3)$. With an elongation factor $\alpha > 1$ (default $\alpha = 2$) and the trace normalization constraint $\text{tr}(\Sigma) = 3$, the eigenvalues become

$$\lambda_{\perp} = \frac{3}{2 + \alpha}, \quad \lambda_{\parallel} = \frac{3\alpha}{2 + \alpha}, \quad (10)$$

and the directional covariance reads

$$\Sigma_{\text{dir}} = \mathbf{R}_{\text{dir}} \text{diag}(\lambda_{\perp}, \lambda_{\perp}, \lambda_{\parallel}) \mathbf{R}_{\text{dir}}^\top. \quad (11)$$

This construction is used for fragment growing, where the direction points from the fixed fragment toward the prior center, and composes with the reference-ligand center-of-mass placement described below.

Both covariance types satisfy the trace invariant $\text{tr}(\Sigma) = 3$, ensuring $\mathbb{E}[\|\mathbf{x}_0\|^2] = 3$ for $\mathbf{x}_0 \sim \mathcal{N}(\mathbf{0}, \Sigma)$, the same second moment as the isotropic prior. This guarantees consistent velocity field magnitudes across prior types and enables stable mixed-batch training in which isotropic and anisotropic samples coexist. Since both Σ_{shape} and Σ_{dir} are derived from reference atom coordinates, they transform equivariantly under rigid-body transformations of the protein–ligand complex, preserving the $SE(3)$ -equivariance of the model. Sampling from $\mathcal{N}(\mathbf{0}, \Sigma)$ is performed via the Cholesky decomposition $\Sigma = \mathbf{L} \mathbf{L}^\top$, yielding $\mathbf{x}_0 = \mathbf{z} \mathbf{L}^\top$ with $\mathbf{z} \sim \mathcal{N}(\mathbf{0}, \mathbf{I})$.

Orthogonal to the covariance construction, the prior point cloud can be spatially relocated to improve locality. For global inpainting modes, the prior cloud is shifted to the center of mass of the to-be-generated atoms in the reference ligand. During training, Gaussian noise with standard deviation σ_{noise} is added to this placement for robustness. Covariance controls the shape of the prior while placement controls its location; the two compose independently. For substructure and fragment inpainting, the prior cloud is shifted to the center of mass of the to-be-replaced fragment in the reference ligand, and an isotropic $\mathcal{N}(\mathbf{0}, \mathbf{I})$ prior suffices since the spatial placement itself provides sufficient locality.

Potency and binding affinity prediction In drug discovery, a variety of parameters, including IC_{50} , K_i , K_d , and EC_{50} , are reported as potency and binding affinity measures. These parameters differ in their definitions and experimental setups, which complicates their direct comparison. For example, K_d is an equilibrium constant that directly measures the strength with which a ligand binds to its target protein. On the other hand, a K_i is an equilibrium constant indicating how well a given inhibitor inhibits the binding of a natural substrate. In other words, while K_d measures the "stickiness"

of a molecule to a target, K_i measures how well the inhibitor blocks the enzyme from its natural substrate. Though these values often correlate, they are not always interchangeable. Likewise, EC_{50} and IC_{50} are used for biological assays. Though they correlate with K_d and K_i , their interpretation depends on assay conditions. For better readability, for the remainder of this work we refer to potency and binding affinity prediction as affinity prediction.

Therefore, in contrast to prior work [Valsson et al., 2025, Passaro et al., 2025], we predict each potency measure separately, aligning better with the complexity of drug-target data. Specifically, FLOWR.ROOT employs separate prediction heads for each affinity type (pIC_{50} , pK_d , pK_i , pEC_{50}), with each head trained separately on its corresponding data type. This design explicitly avoids treating heterogeneous affinity labels as interchangeable. Given invariant and equivariant ligand features $\mathbf{h}_i^{\text{inv}}$, $\mathbf{h}_i^{\text{equi}}$, pocket features $\mathbf{p}_j^{\text{inv}}$, $\mathbf{p}_j^{\text{equi}}$, and ligand-pocket interaction features \mathbf{e}_{ij} extracted from the ligand decoder’s latent message-passing module, the affinity head computes:

$$\begin{aligned} \mathbf{f}_i^{\text{lig}} &= \text{Gate}(\mathbf{h}_i^{\text{inv}}, \mathbf{h}_i^{\text{equi}}) \\ \mathbf{z}^{\text{lig}} &= \text{MLP}_{\text{lig}} \left(\left[\frac{1}{C} \sum_i \mathbf{f}_i^{\text{lig}}, \frac{1}{|\mathcal{L}|} \sum_i \mathbf{f}_i^{\text{lig}} \right] \right) \\ \mathbf{f}_j^{\text{pocket}} &= \text{Gate}(\mathbf{p}_j^{\text{inv}}, \mathbf{p}_j^{\text{equi}}) \\ \mathbf{z}^{\text{pocket}} &= \text{MLP}_{\text{pocket}} \left(\frac{1}{|\mathcal{P}|} \sum_j \mathbf{f}_j^{\text{pocket}} \right) \\ \mathbf{z}^{\text{int}} &= \text{MLP}_{\text{int}} \left(\frac{\sum_{i,j} \mathbf{e}_{ij} m_i m_j}{\sum_{i,j} m_i m_j} \right) \end{aligned}$$

where Gate is a Gated equivariant block [Schütt et al., 2021] to combine equivariant and invariant feature tensors, and MLP is a multi-layer perceptron with two linear layers and SiLU activation. The input to MLP_{lig} is the concatenation of normalized invariant features, where $C = 100$, and $|\mathcal{L}|$ denotes the number of atoms in the ligand. The concatenated feature tensor $\mathbf{z} = [\mathbf{z}^{\text{lig}}, \mathbf{z}^{\text{pocket}}, \mathbf{z}^{\text{int}}]$ is passed to task-specific heads defined as

$$y_{\text{affinity}} = \text{ReLU}(\text{MLP}_{\text{affinity}}(\mathbf{z})).$$

The affinity prediction loss is computed using the mean Huber loss between predicted and true affinity values in log units (pIC_{50} , pK_d , pK_i , pEC_{50}) through

$$\mathcal{L}_{\text{affinity}} = \frac{1}{N} \sum_{i=1}^N \text{Huber}(\hat{y}_i, y_i),$$

where \hat{y}_i and y_i are the predicted and true affinity values for valid samples i , and N is the number of valid samples.

To convert affinity values to experimental free energy ΔG values for comparison with physics-based models, we use the following formula:

$$\Delta G = -RT \ln 10 \cdot pK, \quad (12)$$

where $R = 1.987 \times 10^{-3} \text{ kcal K}^{-1} \text{ mol}^{-1}$ is the universal gas constant and $T = 298 \text{ K}$ is the absolute temperature and pK being the respective affinity type.

Confidence prediction: Predicted local distance difference test (pLDDT) We also predict pLDDT confidence scores to assess the reliability of generated ligand structures. Given predicted ligand samples $\hat{l}_1 = (\hat{X}, \hat{T}, \hat{Q}, \hat{H}, \hat{B})$ and ground-truth ligand-protein coordinates $X_l \in \mathbb{R}^{N_l \times 3}$ and $X_p \in \mathbb{R}^{N_p \times 3}$, we compute distance matrices $D, \hat{D} \in \mathbb{R}_+^{N_l \times N_p}$ for true and predicted ligand-protein distances, respectively. We consider distances below 12.0 \AA with $b_i = \text{clamp}(\sum_{j=1}^{N_p} (D_{i,j} < 12.0), \min = 1)$ neighbors for each ligand atom.

Using distance thresholds $\tau = \{\frac{1}{2}, 1, 2, 4\}$ and L1 distance errors $L = |D - \hat{D}|$, the LDDT score for each ligand atom is obtained through

$$\text{LDDT}_i = \frac{1}{b_i} \sum_{j=1}^{N_p} \left[\frac{1}{|\tau|} \sum_{c \in \tau} (L_{ij} < c) \right] \in (0, 1).$$

Each atom’s LDDT score is binned into $k = 50$ categories for multi-class classification. The confidence head, f_ϕ , shares the ligand decoder backbone with reduced depth ($l = 8$ layers), taking the generated structure \hat{l}_1 as input and outputting invariant logits $\text{pLDDT}_i \in \mathbb{R}^{50}$ for cross-entropy loss minimization.

Training and sampling overview We summarize the training and sampling procedures in Algorithms 1 and 2. The complete ligand representation comprises coordinates \mathbf{X} , atom types \mathbf{A} , formal charges \mathbf{Q} , hybridization states \mathbf{H} , and bond types \mathbf{B} . For brevity, Algorithms 1–2 detail only coordinates (continuous) and atom types (discrete, F categories); all other categorical features follow the identical discrete flow procedure.

Algorithm 1 Training (one step)

Require: Dataset $\mathcal{D} = \{(\mathcal{P}_i, l_{1,i})\}$, model f_θ

- 1: Sample (\mathcal{P}, l_1) from \mathcal{D} with $l_1 = (\mathbf{X}_1, \mathbf{A}_1, \dots)$
 - 2: Sample generation mode m (de novo, scaffold hopping, scaffold elaboration, linker inpainting, core/fragment growing, interaction-conditional)
 - 3: Extract fragment mask $\mathbf{m} \in \{0, 1\}^N$ ($m_i=1$: fixed; $m_i=0$: variable; $\mathbf{m}=\mathbf{0}$ for de novo)
 - 4: Sample priors: $\mathbf{X}_0 \sim \mathcal{N}(\mathbf{0}, \Sigma)$, $\mathbf{A}_0 \sim \text{Uniform}(\{1, \dots, F\})^N$ (one-hot) ▷ Σ : anisotropic or \mathbf{I}_3
 - 5: Overwrite fixed atoms: $\mathbf{X}_{0,i} \leftarrow \mathbf{X}_{1,i}$, $\mathbf{A}_{0,i} \leftarrow \mathbf{A}_{1,i} \forall i$ where $m_i=1$
 - 6: Optionally shift variable-atom prior to reference-ligand center of mass
 - 7: Sample $t \sim \mathcal{U}(0, 1)$; set $t_i \leftarrow 1$ for all fixed atoms ($m_i=1$)
 - 8: Interpolate: $\mathbf{X}_t = (1-t)\mathbf{X}_0 + t\mathbf{X}_1 + \sigma(t)\epsilon$, $\epsilon \sim \mathcal{N}(\mathbf{0}, \mathbf{I})$
 - 9: Unmask atom types: $A_{t,i} = A_{1,i}$ w.p. t , $A_{t,i} = A_{0,i}$ w.p. $1-t$ ▷ Independently per atom
 - 10: Forward: $(\hat{\mathbf{X}}_1, \hat{\mathbf{A}}_1) = f_\theta(l_t, t; \mathcal{P})$ ▷ Model predicts target l_1
 - 11: $\mathcal{L} = \lambda_c \text{MSE}(\hat{\mathbf{X}}_1, \mathbf{X}_1) + \lambda_t \text{CE}(\hat{\mathbf{A}}_1, \mathbf{A}_1) + \mathcal{L}_{\text{aux}}$ ▷ See $\mathcal{L}_{\text{total}}$ above
 - 12: Update $\theta \leftarrow \theta - \eta \nabla_\theta \mathcal{L}$
-

Algorithm 2 Sampling / Inference

Require: Pocket \mathcal{P} , optional fragment mask \mathbf{m} , num. atoms N , steps K , $\Delta t = 1/K$, model f_θ , coord. noise σ_c , inpainting frequency $N_{\text{inp}} \leq K$ (default K)

- 1: Construct $l^{(0)}$: $\mathbf{X}^{(0)} \sim \mathcal{N}(\mathbf{0}, \Sigma)$, $\mathbf{A}^{(0)} \sim \text{Uniform}(\{1, \dots, F\})^N$ (one-hot); initialize $t \leftarrow 0$
 - 2: If $\mathbf{m} \neq \mathbf{0}$: fix coordinates/types for atoms with $m_i=1$; set $t_i=1$
 - 3: **for** $k = 0, \dots, K-1$ **do**
 - 4: $(\hat{\mathbf{X}}_1, \hat{\mathbf{A}}_1) = f_\theta(l^{(k)}, t; \mathcal{P})$ ▷ $\hat{\mathbf{A}}_1 = \text{softmax}(\cdot)$
 - 5: $v_t^\theta = (\hat{\mathbf{X}}_1 - \mathbf{X}^{(k)}) / (1-t)$; $g_t = (t+\epsilon)^{-1} \mathbf{1}[t < t_c]$ ▷ Velocity; inv. noise sched.
 - 6: $\mathbf{X}^{(k+1)} = \mathbf{X}^{(k)} + \Delta t \cdot v_t^\theta$ ▷ Euler step (ODE, default)
 - 7: *or stochastic:* $s_t = \frac{t v_t^\theta - \mathbf{X}^{(k)}}{1-t}$; $\mathbf{X}^{(k+1)} = \mathbf{X}^{(k)} + \Delta t (v_t^\theta + g_t s_t) + \Delta t \sqrt{2g_t \sigma_c} \epsilon$, $\epsilon \sim \mathcal{N}(\mathbf{0}, \mathbf{I})$ ▷ SDE
 - 8: $P(\mathbf{A}^{(k+1)}=s \mid \mathbf{A}^{(k)}=j) = \begin{cases} \frac{\Delta t}{1-t} \hat{\mathbf{A}}_{1,s} & s \neq j \\ 1 - \sum_{s' \neq j} \frac{\Delta t}{1-t} \hat{\mathbf{A}}_{1,s'} & s = j \end{cases}$
 - 9: $\mathbf{A}^{(k+1)} \sim \text{Cat}(P)$ ▷ Discrete flow step
 - 10: If $\mathbf{m} \neq \mathbf{0}$ and $k \bmod \lfloor K/N_{\text{inp}} \rfloor = 0$: restore fixed atoms from fragment ▷ Periodic inpainting
 - 11: $t \leftarrow t + \Delta t$
 - 12: **end for**
 - 13: Final pass: $(\hat{\mathbf{X}}_1, \hat{\mathbf{A}}_1) = f_\theta(l^{(K)}, t \approx 1; \mathcal{P})$ ▷ Corrector step
 - 14: **return** $\hat{l}_1 = (\hat{\mathbf{X}}_1, \arg \max \hat{\mathbf{A}}_1)$
-

A.3 Inference-time scaling

Inference-time scaling is a powerful approach that allocates additional computation during generation, rather than solely relying on larger architectures [Snell et al., 2024, Setlur et al., 2024]. Originally developed for large language models,

this approach has been extended to diffusion and flow matching models. Diffusion models leverage stochasticity through particle sampling [Wu et al., 2023, Cremer et al., 2024] and Feynman-Kac steering [Singhal et al., 2025], where multiple trajectories are generated and resampled based on reward functions. Flow matching models, despite being deterministic, achieve inference-time scaling through SDE-based generation, interpolant conversion, and Rollover Budget Forcing (RBF) for adaptive resource allocation [Kim et al., 2025], improving upon diffusion-based advances [Ma et al., 2025].

In our work, we steer generative trajectories to sample from the conditional (target) distribution

$$p_\phi(l|y, P) \propto r(y|l, \mathcal{P})p_\theta(l|\mathcal{P}),$$

where y is a vector of properties such as binding affinity, and r represents a reward function that encodes user preferences.

Steering via Importance Sampling The target distribution is usually intractable, especially when applying neural generative models that transport samples over time, such as flow or diffusion models. One way to sample from the target distribution is to generate B particles and resample them based on importance weights derived from scores $\exp(\lambda r(y, l, \mathcal{P}))$, following the principle of importance sampling.

The sequential Monte Carlo (SMC) method [Del Moral et al., 2006] extends this concept to a time-sequential setting by maintaining B particles and updating their importance weights over time [Wu et al., 2023]. A straightforward weighting scheme involves evaluating the current batch of particles $\{l_{i,\tau}\}_{i=1}^B$ at time τ , computing their scores $\{\hat{y}_i = r(l_{i,\tau}, \mathcal{P})\}_{i=1}^B$, and obtaining resampling weights through softmax normalization: $w_i = \frac{\exp(\hat{y}_i)}{\sum_j \exp(\hat{y}_j)}$. Particles are then resampled from the discrete distribution $\{l_i\}_{i=1}^B \sim \text{Multinomial}(B, w = (w_1, w_2, \dots, w_B))$ with probability proportional to their weights, as done in PILOT [Cremer et al., 2024].

A.4 Quantum Mechanical Calculations on Protein-Ligand Complexes

To benchmark FLOWR.ROOT’s affinity prediction head, we perform quantum mechanical (QM) calculations on protein-ligand complexes and correlate the results with predicted affinities. Calculations were conducted using ULYSSES [Menezes and Popowicz, 2022], a general-purpose semi-empirical library offering multiple molecular Hamiltonians. We employ GFN2-xTB [Bannwarth et al., 2019] with ALPB aqueous solvation [Ehlert et al., 2021]. GFN2-xTB is a simplified density functional method that parametrizes interparticle interaction integrals against reference data, significantly accelerating calculations [Bannwarth et al., 2019]—a critical advantage for large atomic systems such as protein-ligand complexes. Additionally, GFN2-xTB provides a balanced treatment of electrostatic interactions and incorporates state-of-the-art dispersion corrections, enabling accurate descriptions of non-bonded complexes. In this work, the QM validation of FLOWR.ROOT used full protein domains, containing over 5000 atoms. Such a system size, required for meaningful physics-based evaluations of the granular details distinguishing different ligands, necessitates using semi-empirical Hamiltonians. Further, we only consider non-covalent binders, and, for such cases, intermolecular interactions are treated at a level similar to full Density Functional Theory (DFT). Finally, we found in previous work that GFN2-xTB provides accurate evaluations of protein-ligand complexes, in agreement with experimental SAR data [Grygier et al., 2023, Nowacki et al., 2025, Góral et al., 2024, Grygier et al., 2025].

Regarding the choice of GFN2-xTB for non-covalent protein-ligand binding energetics: (1) The SQM2.20 method demonstrated strong correlations between semi-empirical QM-derived binding energies and experimental data for multiple targets including BACE1, which we also investigate—notably, such correlations were not observed with force-field approaches or contemporary ML scoring functions [Pecina et al., 2024]. (2) GFN2-xTB was explicitly parameterized using non-covalent interaction datasets, employing the D4 dispersion correction and an updated electrostatics model [Bannwarth et al., 2019], making it particularly suited for non-bonded interactions that dominate protein-ligand binding. (3) Large QM regions are essential for reliably capturing binding energetics and selectivity effects; for example, DYRK1A and DYRK1B are highly homologous kinases (over 85% sequence identity), and treating only small binding-site regions would be insufficient to distinguish relative affinities. We emphasize that the QM calculations serve as an independent validation of predicted affinity trends rather than absolute binding energies.

Benchmark calculations on protein complexes extracted from the Schrödinger FEP dataset already contained protonated protein structures. For these cases, FLOWR.ROOT-generated ligands had to be protonated using open babel [O’Boyle et al., 2011]. Calculations were run on the full complexes, water molecules were excluded and solvation was treated only implicitly, except when otherwise stated. In the case of the kinase selectivity test, structures were extracted directly from the PDB and processed with open babel. This includes protonation of the protein pockets and of all ligands, along with their predicted total charges.

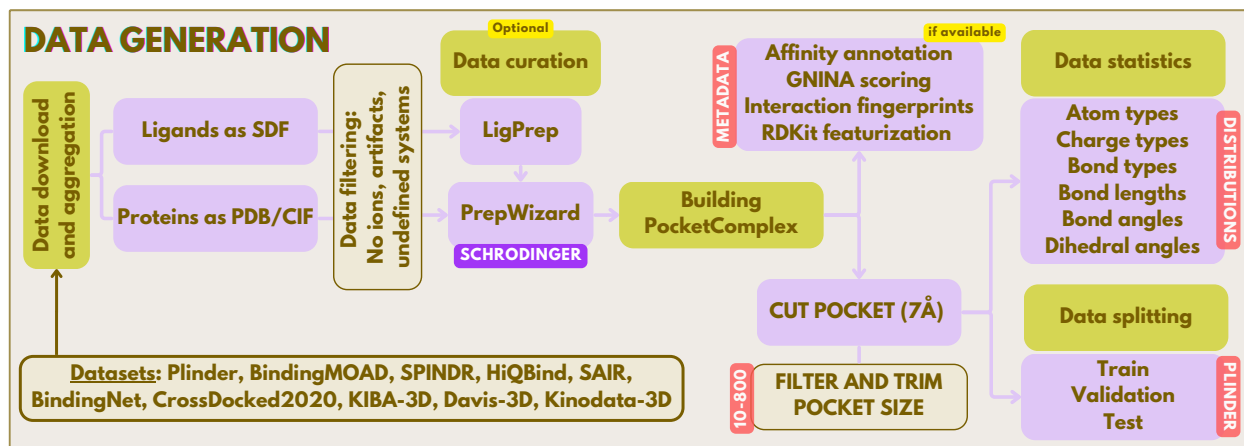


Figure 9: **Overview of the dataset generation pipeline used in this work.** Dataset generation workflow comprising data filtering, curation via Schrodinger’s LigPrep and PrepWizard, building of metadata-annotated internal representation, and calculation of molecule statistics.

A.5 Datasets

To comprehensively train and evaluate FLOWR.ROOT for structure-aware ligand design, we leverage a diverse collection of public datasets spanning both small molecules and biomolecular complexes. Our dataset selection encompasses three primary categories: (1) large-scale small molecule databases for training conformational and chemical diversity, (2) large-scale computationally generated datasets that bridge the gap between available experimental data and the scale and augmentation required for deep learning applications, and (3) small-scale experimental protein-ligand complex datasets for higher-fidelity structure-based modeling. This multi-faceted approach ensures robust model training across diverse chemical, conformational, and biological/bio-activity spaces while maintaining high structural quality standards.

For our small molecule database, we utilized Zinc3D, PubChem3D, Enamine REAL, and OMol25. For our protein-ligand database, we assembled a comprehensive collection of protein-ligand complex datasets by aggregating and standardizing data from multiple sources, including Plinder, BindingMOAD, SPINDR, HiQBind, SAIR, BindingNet, CrossDocked2020, KIBA-3D, Davis-3D, and Kinodata-3D. As visualized in Fig. 9, after rigorous preprocessing, filtering, and preparation of both ligands and proteins, each complex was converted into a unified internal representation and annotated with extensive metadata, such as affinity values, if available, and molecular descriptors. This harmonized dataset enables systematic analysis of chemical composition, structural diversity, and affinity distributions across all included sources, providing a robust foundation for downstream modeling and benchmarking.

While SPINDR and HiQBind provide preprocessed and well-curated co-crystal data resources, we applied additional comprehensive curation to selected datasets, namely Plinder, BindingMoad, SAIR, KIBA-3D and Davis-3D using Schrödinger’s LigPrep and PrepWizard tools. We used LigPrep to generate multiple protonated molecular conformations considering among other things different tautomeric states at physiological pH (7.4 ± 2.0), utilizing the OPLS4 force field and Epik for accurate pK_a prediction aligned with the reference ligand via the maximum common substructure (MCS). PrepWizard handled protein preparation through side chain completion, protonation state determination using Epik and PROPKA, termini capping, water molecule sampling within 10.0 \AA , constrained hydrogen and overall restrained minimization (0.3 \AA RMSD tolerance) using the S-OPLS force field. Unless otherwise stated, protein pockets were extracted using a 7 \AA cutoff radius around the respective reference ligands, with constraints of a minimum of 10 and maximum of 800 pocket atoms per complex to ensure computational tractability while preserving essential binding site information.

Importantly, throughout all protein-ligand datasets we kept a consistent dataset split following the provided Plinder [Durrain et al., 2024] train, validation and test set splits to avoid data leakage as best as possible enabling a stringent downstream evaluation. For more details about the datasets we refer to Appendix A.5, where we provide an overview of the aforementioned dataset generation, curation, and preprocessing pipeline, and a set of different dataset statistics.

Zinc3D Zinc3D [Irwin et al., 2020] is a subset of the ZINC20 database containing pre-computed low-energy conformations for commercially available compounds. By providing ready-to-use 3D structures, ZINC3D eliminates

the computational overhead of on-the-fly conformer generation, thereby accelerating virtual screening campaigns and structure-based drug discovery workflows. We utilized 646,663,126 molecules with their provided conformations.

PubChem3D PubChem3D Bolton et al. [2011] extends the widely-used PubChem database by providing up to 500 computed 3D conformations for millions of bioactive compounds. This resource offers extensive conformational diversity, crucial for training robust generative models. We employed 10 conformations per molecule from approximately 93 million compounds, resulting in 928,649,525 total conformations.

Enamine REAL The Enamine REAL database comprises commercially available, synthetically accessible compounds widely employed in virtual screening and drug design. Its well-curated chemical space supports generative design strategies focused on drug-likeness and synthetic feasibility. Following Cremer et al. [2024], we used a diversity subset of the Enamine REAL database. We employed OpenEye’s Omega software with default parameters to generate up to five conformers per molecule, yielding 111,389,149 conformations.

OMol25 OMol25 [Levine et al., 2025] is a comprehensive dataset containing over 100 million density functional theory (DFT) calculations at the ω B97M-V/def2-TZVPD level of theory. The dataset covers systems up to 350 atoms with exceptional chemical and structural diversity across 83 elements. We utilized two subsets: the small molecules collection (21,352,259 structures) comprising recomputed versions of widely-used datasets (ANI-2X, Orbnet Denali, SPICE2, Solvated Protein Fragments, and 30% of GEOM) upgraded to consistent high-level DFT theory, and the biomolecules subset (5,180,233 structures), encompassing protein-ligand interactions derived from BioLiP2 and additional complexes generated through docking drug-like molecules from GEOM, ChEMBL, and ZINC20. The biomolecule dataset features protein pocket environments processed through molecular dynamics simulation with appropriate capping and protonation state sampling.

KIBA-3D We introduce KIBA-3D, a kinase-focused dataset derived from the KIBA bioactivity dataset Tang et al. [2014a]. Using Schrödinger’s Glide, we performed exhaustive cross-docking of the KIBA ligand space across 172 kinase targets, generating 333,670 protein–ligand complexes spanning 2,038 unique ligands. This dataset provides a dense bioactivity landscape ideally suited for affinity guided, pocket-conditioned generative modeling and kinase-specific benchmarking applications.

Davis-3D DAVIS-3D is a structurally augmented version of the original DAVIS kinase bioactivity dataset [Davis et al., 2011], created as part of the Folding-Docking-Affinity (FDA) framework [Wu et al., 2025]. The dataset was generated by computationally folding protein structures using ColabFold and determining protein-ligand binding conformations through DiffDock, a deep learning-based docking model. This process transforms the original sequence-based DAVIS dataset into a collection of three-dimensional protein-ligand binding structures, of which we utilized 12,982 complexes with binding affinities.

Kinodata-3D Kinodata-3D [Backenköhler et al., 2024] is a curated collection of kinase complexes processed using cross-docking methodologies. We utilized 94,211 complexes from the combined mid- to higher-confidence subsets, which include binding affinity annotations and are preprocessed with a 5 Å protein-ligand pocket cutoff.

BindingNet BindingNet [Li et al., 2024, Zhu et al., 2025] comprises 689,796 modeled protein-ligand binding complexes across 1,794 protein targets. The dataset was constructed using an enhanced template-based modeling workflow that incorporates pharmacophore and molecular shape similarities alongside chemical similarity. Structures are categorized by template matching quality into high-confidence (232,030), moderate-confidence (164,912), and low-confidence (292,813) subsets, all of which we employed with their respective binding affinity annotations.

Plinder Plinder [Durairaj et al., 2024] represents the largest and most comprehensively annotated protein-ligand interaction (PLI) dataset, containing 449,383 PLI systems with over 500 annotations per complex. The dataset encompasses diverse interaction types including multi-ligand systems, oligonucleotides, peptides, and saccharides. Plinder introduced an approach for generating training and evaluation splits that minimizes task-specific leakage while maximizing test set quality. After removing complexes containing ligand artifacts, ions, or undefined ligands, and processing using Schrödinger’s LigPrep and PrepWizard, we utilized 250,633 protein-ligand systems.

SAIR The Structurally Augmented IC50 Repository (SAIR) [Lemos et al., 2025] is the largest publicly available dataset of protein-ligand 3D structures with binding affinity annotations, addressing the scarcity of high-quality experimental structures for deep learning applications. The original dataset contains 5,244,285 computationally generated structures across 1,048,857 unique protein-ligand systems from ChEMBL and BindingDB, with structures

folded using the Boltz-1x model [Wohlwend et al., 2024]. We applied stringent filtering criteria, retaining only PoseBusters-valid [Buttenschoen et al., 2024] complexes with negative AutoDock-Vina scores [Eberhardt et al., 2021], confidence scores ≥ 0.8 , interaction PTM ≥ 0.6 , and IPTM ≥ 0.8 , yielding 1,781,634 complexes. Further processing using Schrödinger’s LigPrep and PrepWizard resulted in 1,564,677 curated complexes with IC50 annotations.

BindingMOAD BindingMOAD [Hu et al., 2005] is a comprehensive database developed over two decades (2001-2025), containing 41,409 protein-ligand complexes with affinity coverage for 15,223 complexes (37%) and 20,387 unique ligands. After preprocessing with Schrödinger’s LigPrep and PrepWizard, we obtained 33,286 complexes with diverse binding affinity annotations.

SPINDR SPINDR [Cremer et al., 2025] is a higher-fidelity dataset of protein–ligand complexes curated for interaction-aware modeling. The dataset emphasizes accurate binding site geometries and ligand poses, supporting physically consistent generative modeling. Complexes are thoroughly cleaned to focus on drug-like, non-covalent interactions using Schrödinger’s PrepWizard, with protein-ligand interactions annotated using ProLIF [Bouysset and Fiorucci, 2021]. We employed all 35,627 provided complexes with partial binding affinity annotations.

HiQBind HiQBind [Wang et al., 2025] is a curated dataset addressing structural artifacts in widely-used datasets, like PDBbind. Containing over 18,000 unique PDB entries and 30,000 protein-ligand complex structures, it matches binding free energies from BioLiP, Binding MOAD, and BindingDB with co-crystallized PDB complexes. The dataset employs strictly open-source curation tools with multiple quality control modules for steric clash detection, ligand structure fixing, protein completion, and hydrogen addition protocols. We utilized all 31,571 complexes with binding affinity annotations.

Schrodinger FEP+ dataset The Schrodinger FEP+ dataset [Ross et al., 2023b] comprises a large and diverse collection of protein-ligand complexes, each featuring congeneric series of small molecules with experimentally measured binding affinities (K_d , K_i , or IC_{50}). Designed as a benchmark for assessing the accuracy and reproducibility of free energy perturbation (FEP) methods, the dataset emphasizes high-quality structural data, including X-ray structures and carefully curated protein and ligand preparations. It covers a broad chemical space, including challenging cases such as macrocycles, charge-changing transformations, and buried water displacement. This dataset is intended to support the development, validation, and comparison of computational methods for predicting relative binding affinities, providing a robust foundation for downstream applications in drug discovery and molecular design.

A.5.1 Dataset Statistics

In Sec. A.5 in Fig. 9 we visualize the data generation framework that we established for this work. As outlined in Sec. A.5 we used as protein-ligand complex data Plinder, BindingMOAD, SPINDR, HiQBind, SAIR, BindingNet, CrossDocked2020, KIBA-3D, Davis-3D, and Kinodata-3D. After downloading and aggregating the different data sources, we split proteins and ligands, if not already done, into separate files. We save ligands as SDF and proteins as PDB or CIF files. Afterwards, we filter the data and remove systems that classify the ligands either as ions, artifacts or not definable. Then, we use Schrodinger’s LigPrep to prepare the ligands and Schrodinger’s PrepWizard to prepare the protein-ligand complex (see Sec. A.5 for more details). Successfully prepared systems are converted into our internal pocket-ligand representation encapsulated as PocketComplex instances for easy handling and data management. We retrieve pockets by cutting around the reference ligands with a cutoff of 7Å and, if necessary, trim the pocket to the max size of 800 atoms. Every PocketComplex instance is annotated with comprehensive metadata spanning affinity values (if available), GNINA scores, interaction fingerprints, and selected RDKit features, like molecular weight, logP, TPSA, number of hydrogen acceptors and donors, number of rotatable bonds, number of aliphatic rings and many more. Finally, for all datasets we calculate distribution statistics comprising atom, charge, and bond type distributions as well as bond angles, bond lengths and dihedral angles distributions. Importantly, all datasets are splitted following the Plinder train, validation and test splits.

In Fig. 10, we compared the chemical composition of all protein–ligand datasets used in this work by analyzing the distributions of ligand atom types, protein atom types, and protein residue types. The aggregated distributions (top row) reveal the overall prevalence of each type, while the per-dataset heatmaps (bottom row) illustrate how these distributions vary between datasets. For atom types, a logarithmic scale was used to emphasize less frequent elements. Only the 20 standard amino acids were considered for residue type comparisons, and hydrogens were excluded from atom type analyses to improve interpretability.

To provide a comprehensive overview of the affinity data, Fig. 11 summarizes both the distribution and coverage of affinity types across all datasets. The ECDFs display the range and distribution of affinity values for each affinity type, highlighting differences in spread and modality. The overall affinity type counts, presented on a logarithmic scale,

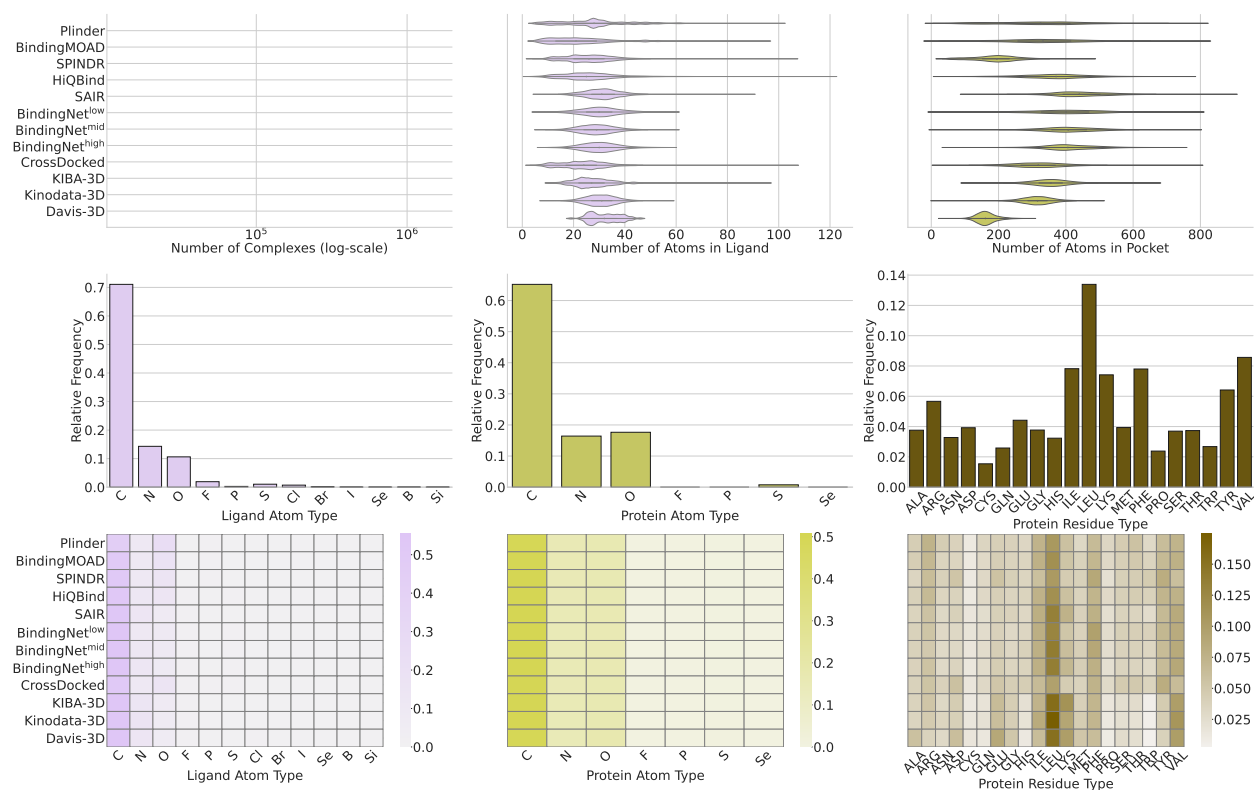


Figure 10: Dataset chemistry statistics. Distributions of ligand atom types, protein atom types, and protein residue types across multiple datasets. We show normalized frequencies of each type aggregated over all datasets, and per-dataset distributions visualized as heatmaps (logarithmic scale for atom types), highlighting differences in composition between datasets. Only the 20 standard amino acids are shown for residue types; hydrogens are excluded from atom type analyses.

reveal a pronounced imbalance, with IC50 being the most abundant. Dataset-specific distributions are visualized using horizontal violin plots, while horizontal bar plots summarize the number of measurements for each affinity type within each dataset. The majority of affinity values originate from the SAIR and BindingNet datasets. Notably, BindingNet also provides Ki measurements, while HiQBind and BindingMOAD offer a balanced representation of IC50, Ki, and Kd values. HiQBind is the only dataset containing EC50 measurements. In contrast, Davis-3D is exclusively annotated with Kd values. This overview facilitates the identification of data biases and gaps that may influence downstream analyses.

To systematically assess the chemical diversity of ligands across datasets, we analyzed the distributions of several continuous molecular descriptors in Fig. 12, including molecular weight, logP, molar refractivity, and topological polar surface area (TPSA). These features capture key aspects of ligand size, hydrophobicity, polarizability, and polarity, which are relevant for molecular recognition and drug-likeness. The results reveal pronounced differences between datasets: for example, BindingNet and SAIR contain ligands with a broader range of molecular weights and higher TPSA values, while datasets such as HiQBind and BindingMOAD exhibit more constrained distributions. These trends reflect the varying selection criteria and source domains of the datasets, and highlight the importance of considering chemical diversity in benchmarking and model development.

We further characterized the datasets by comparing the distributions of discrete ligand features in Fig. 13, including the number of hydrogen bond acceptors and donors, rotatable bonds, ring systems, and chiral centers. These properties provide insight into molecular complexity, flexibility, and the presence of functional groups relevant for binding interactions. The analysis demonstrates that datasets such as BindingNet and SAIR encompass ligands with higher numbers of rotatable bonds and greater ring system diversity, whereas datasets like Davis-3D and KIBA-3D are more restricted in these aspects. Notably, the number of chiral centers and structural alerts also varies substantially, underscoring differences in stereochemical complexity and potential reactivity. Together, these comparisons elucidate the distinct chemical spaces sampled by each dataset and inform the interpretation of downstream modeling results.

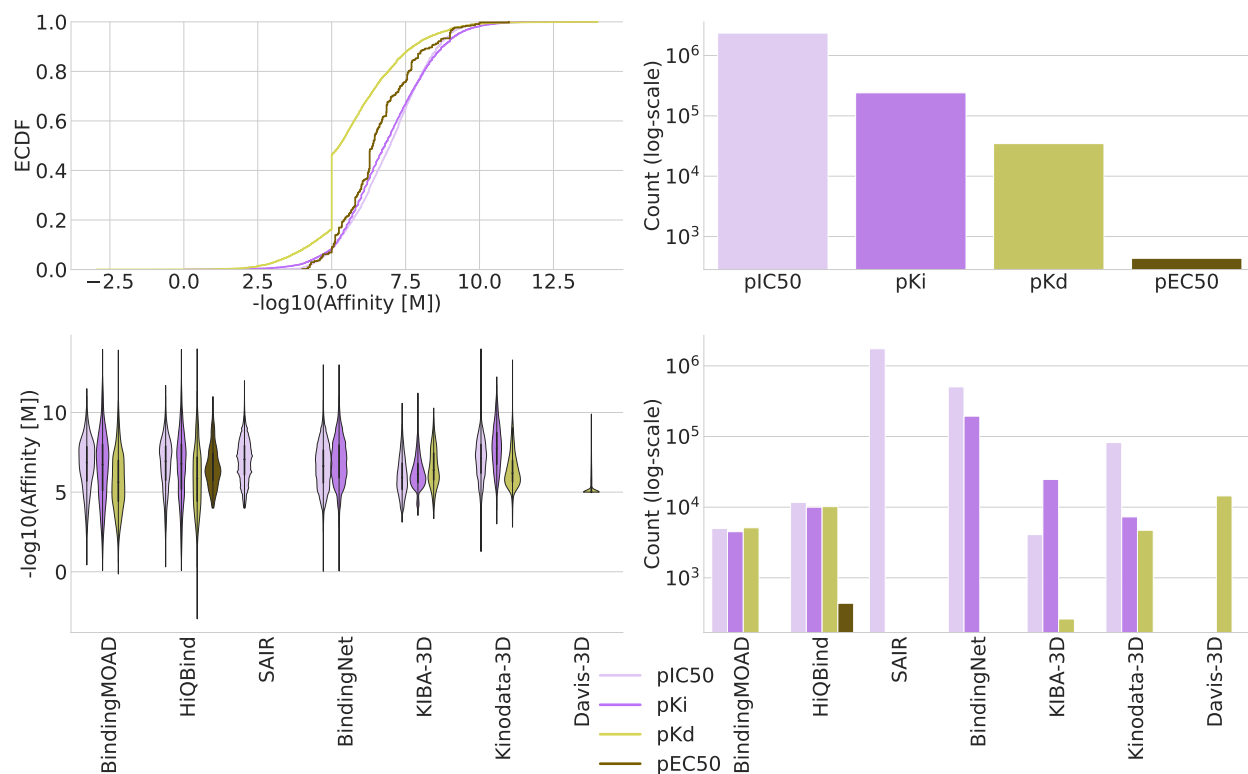


Figure 11: **Dataset affinity statistics.** Overview of affinity data distributions and dataset coverage. We show empirical cumulative distribution functions (ECDFs) of affinity values for each affinity type across all datasets; overall counts of each affinity type (log scale); and distribution of affinity values per dataset and affinity type (horizontal violin plots), as well as affinity type counts per dataset (horizontal bar plots, log scale). Legend indicates affinity type color coding used throughout all plots.

A.5.2 KIBA-3D

The KIBA dataset was originally introduced by Tang *et al.* [Tang *et al.*, 2014b] as a large-scale benchmark for kinase–ligand binding affinity prediction, integrating heterogeneous bioactivity readouts into a standardized KIBA score. The original dataset contained 52,498 chemical compounds, 467 kinase targets and over 240,000 interaction records. While comprehensive, the original KIBA dataset was highly scattered, due to an imbalance between the number of ligand-kinase pairs and associated measurements. To improve the density and ensure more reliable evaluation, subsequent studies discarded the ligands and targets with less than 10 interaction records. This procedure reduced the dataset to 2,094 ligands and 229 kinase targets. For this work, we prepared the 3D extension of KIBA (KIBA-3D) based on kinase targets with experimentally solved structures deposited in the PDB. Figure 14 shows examples of our docking results, illustrating that Glide could reproduce near-native binding poses for selected kinase inhibitors with conserved bidentate hydrogen bond pattern in the hinge region (e.g., PDBID:2XB7-CHEMBL461876, glide gscore -11.4 , PDBID:6LVM-CHEMBL1968590, glide gscore -11.9). The KIBA-3D dataset serves as a large-scale, structure-consistent benchmark for evaluating generative and predictive models.

Target protein structure selection for KIBA-3D Kinase targets from the KIBA dataset were mapped to their UniProt identifiers. For each UniProt accession, X-ray crystal structures were selected according to a set of heuristics to ensure biological relevance of the binding site. Only entries covering the kinase domain were considered. Among the available structures, the highest resolution one was chosen, with preference for holo over apo forms. Complexes with ATP, ADP, or staurosporine were deprioritized, as these ligands tend to stabilize non-representative conformations of the binding pocket; in particular, staurosporine, aside from being a highly promiscuous kinase inhibitor has a flat shape that inflates the catalytic site and biases the pocket toward accommodating larger ligands. Structures with fewer missing residues were favored, and cases where the bound small molecule occupied an allosteric or noncanonical pocket were excluded. The resulting curated set provides 174 kinase structures suitable for docking of the KIBA ligand set.

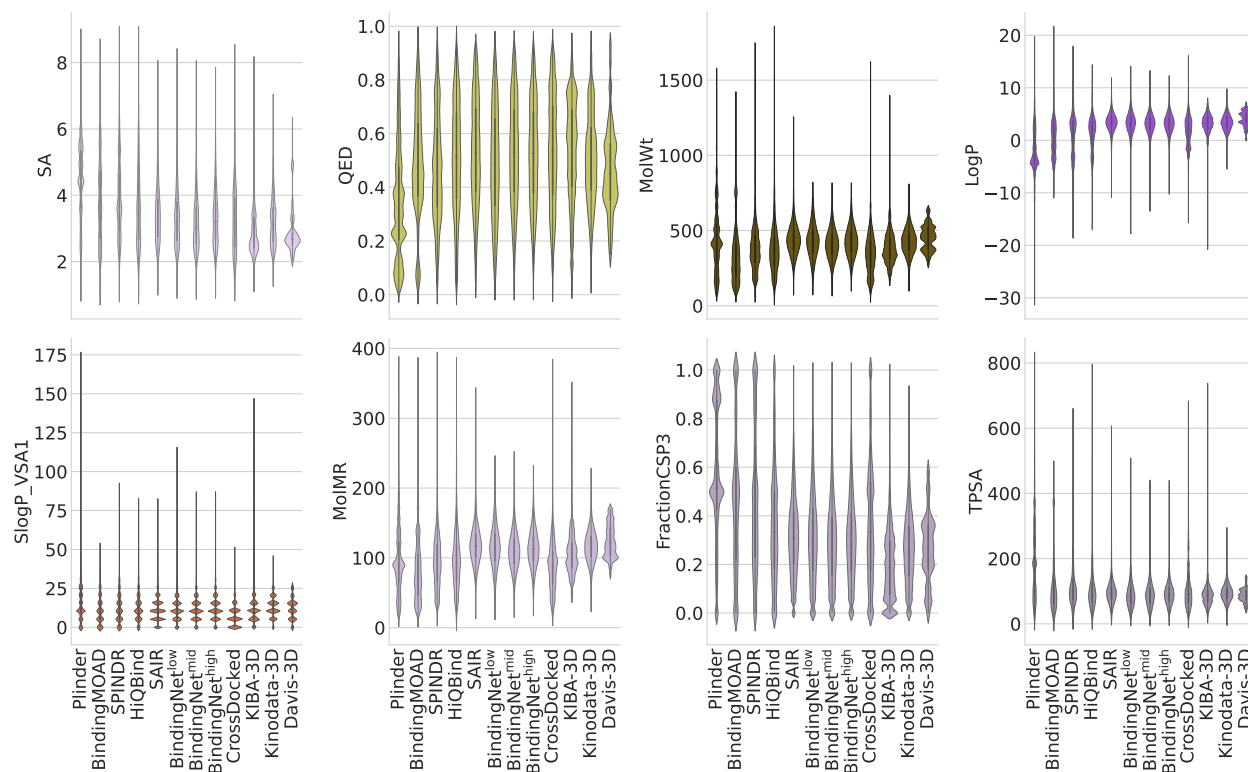


Figure 12: **Dataset property statistics.** Comparison of key continuous molecular properties of ligands—including molecular weight, logP, molar refractivity, and topological polar surface area—across all datasets. The distributions reveal substantial variability in ligand size, polarity, and hydrophobicity, reflecting the chemical diversity and distinct selection criteria of each dataset.

Docking We performed docking with the Maestro suite (Schrödinger Release 2023-2: Maestro, Schrödinger, LLC, New York, NY, 2023) to generate consistent protein–ligand complexes across the 174 kinase targets. Small molecules were first optimized with LigPrep. All the 2094 ligands were processed. The dataset covers a broad chemical space, with molecular weights ranging from 180.15 to 1381.64 Da (median 376.49 Da). Protein structures were processed using the Protein Preparation Workflow, including protonation with Epik and propka [Johnston et al., 2023] and restrained minimization with the OPLS4 force field [Sastry et al., 2013]. Missing residues were built with Prime. Docking grids were centered on the kinase domain’s hinge region, covering the canonical ATP-binding pocket used by first-type kinase inhibitors. Docking was performed with the Glide SP protocol [Yang et al., 2021], with no constraints applied, generating one pose per ligand.

B Additional results

B.1 GEOM-Drugs and CrossDocked2020 Benchmarks

Complete benchmark results on the unconditional GEOM-Drugs dataset and pocket-conditional CrossDocked2020 dataset are provided below, demonstrating that FLOWR.ROOT achieves state-of-the-art performance across chemical validity, geometric accuracy, and energetic stability metrics.

On the GEOM-DRUGS dataset, FLOWR.ROOT achieves a PoseBusters-validity of 94.0%, surpassing all other models including FLOWMOL3 (91.9%). The model demonstrates exceptional geometric precision with a median relaxation RMSD of only 0.07 Å, significantly lower than all baselines. The relaxation energy of 3.65 kcal/mol indicates that generated conformations are close to local energy minima.

On CROSSDOCKED2020, FLOWR.ROOT achieves a PoseBusters-validity of 0.97, surpassing all models including the test set reference (0.95). The strain energy of 67.13 kcal/mol is significantly lower than FLOWR (87.83) and PILOT (110.48), indicating energetically favorable binding poses. FLOWR.ROOT also achieves the best AutoDock-Vina score of -7.76 kcal/mol while maintaining efficient inference times (15.43s per ligand).

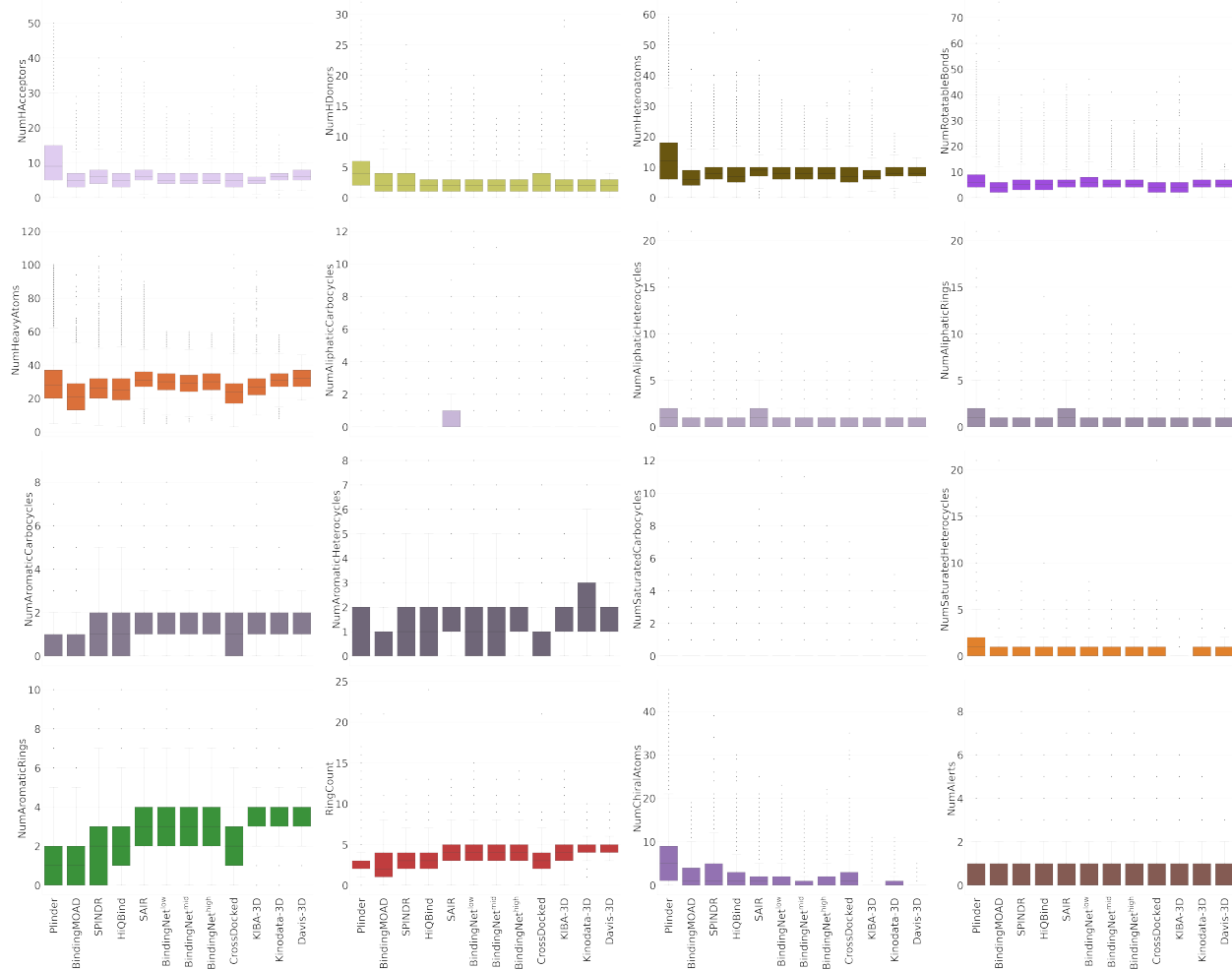


Figure 13: **Dataset property statistics.** Comparison of the distributions of discrete ligand features such as hydrogen bond acceptors and donors, rotatable bonds, ring systems, and chiral centers for each dataset. The observed differences highlight variations in molecular complexity, flexibility, and functional group composition among the datasets, providing insight into their respective chemical spaces.

B.2 Pocket-conditional ligand generation: SPINDR

We evaluate the non-pretrained FLOWR.ROOT^{base} model across three conditional generation modes and compare against the corresponding FLOWR.MULTI [Cremer et al., 2025] baselines. For interaction-conditional generation, where the model is guided by predefined protein-ligand interactions, results are shown in Table 6. We also assess scaffold inpainting, where functional groups are provided as context and the model generates the core scaffold (Table 7). Conversely, for functional group inpainting, where the scaffold is given and the model decorates it with functional groups (Table 8).

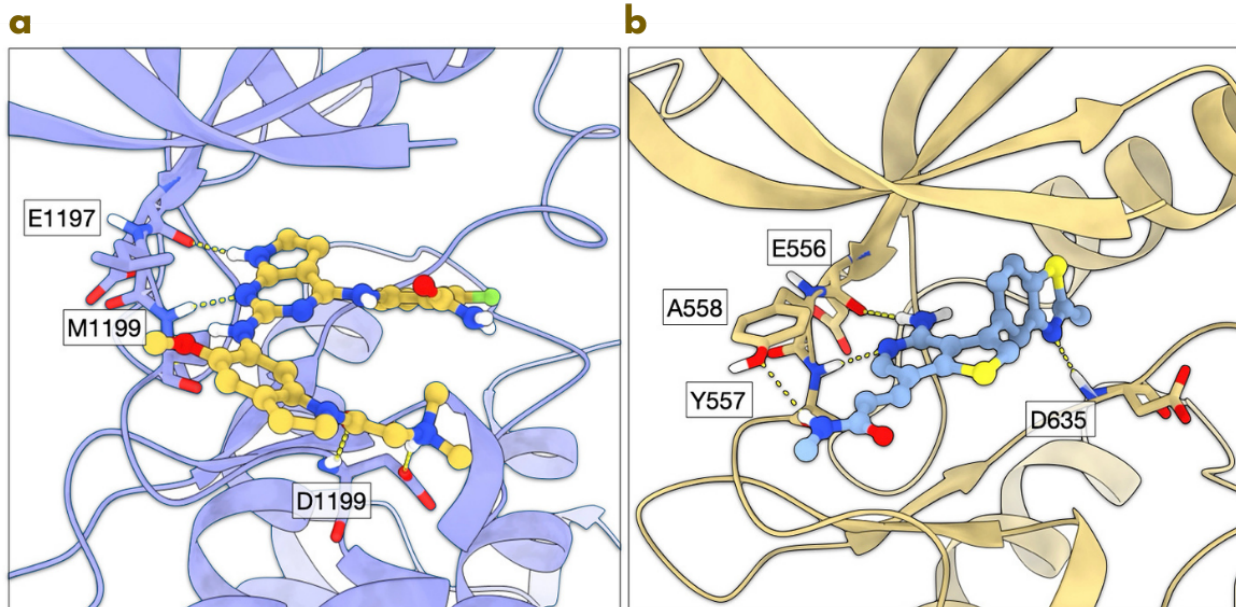


Figure 14: **Example visualizations of protein-ligand complexes in KIBA-3D.** **a** The structure of anaplastic lymphoma kinase (ALK, PDB ID: 2XB7, blue) with docked CHEMBL461876. The pyrrolopyrimidine moiety is positioned in the adenine region of the catalytic pocket, forming a bidentate hydrogen bond (yellow dashed lines) with the main chains of hinge residues Glu1197 and Met1199. **b** the structure of the tyrosine kinase fibroblast growth factor receptor 3 (FGFR3, PDB ID: 6LVM, yellow) accommodates an aminopyridine derivative (CHEMBL1968590) in a similar manner, with a conserved bidentate H-bond pattern in the hinge region (Glu556 and Ala558), complemented by an additional H-bond to the Tyr557 side chain. Furthermore, the nitrogen of the thiazole ring forms a hydrogen bond with Asp635 from the functional DFG motif. Both poses were favourable scored, with Glide docking score below -11 (-11.4 for the 2XB7-CHEMBL461876 complex and -11.9 for the 6LVM-CHEMBL1968590 complex)

Table 3: **Evaluation and comparison of FLOWR.ROOT unconditional base model on GEOM-DRUGS.** Benchmark comparison of the non-pretrained FLOWR.ROOT ligand-only base model against EQGAT-DIFF, ADIT, SEMLAFLOW, MEGALODON, FLOWMOL3 on the GEOM-DRUGS dataset. We follow the conventions in this field and sample 10,000 molecules with molecule sizes randomly sampled from the test set. We evaluate the performance of FLOWR.ROOT on RDKit- and PoseBusters-validity, the change in potential energy resulting from GFN2-xTB minimization (ΔE_{relax}) and the all-atom RMSD between the predicted and GFN2-xTB minimized conformations (Relax RMSD). All values denote the sample mean with the 95% confidence interval over five replicate runs with different seeds as subscripts. For ΔE_{relax} and Relax RMSD we report the median.

MODEL	RDKit-VALID(%) \uparrow	PB-VALID(%) \uparrow	ΔE_{relax} \downarrow	RELAX RMSD \downarrow	PARAMS (M)
EQGAT-DIFF	86.0 ± 0.9	77.6 ± 0.8	6.51 ± 0.16	0.60 ± 0.01	12
ADIT	99.9 ± 0.0	82.7 ± 0.8	79.32 ± 1.00	1.30 ± 0.02	150
SEMLAFLOW	95.5 ± 0.5	88.5 ± 1.3	31.9 ± 2.30	0.24 ± 0.03	40
MEGALODON	94.8 ± 0.3	86.6 ± 0.7	3.17 ± 0.11	0.41 ± 0.01	60
FLOWMOL3	99.9 ± 0.1	91.9 ± 0.7	3.83 ± 0.08	0.39 ± 0.01	6
FLOWR.ROOT ^{BASE} _{UNCOND.}	98.5 ± 0.2	94.0 ± 0.2	3.65 ± 0.07	0.07 ± 0.02	34
TRAIN SET	100.0 ± 0.0	93.2 ± 0.1	-	-	

Table 4: **Evaluation and comparison of FLOWR.ROOT base model on CROSSDOCKED2020.** Benchmark comparison of the non-pretrained FLOWR.ROOT base model against POCKET2MOL, TARGETDIFF, DIFFSBDD, PILOT, DRUGFLOW and FLOWR on the CROSSDOCKED2020 test dataset. We follow the conventions in this field and sample 100 ligands per test target, of which there are 100. We evaluate the most expressive metrics, namely PoseBusters-validity, GenBench3D strain energy, AutoDock-Vina scores and the Wasserstein distance of the generated ligands’ bond angles (BondA.W1) and bond lengths (BondL.W1) distributions relative to the test set.

MODEL	PB-VALID \uparrow	STRAIN \downarrow	VINA SCORE \downarrow	VINA SCORE ^{MIN} \downarrow	BONDA.W1 \downarrow	BONDL.W1 [10 ⁻²] \downarrow	SIZE	TIME (S) \downarrow
POCKET2MOL	0.76 \pm 0.39	147.22 \pm 61.41	-4.72 \pm 1.47	-5.80 \pm 1.26	2.04	0.66	17.04 \pm 4.11	2320 \pm 45
DIFFSBDD	0.38 \pm 0.46	519.03 \pm 251.32	-2.97 \pm 5.21	-4.71 \pm 3.30	7.00	0.51	24.85 \pm 8.94	160.31 \pm 73.30
TARGETDIFF	0.57 \pm 0.46	294.89 \pm 136.32	-5.20 \pm 1.79	-5.82 \pm 1.60	7.76	0.42	22.79 \pm 9.46	3228 \pm 121
DRUGFLOW	0.75 \pm 0.39	120.21 \pm 73.28	-5.66 \pm 1.78	-6.10 \pm 1.62	2.11	0.38	21.14 \pm 6.81	-
PILOT	0.83 \pm 0.33	110.48 \pm 87.47	-5.73 \pm 1.72	-6.21 \pm 1.65	1.75	0.33	22.58 \pm 9.77	295.42 \pm 117.35
FLOWR	0.92 \pm 0.22	87.83 \pm 74.30	-6.29 \pm 1.56	-6.48 \pm 1.45	0.96	0.27	22.28 \pm 9.78	12.05 \pm 8.01
FLOWR.ROOT ^{BASE}	0.97 \pm 0.22	67.13 \pm 53.05	-7.76 \pm 0.55	-7.93 \pm 0.42	0.91	0.22	22.41 \pm 8.95	15.43 \pm 6.22
TEST SET	0.95 \pm 0.21	75.62 \pm 57.29	-6.44 \pm 2.74	-6.46 \pm 2.61	-	-	22.75 \pm 9.90	-

Table 5: **Benchmark of the (non-pretrained) FLOWR.ROOT^{base} model against FLOWR on the SPINDR test set.** FLOWR.ROOT^{base} denotes a base model with $\sim 1.5x$ the number of parameters to see the effect of model scaling on the SPINDR dataset. We report RDKit- and PoseBusters-validity of generated ligands, the GenBench3D strain energy and the AutoDock-Vina score. We also state the Wasserstein distance of generated ligands for the bond angles and bond lengths distribution to the SPINDR test set. Novelty, uniqueness and diversity measure the capability of the model to explore the chemical space both in 2D and 3D with the latter evaluating uniqueness and diversity of conformers of the same molecule (Note: if the list of generated ligands for a target contains duplicated molecules, otherwise they become zero). RDKit’s QED evaluation, SAScore, the molecular weight as well as the logP values evaluate drug-likeness of generated ligands. All presented values are mean values taken for 100 sampled ligands per test set target. The test dataset comprises 225 test set targets. Note, both RDKit- and PoseBusters-validity are evaluated on the raw generated set of 100 ligands per target. All other metrics are calculated on the subset of RDKit-valid ligands.

METRIC	TEST SET	FLOWR	FLOWR.ROOT ^{BASE}	FLOWR.ROOT ^{BASE} _{LARGE}
RDKit-VALIDITY	1.00 \pm 0.00	0.94 \pm 0.24	0.98 \pm 0.13	0.98 \pm 0.14
PB-VALIDITY	0.99 \pm 0.02	0.88 \pm 0.21	0.97 \pm 0.10	0.98 \pm 0.09
STRAIN ENERGY	43.27 \pm 41.85	90.05 \pm 52.18	50.36 \pm 34.59	47.67 \pm 34.59
VINA SCORE	-7.69 \pm 2.00	-6.93 \pm 0.92	-7.52 \pm 0.84	-7.56 \pm 0.85
VINA SCORE (MINIMIZED)	-7.88 \pm 2.00	-7.22 \pm 0.92	-7.71 \pm 0.85	-7.74 \pm 0.85
BONDANGLESW1	-	1.08	0.60	0.68
BONDLENGTHSW1 [10 ⁻²]	-	0.35	0.43	0.40
NOVELTY	1.00 \pm 0.00	0.94 \pm 0.23	1.00 \pm 0.00	1.00 \pm 0.00
UNIQUENESS2D	0.92 \pm 0.10	0.94 \pm 0.13	0.89 \pm 0.18	0.89 \pm 0.18
UNIQUENESS3D	-	0.50 \pm 0.20	0.45 \pm 0.22	0.43 \pm 0.18
DIVERSITY2D	0.92 \pm 0.04	0.86 \pm 0.05	0.83 \pm 0.10	0.82 \pm 0.09
DIVERSITY3D	-	0.21 \pm 0.12	0.13 \pm 0.11	0.12 \pm 0.11
SA	0.66 \pm 0.12	0.67 \pm 0.13	0.67 \pm 0.14	0.66 \pm 0.14
QED	0.49 \pm 0.22	0.52 \pm 0.21	0.49 \pm 0.20	0.50 \pm 0.20
RINGS	2.98 \pm 1.42	2.68 \pm 1.35	3.33 \pm 1.52	3.41 \pm 1.56
AROMATIC RINGS	1.84 \pm 1.31	1.52 \pm 1.16	2.07 \pm 1.39	2.13 \pm 1.35
HACCEPTORS	7.30 \pm 4.49	6.67 \pm 4.23	7.36 \pm 4.78	7.39 \pm 4.79
HDONORS	2.62 \pm 1.68	2.52 \pm 1.68	2.49 \pm 1.67	2.50 \pm 1.65
LOGP	0.29 \pm 3.48	0.29 \pm 3.31	0.59 \pm 3.52	0.54 \pm 3.45
MOLWT	390.43 \pm 119.82	350.10 \pm 114.00	384.26 \pm 121.50	384.45 \pm 121.68
LIPINSKI	4.00 \pm 1.34	4.35 \pm 1.05	4.25 \pm 1.11	4.27 \pm 1.10

Table 6: **Benchmark of the (non-pretrained) FLOWR.ROOT^{base} model against FLOWR.MULTI running interaction-/pharmacophore-conditional generation on the SPINDR test set.** Given ligand atoms forming interactions with the protein pocket as context, the model generates the remaining structure. We report RDKit- and PoseBusters-validity of generated ligands, the GenBench3D strain energy and the AutoDock-Vina score. We also state the Wasserstein distance of generated ligands for the bond angles and bond lengths distribution to the SPINDR test set. Novelty, uniqueness and diversity measure the capability of the model to explore the chemical space both in 2D and 3D with the latter evaluating uniqueness and diversity of conformers of the same molecule (Note: if the list of generated ligands for a target contains duplicated molecules, otherwise they become zero). RDKit’s QED evaluation, SAScore, the molecular weight as well as the logP values evaluate drug-likeness of generated ligands. All presented values are mean values taken for 100 sampled ligands per test set target. The test dataset comprises 225 complexes. Note, both RDKit- and PoseBusters-validity are evaluated on the raw generated set of 100 ligands per target. All other metrics are calculated on the subset of RDKit-valid ligands.

METRIC	TEST SET	FLOWR.MULTI ^{interact.-cond.}	FLOWR.ROOT ^{BASE} _{interact.-cond.}
RDKIT-VALIDITY	1.00 \pm 0.00	0.93 \pm 0.25	0.98 \pm 0.15
PB-VALIDITY	0.99 \pm 0.02	0.86 \pm 0.19	0.95 \pm 0.11
STRAIN ENERGY	43.27 \pm 41.85	107.60 \pm 93.07	56.60 \pm 43.19
VINA SCORE	-7.69 \pm 2.00	-7.18 \pm 0.83	-7.57 \pm 0.67
VINA SCORE (MINIMIZED)	-7.88 \pm 2.00	-7.48 \pm 0.80	-7.82 \pm 0.68
BONDANGLESW1	-	1.17	0.61
BONDLENGTHSW1 [10^{-2}]	-	0.43	0.37
NOVELTY	1.00 \pm 0.00	0.93 \pm 0.26	1.00 \pm 0.00
UNIQUENESS2D	0.92 \pm 0.10	0.83 \pm 0.26	0.74 \pm 0.32
UNIQUENESS3D	-	0.40 \pm 0.21	0.36 \pm 0.21
DIVERSITY2D	0.92 \pm 0.04	0.82 \pm 0.08	0.79 \pm 0.10
DIVERSITY3D	-	0.06 \pm 0.07	0.09 \pm 0.08
SA	0.66 \pm 0.12	0.67 \pm 0.13	0.66 \pm 0.13
QED	0.49 \pm 0.22	0.50 \pm 0.21	0.49 \pm 0.20
RINGS	2.98 \pm 1.42	2.98 \pm 1.38	3.33 \pm 1.52
AROMATIC RINGS	1.84 \pm 1.31	1.79 \pm 1.22	2.05 \pm 1.34
HACCEPTORS	7.30 \pm 4.49	7.23 \pm 4.44	7.25 \pm 4.60
HDONORS	2.62 \pm 1.68	2.75 \pm 1.58	2.72 \pm 1.56
LOGP	0.29 \pm 3.48	0.41 \pm 3.43	0.35 \pm 3.44
MOLWT	390.43 \pm 119.82	379.85 \pm 115.96	382.45 \pm 117.86
LIPINSKI	4.00 \pm 1.34	4.29 \pm 1.11	4.31 \pm 1.08

Table 7: **Benchmark of the (non-pretrained) FLOWR.ROOT^{base} model against FLOWR.MULTI on the SPINDR test set for scaffold hopping.** Given functional groups as context, the model generates the remaining scaffold structure. We report RDKit- and PoseBusters-validity of generated ligands, the GenBench3D strain energy and the AutoDock-Vina score. We also state the Wasserstein distance of generated ligands for the bond angles and bond lengths distribution to the SPINDR test set. Novelty, uniqueness and diversity measure the capability of the model to explore the chemical space both in 2D and 3D with the latter evaluating uniqueness and diversity of conformers of the same molecule (Note: if the list of generated ligands for a target contains duplicated molecules, otherwise they become zero). RDKit’s QED evaluation, SAScore, the molecular weight as well as the logP values evaluate drug-likeness of generated ligands. All presented values are mean values taken for 100 sampled ligands per test set target. The test dataset comprises 225 test set targets. Note, both RDKit- and PoseBusters-validity are evaluated on the raw generated set of 100 ligands per target. All other metrics are calculated on the subset of RDKit-valid ligands.

METRIC	TEST SET	FLOWR.MULTI ^{SCAFFOLD-INPAINT}	FLOWR.ROOT ^{BASE} _{SCAFFOLD-INPAINT}
RDKit-VALIDITY	1.00 ± 0.00	0.92 ± 0.26	0.98 ± 0.14
PB-VALIDITY	0.99 ± 0.02	0.86 ± 0.17	0.95 ± 0.12
STRAIN ENERGY	43.27 ± 41.85	105.32 ± 95.47	56.40 ± 44.10
VINA SCORE	-7.69 ± 2.00	-7.10 ± 0.71	-7.27 ± 0.63
VINA SCORE (MINIMIZED)	-7.88 ± 2.00	-7.34 ± 0.72	-7.51 ± 0.64
BONDANGLESW1	-	1.14	0.46
BONDLENGTHSW1 [10 ⁻²]	-	0.58	0.33
NOVELTY	1.00 ± 0.00	0.87 ± 0.33	1.00 ± 0.00
UNIQUENESS2D	0.92 ± 0.10	0.70 ± 0.33	0.71 ± 0.29
UNIQUENESS3D	-	0.31 ± 0.20	0.35 ± 0.15
DIVERSITY2D	0.92 ± 0.04	0.78 ± 0.08	0.75 ± 0.10
DIVERSITY3D	-	0.07 ± 0.12	0.06 ± 0.06
SA	0.66 ± 0.12	0.65 ± 0.13	0.66 ± 0.13
QED	0.49 ± 0.22	0.49 ± 0.22	0.48 ± 0.21
RINGS	2.98 ± 1.42	2.93 ± 1.36	2.93 ± 1.37
AROMATIC RINGS	1.84 ± 1.31	1.60 ± 1.20	1.82 ± 1.30
HACCEPTORS	7.30 ± 4.49	7.54 ± 4.40	7.43 ± 4.49
HDONORS	2.62 ± 1.68	2.80 ± 1.67	2.69 ± 1.81
LOGP	0.29 ± 3.48	0.07 ± 3.46	0.30 ± 3.59
MOLWT	390.43 ± 119.82	382.87 ± 117.73	388.79 ± 120.44
LIPINSKI	4.00 ± 1.34	4.20 ± 1.18	4.20 ± 1.17

Table 8: **Benchmark of the (non-pretrained) FLOWR.ROOT^{base} model for functional group inpainting against FLOWR.MULTI on the SPINDR test set.** Given a scaffold as context, the model generates the remaining functional groups. We report RDKit- and PoseBusters-validity of generated ligands, the GenBench3D strain energy and the AutoDock-Vina score. We also state the Wasserstein distance of generated ligands for the bond angles and bond lengths distribution to the SPINDR test set. Novelty, uniqueness and diversity measure the capability of the model to explore the chemical space both in 2D and 3D with the latter evaluating uniqueness and diversity of conformers of the same molecule (Note: if the list of generated ligands for a target contains duplicated molecules, otherwise they become zero). RDKit’s QED evaluation, SAScore, the molecular weight as well as the logP values evaluate drug-likeness of generated ligands. All presented values are mean values taken for 100 sampled ligands per test set target. The test dataset comprises 225 test set targets. Note, both RDKit- and PoseBusters-validity are evaluated on the raw generated set of 100 ligands per target. All other metrics are calculated on the subset of RDKit-valid ligands.

METRIC	TEST SET	FLOWR.MULTI ^{func.-group.-inpaint}	FLOWR.ROOT ^{BASE} _{func.-group.-inpaint}
RDKit-VALIDITY	1.00 ± 0.00	0.93 ± 0.25	0.98 ± 0.15
PB-VALIDITY	0.99 ± 0.02	0.88 ± 0.13	0.98 ± 0.10
STRAIN ENERGY	43.27 ± 41.85	86.26 ± 78.31	52.52 ± 36.64
VINA SCORE	-7.69 ± 2.00	-7.41 ± 0.67	-7.35 ± 0.58
VINA SCORE (MINIMIZED)	-7.88 ± 2.00	-7.72 ± 0.59	-7.62 ± 0.59
BONDANGLESW1	-	0.84	0.58
BONDLENGTHSW1 [10 ⁻²]	-	0.52	0.27
NOVELTY	1.00 ± 0.00	0.94 ± 0.23	1.00 ± 0.00
UNIQUENESS2D	0.92 ± 0.10	0.74 ± 0.28	0.75 ± 0.24
UNIQUENESS3D	-	0.35 ± 0.12	0.37 ± 0.15
DIVERSITY2D	0.92 ± 0.04	0.77 ± 0.07	0.75 ± 0.09
DIVERSITY3D	-	0.02 ± 0.01	0.06 ± 0.07
SA	0.66 ± 0.12	0.67 ± 0.13	0.66 ± 0.13
QED	0.49 ± 0.22	0.51 ± 0.21	0.51 ± 0.21
RINGS	2.98 ± 1.42	3.29 ± 1.46	3.27 ± 1.50
AROMATIC RINGS	1.84 ± 1.31	1.91 ± 1.33	1.84 ± 1.30
HACCEPTORS	7.30 ± 4.49	6.90 ± 4.21	7.00 ± 4.38
HDONORS	2.62 ± 1.68	2.61 ± 1.62	2.53 ± 1.73
LOGP	0.29 ± 3.48	0.83 ± 3.33	0.69 ± 3.29
MOLWT	390.43 ± 119.82	380.10 ± 115.69	381.96 ± 118.04
LIPINSKI	4.00 ± 1.34	4.40 ± 1.02	4.34 ± 1.07

B.3 Domain Adaptation via Finetuning: Project-1

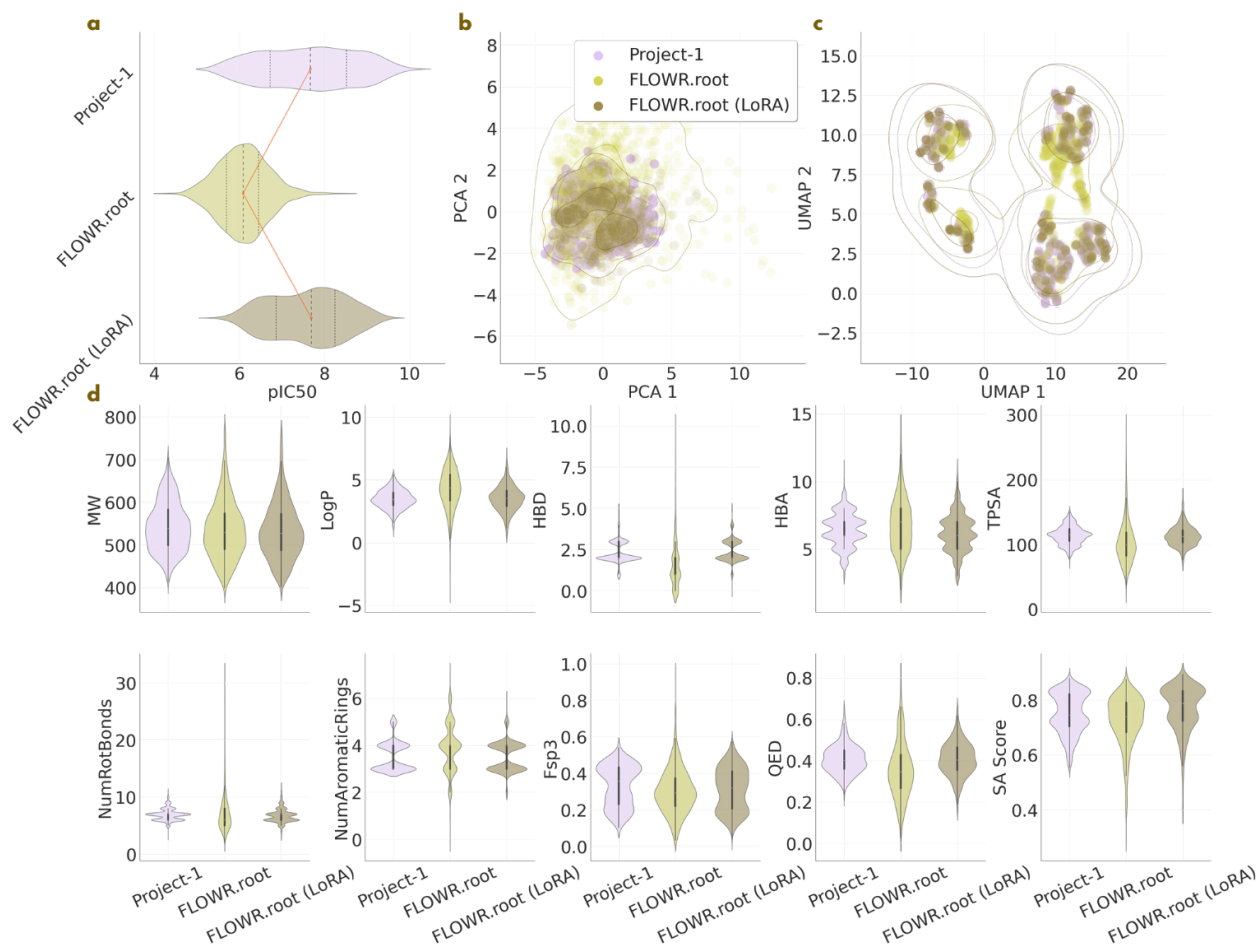


Figure 15: **Evaluation of FLOWR.ROOT-generated samples on the in-house Project-1 test dataset.** **a** Comparing the distribution of pIC_{50} values of generated ligands across test set complexes between FLOWR.ROOT and LoRA-finetuned FLOWR.ROOT. The pIC_{50} values for the test set are experimental, and otherwise predicted. **b** Depiction of chemical space comparison via PCA analysis showing the first two principal components. **c** Depiction of chemical space comparison via 2D UMAP analysis. **d** Distribution comparison regarding different chemical properties, namely molecular weight (MW), logP, number of hydrogen donors (HBD) and acceptors (HBA), topological surface area (TPSA), number of rotatable bonds (NumRotBonds) and aromatic rings (NumAromaticRings), fraction of sp^3 carbons (Fsp3), druglikeness (QED) and synthesizability (SA Score).

In Fig. 15, we visualize the structure–activity landscape of the test data from one of our in-house project datasets, comparing it to the distribution of ligands generated by both FLOWR.ROOT and its LoRA-finetuned variant. Following finetuning, we observe substantial adaptation to the SAR characteristics of the in-house distribution across predicted potency as well as a broad range of chemical properties, including the number of hydrogen bond donors and acceptors, rotatable bonds, and TPSA. These results underscore the effectiveness of the proposed domain adaptation approach. As expected, FLOWR.ROOT performs significantly worse when comparing chemical feature distributions; however, structural fidelity remains high. The mean PoseBusters validity is 0.90 ± 0.28 , and the mean strain energy is 48.04 ± 19.19 (compared to a mean reference strain energy 45.16 ± 11.43). Thus, in contrast to the zero-shot affinity prediction capabilities of FLOWR.ROOT, zero-shot structure prediction yields physically realistic structures.

B.4 Domain Adaptation via Finetuning: PDE10A

In Fig. 16, we visualize FLOWR.ROOT-generated ligands using fragment replacement and growing, allowing the model to extend the quinoline ring of compound 5SF4_46 from the PDE10A dataset within the 5SF4 protein pocket. The generated ligands effectively explore hydrogen bonding opportunities with the hydroxyl group of Y693 while

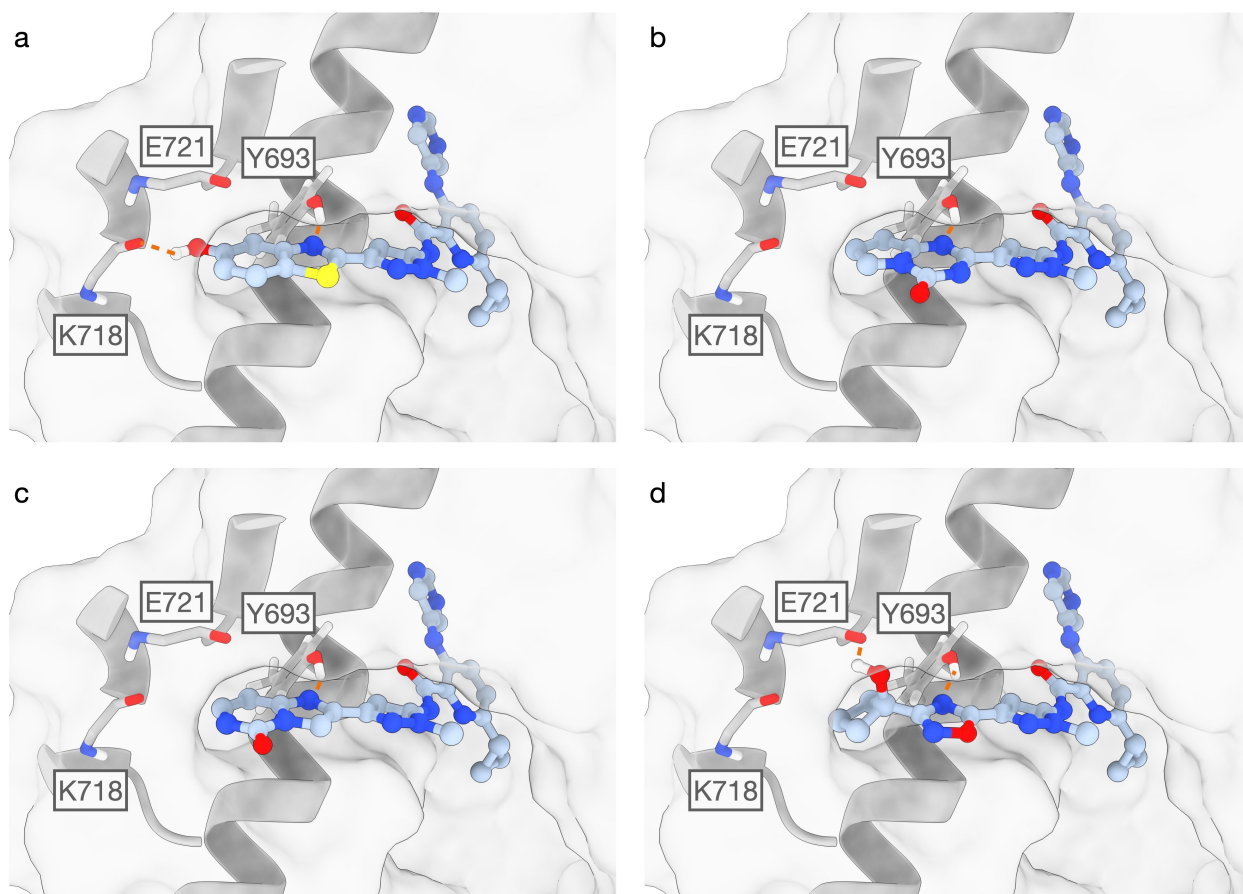


Figure 16: **Visualization of FLOWR.ROOT-predicted ligands running fragment replacement on PDE10A (PDB ID: 5SF4).** Several ligand chemotypes with different interaction patterns around the protein pocket. **a** capturing K718's main chain with a hydrogen bond. **b** and **c** similar chemotypes capable of avoiding interactions with the residues E721 and K718. **d** A ligand capable of capturing E721 with a hydrogen bond.

extending in alternative directions, such as towards residues E721 and K718. In most cases, the generated ligands tend to avoid interactions with these residues. However, in two instances (Fig. 16a and 16d), the ligand developed functional groups capable of forming hydrogen bonds with the main chain atoms of E721 and K718. The generated structures maintain high physical plausibility, with a mean PoseBusters-validity of 0.89 ± 0.31 and a mean strain energy of 93.92 ± 15.48 kcal/mol (compared to a reference ligand strain energy of 83.50 kcal/mol).

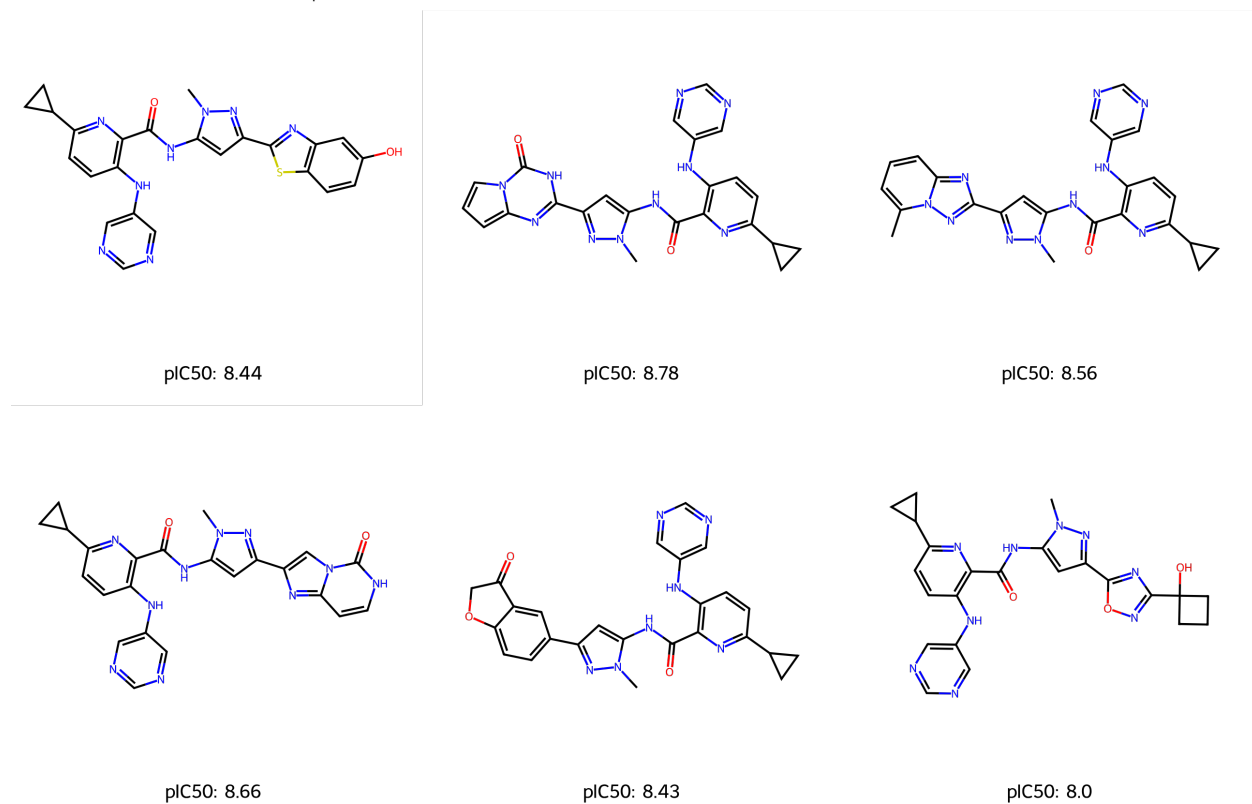
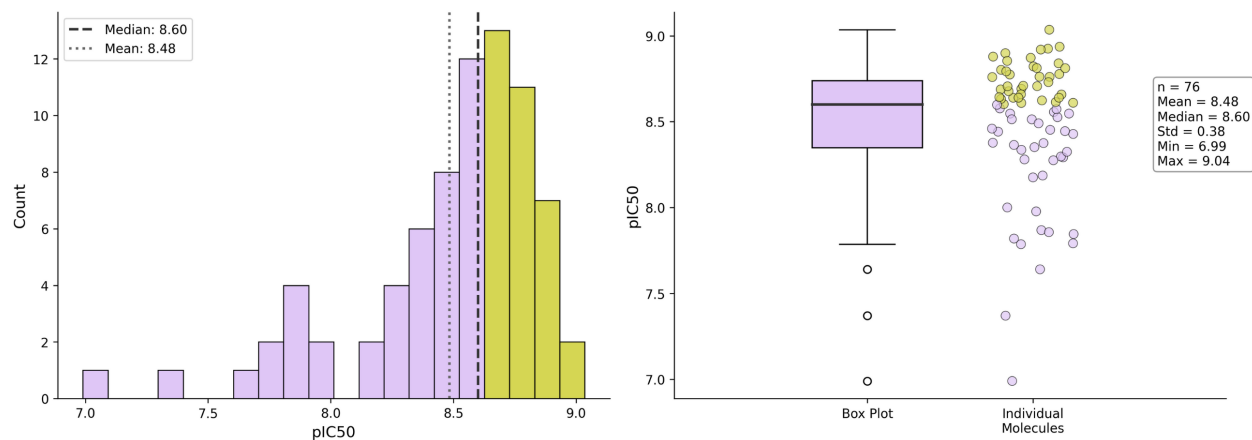


Figure 17: **Analysis of FLOWR.ROOT-predicted ligands after running fragment replacement on PDE10A (PDB ID: 5SF4).** Distribution over predicted pIC_{50} values of generated ligands within the 5SF4 protein pocket and a selection over promising candidates after interaction-analysis.

B.5 Case studies

Hsp90: Heat shock protein 90 We also performed QM validation of FLOWR.ROOT’s affinity head prediction on the heat shock protein 90 (Hsp90), Figure 18. Unlike the cases in the main text, the dynamic range of predicted affinities is significantly smaller, a consequence of the narrower pocket filled with water molecules. We performed two sets of benchmarks, on different sets: test1 includes more ligands with higher variation in functional groups (Figure 18, top block); test2 includes explicit water in the QM calculations (Figure 18, bottom block). In all cases, critical interactions, like the hydrogen bond to Asp93, are retained over the ligand space. In test1, FLOWR.ROOT tried to explore interactions in a lipophilic subpocket of Hsp90 by replacing a terminal phenyl ring with a pyridyl, to realize the latter is less likely to be stabilized in the lipophilic environment. The model also replaced the pyrimidine ring with a quinazoline, in order to reduce the ligand’s degrees of freedom, leading to less penalizing changes in entropy upon binding. This is seen when comparing the worst and best binders of the series. Finally, FLOWR.ROOT also tried to explore substitutions on the pyrimidine/quinazoline rings to further grow the ligand. As this is a solvent-exposed domain, NH_2 groups are favored and lead to better interaction patterns. In the case of test2, we explicitly included water molecules in the QM calculations, on top of implicit aqueous environment. This resulted in significantly better correlation between FLOWR.ROOT and the QM binding energies, although some of the poorer ligands had poorer QM scores due to soft clashes with the water molecules. This indicates that, although FLOWR.ROOT implicitly learns the composition and orientations of solvation layers, future work might involve giving the model the ability to capture these dynamically.

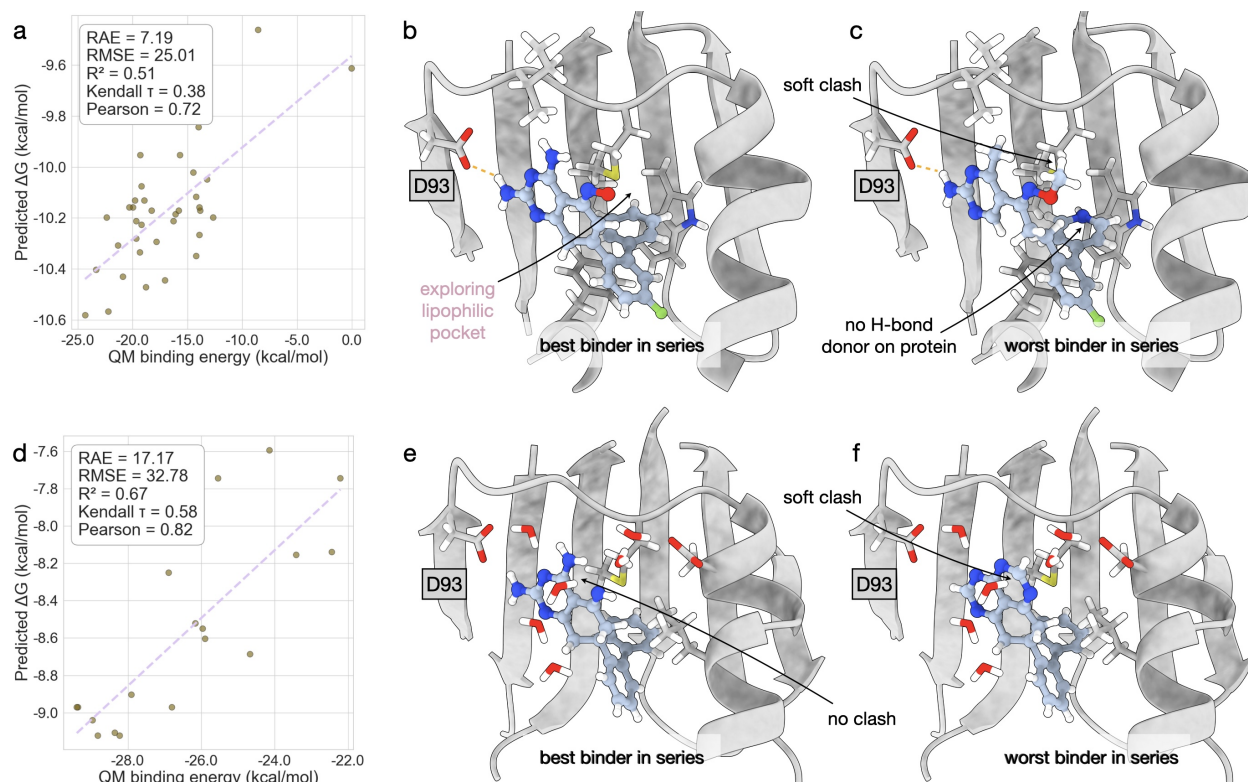


Figure 18: **FLOWR.ROOT quantum mechanical validation on Hsp90.** **a** Test-1 validation, with more ligands but without explicit waters. **b** Correlation between FLOWR.ROOT affinity metrics and QM binding energies. **c** Schematic representation of the best binder in the series. **d** Schematic representation of the worst binder in the series. **e** Test-2 validation, with explicit waters considered in the QM calculations. **f** Correlation between FLOWR.ROOT affinity metrics and QM binding energies. **g** Schematic representation of the best binder in the series. **h** Schematic representation of the worst binder in the series.

C Related Works

Diffusion- and flow-based generative models have emerged as leading frameworks in machine learning [Ho et al., 2020b, Song et al., 2021, Rombach et al., 2022]. Denoising Diffusion Probabilistic Models (DDPMs) learn a reverse process to transform noise into data samples [Ho et al., 2020b], while score-based models formulate generation via

reverse-time stochastic differential equations (SDEs) or their probability-flow ordinary differential equation (ODE) counterparts [Song et al., 2021]. Flow matching, in turn, directly regresses the velocity field along a prescribed probability path to train continuous normalizing flows [Lipman et al., 2023, Liu et al., 2022], with stochastic-interpolant theory offering a unified perspective on diffusion and flow models [Albergo and Vanden-Eijnden, 2023, Albergo et al., 2023]. Beyond applications in natural language processing and computer vision, these models are increasingly applied to biology and chemistry, fueling advances in generative chemistry for drug discovery [Hoogeboom et al., 2022, Vignac et al., 2023, Le et al., 2023, Schneuing et al., 2023, Guan et al., 2023, Cremer et al., 2024, Campbell et al., 2024, Irwin et al., 2024, Cremer et al., 2025]. In drug discovery, designing small molecules that selectively bind to specific protein targets remains a critical challenge. Diffusion and flow models have proven effective at capturing complex molecular and structural distributions, advancing methods from 3D molecular generation in structure-based drug design (SBDD) to protein–ligand (co-)folding [Abramson et al., 2024, Passaro et al., 2025].

One important subfield of AI-driven SBDD is pocket-conditional, structure-aware ligand design. Models like DiffSBDD [Schneuing et al., 2023] and TargetDiff [Guan et al., 2023] have demonstrated that $SE(3)$ -equivariant diffusion models can generate ligands directly within protein pockets. Follow-up studies have focused on improving chemical validity and pose accuracy [Le et al., 2023, Wang et al., 2024] while coupling pocket conditioning with large-scale pre-training and multi-objective importance sampling to guide generation toward potency and synthesizability [Cremer et al., 2024]. Additionally, AI-driven models have increasingly integrated fragment priors into generative pipelines [Imrie et al., 2020, Voloboev, 2024, Zhang et al., 2024, Lee et al., 2025, Guo et al., 2023, Igashov et al., 2024]. In fragment-based drug discovery (FBDD), which focuses on hit-to-lead optimization, models typically specialize either in *de novo* design or fragment-based strategies. However, practical lead optimization requires flexible navigation between these regimes, such as fragment growing or scaffold hopping under interaction constraints, which most current frameworks do not adequately address. Furthermore, many models do not incorporate the geometric constraints imposed by protein pockets. Recent work proposes a unified flow matching approach that integrates *de novo*, interaction-constrained, and fragment-based generation under pocket conditioning with efficient ODE sampling [Cremer et al., 2025].

However, the effectiveness of generated ligands ultimately depends on their potency and binding affinity, which requires reliable affinity prediction. While experimental validation remains indispensable, computational prioritization during the design phase relies on accurate affinity predictions to effectively navigate target-relevant regions of chemical space. Classical scoring functions, such as AutoDock Vina [Trott and Olson, 2010], Glide [Friesner et al., 2004], and GOLD [Jones et al., 1997], offer computational efficiency but often lack the necessary accuracy for reliable prioritization. Physics-based methods like free energy perturbation (FEP) and absolute binding free energy (ABFE) calculations provide higher precision [Wang et al., 2015, Mey et al., 2020, Mobley and Klimovich, 2012, Alibay et al., 2022, Feng et al., 2022a, Ries et al., 2024], yet their computational cost prohibits application to large-scale generative campaigns, restricting their use to small subsets of candidates where absolute affinity data is critical. Machine learning–based scoring functions improve throughput but suffer from dataset bias and limited generalization [Jiménez et al., 2018]. Recent approaches using data augmentation have shown modest improvements [Valsson et al., 2025], though they lack explicit structural information and remain insufficient for robust affinity prediction. The Boltz-2 ligand–protein co-folding model achieves near-FEP accuracy on selected targets with substantial speed advantages [Passaro et al., 2025]. However, its decoupled architecture—where the affinity head is trained independently from the structural module—creates dependence on structure prediction quality, requires co-folding prior to each affinity prediction, and may limit co-adaptation between protein pocket and ligand geometry, particularly during project-specific finetuning.

These limitations motivate a framework that jointly learns structure and affinity while supporting fast, controllable, structure-aware generation. A model that learns the joint probability distribution over ligand geometry, binding pose, and affinity within the protein pocket context would enable efficient, potency-guided ligand generation with on-the-fly ranking capabilities. Crucially, joint training facilitates simple project-specific adaptation through finetuning—an essential capability given the distinct constraints of drug discovery campaigns, ranging from ADME/T requirements to R-group and scaffold novelty constraints, diverse assay readouts, and medicinal chemistry heuristics. A fundamental challenge in structure-based generative modeling lies in the inherent disconnect between public-domain training data and project-specific structure-activity relationships (SARs). While models can achieve broad coverage of chemical space through ligand generation, generalizing across novel bioactivity landscapes represents a fundamentally more complex problem. We posit that expecting universal generalization without adaptation is unrealistic; instead, models should function as dynamic companions that continuously refine their understanding of project-specific SARs through sustained interaction with incoming data. This paradigm shift necessitates moving from static models to efficient iterative refinement processes where model utility grows through continuous adaptation. Additionally, techniques such as multi-objective guidance via inference-time importance sampling [Cremer et al., 2024] can help steering generation toward pre-specified, desired properties, while deeper distribution mismatches or activity cliffs can be addressed through direct preference alignment [Schneuing et al., 2025] when suitable data is available.

While large ligand-only resources such as ZINC and PubChem offer abundant chemical diversity [Irwin et al., 2020, Bolton et al., 2011], high-quality protein–ligand complexes with reliable affinity annotations remain scarce and noisy. Databases like PDBbind provide valuable training data [Wang et al., 2005], yet suffer from quality and coverage limitations; curated subsets such as HiQBind address these issues and even increase sample sizes [Wang et al., 2025], yet remain limited in scale. The Plinder dataset [Durairaj et al., 2024] expands scale by broadly curating the PDB, but most entries lack affinity annotations. More recent resources—BindingNet [Zhu et al., 2025], Kinodata-3D [Backenköhler et al., 2024], and especially SAIR [Lemos et al., 2025]—improve chemical space coverage and include affinity data, though they do so with reduced accuracy. This heterogeneous data landscape, however, motivates a multi-stage training paradigm: by systematically combining available resources ranked by fidelity, we can exploit their complementary strengths. Large-scale, lower-fidelity data establishes broad chemical space coverage and foundational structural understanding, while subsequent refinement on higher-quality, curated datasets sharpens affinity prediction and structural accuracy. Critically, this approach yields foundation models capable of efficient adaptation to project-specific objectives.

In the following, we discuss related works in more details for 3D molecular generation, pocket-aware ligand design, fragment-based drug discovery, and binding affinity prediction methods.

Molecule generation Early neural approaches to 3D molecular generation explored autoregressive models that sequentially add coordinates and atom types while maintaining geometric consistency. Symmetry-aware models such as G-SchNet [Gebauer et al., 2020] and its conditional inverse-design follow-up [Gebauer et al., 2022] demonstrated that enforcing $E(3)$ symmetries and conditioning signals can substantially improve the validity and controllability of generated 3D structures. Subsequent work proposed explicit autoregressive flows [Luo and Ji, 2022]. In parallel, the diffusion modeling paradigm matured from its non-equilibrium thermodynamics roots [Sohl-Dickstein et al., 2015] through score-based [Song et al., 2021] and variational formulations [Ho et al., 2020a, Kingma et al., 2021]. These ideas rapidly translated to molecular geometry: Xu et al. [2022] and Jing et al. [2023] showed that $E(3)$ -equivariant denoisers enable high-quality conformation generation by diffusing in Cartesian and torsional spaces, respectively.

The first $E(3)$ -equivariant diffusion model for joint continuous coordinate and atom type generation was EDM [Hoogenboom et al., 2022]. Follow-ons pushed the design space along several axes: discrete and continuous combination with explicit bond order learning [Vignac et al., 2023], and enhanced denoising learning objectives [Le et al., 2023], establishing strong baselines.

Thereafter, diffusion-based methods pioneered pocket-aware *de novo* design, also utilizing $E(3)$ -equivariant networks. Notably, DiffSBDD [Schneuing et al., 2023] and TargetDiff [Guan et al., 2023] demonstrated that conditional diffusion models can generate diverse, target-specific ligands within the protein pocket, adhering to symmetry constraints and enabling task versatility through sampling controls. More recently, PILOT [Cremer et al., 2024] combined large-scale pre-training, pocket conditioning, and property guidance, highlighting the importance of multi-objective steering (e.g., drug-likeness, synthesizability) under structure constraints. Together, these works established that pocket-aware 3D diffusion can simultaneously respect symmetry, improve pose realism, and support versatile constraints via conditioning and guided sampling.

Meanwhile, flow matching [Lipman et al., 2023] (FM) was proposed refining continuous normalizing flows by directly regressing a time-dependent velocity field that pushes a simple prior to the data distribution, offering faster sampling and flexible priors. SEMLAFLOW [Irwin et al., 2024] introduced a scalable $SE(3)$ -equivariant architecture (Semla) trained via flow matching, achieving state-of-the-art unconditional 3D molecule generation with significant speed-ups. Pushing FM into SBDD, FLOWR [Cremer et al., 2025] extended the Semla-style backbones with a dedicated pocket encoder and mixed continuous/categorical FM, supporting multi-mode *de novo*, interaction-guided, and fragment-based generation in a single model. FLOWR reports large speedups over pocket-diffusion baselines.

Fragment-based drug discovery Fragment-based drug discovery (FBDD) motivates models that initiate from fragments and perform growth, linking, or merging under pocket constraints. Early deep generative linker design incorporated 3D information into graph models (DeLinker) Imrie et al. [2020], while SyntaLinker and AutoLinker utilized conditional transformers to synthesize linkers directly in the SMILES space, given fragment pairs and constraints Yang et al. [2020b], Feng et al. [2022b]. Recent advances have introduced $E(3)$ -equivariant models: DiffLinker formulates linker generation as an $E(3)$ -equivariant conditional diffusion, explicitly learning 3D geometry between fragment anchors Igashov et al. [2024]. For broader medicinal-chemistry workflows, Link-INVENT extends REINVENT with reinforcement learning to optimize linkers for multiple objectives, demonstrated on fragment linking, scaffold hopping, and PROTAC design Guo et al. [2023]. STRIFE extracts target-specific pharmacophoric features to steer elaboration in 3D Hadfield et al. [2022], while AutoFragDiff integrates fragment-wise, autoregressive diffusion with pocket conditioning to improve local 3D geometry during growth Ghorbani et al. [2023]. For scaffold hopping, DiffHopp employs an $E(3)$ -equivariant graph diffusion model tailored for scaffold replacement conditioned on a protein–ligand complex

Torge et al. [2023], and TurboHopp accelerates pocket-conditioned 3D scaffold hopping with consistency models and reinforcement learning-based preference optimization Yoo et al. [2024].

Binding Affinity Prediction Estimating the change in free energy upon binding (ΔG_{bind} , or affinity) accurately remains a cornerstone of structure-enabled small-molecule discovery. Binding affinity is relevant for all early stages of drug discovery, starting from hit identification, where the goal is to find tight and selective binders, through hit-to-lead and lead optimization, where potency must be balanced with absorption, distribution, metabolism, excretion, safety, toxicity, and efficacy considerations. Given the astronomical size of chemical space, computer-aided drug design (CADD) is indispensable to select and prioritize candidates *in silico* before spending scarce experimental resources [Reymond et al., 2010, Jorgensen, 2004].

Classical structure-based approaches to affinity prediction span knowledge-based scoring and physics-based models grounded in molecular mechanics [Liu and Wang, 2015, Gilson and Zhou, 2007]. Heuristic docking scores offer speed at the expense of physical rigor. Empirical scoring functions such as AutoDock Vina, Glide, or GOLD remain widely used due to speed, but show inconsistent results between targets Trott and Olson [2010], Friesner et al. [2004], Jones et al. [1997]. Semi-empirical and QM / MM scoring have closed part of the gap at an intermediate cost, for example, SQM2.20 achieves DFT-quality affinity estimates in minutes, but only on selected targets [Pecina et al., 2024, Molani and Cho, 2024].

End-point methods such as MM-PBSA and MM-GBSA combine molecular mechanics with continuum solvation to approximate the ΔG_{bind} from MD snapshots at a relatively low cost and remain widely used when throughput is critical [Kollman et al., 2000, Homeyer and Gohlke, 2012, Still et al., 1990, Gohlke and Case, 2004]. Alchemical binding free energy methods, absolute (ABFE) and relative (RBFE), trade throughput for accuracy [Aldeghi et al., 2016, Boresch et al., 2003, Gilson et al., 1997, Fu et al., 2022, Feng et al., 2022a, Cournia et al., 2017, Ross et al., 2023a]. Modern workflows based on the free energy perturbation theory (FEP) [Zwanzig, 1954] have achieved impressive accuracy on suitable congeneric series [Abel et al., 2017, Wang et al., 2015, Ross et al., 2023b], but remain sensitive to force fields and system preparation.

Machine learning (ML) offers a complementary path to rapid affinity estimation by learning structure–activity relationships directly from data. The early ML scoring functions used interaction fingerprints and hand-made descriptors [Ballester and Mitchell, 2010, Wójcikowski et al., 2019, Kundu et al., 2018, Boyles et al., 2020]. Sequence-based CPI / DTA models (e.g., DeepDTA) encode proteins and ligands from 1D inputs to predict binding affinity [Öztürk et al., 2018], while more recent deep architectures, such as 3D convolutional neural networks and graph neural networks, operate more holistically on complex geometry and interaction graphs [Jiménez et al., 2018, Jiang et al., 2021, Karlov et al., 2020, Nguyen et al., 2021, Li et al., 2021, Meli et al., 2022, Valsson et al., 2025].

ML models are typically trained and evaluated on community benchmarks (e.g., CASF) [Li et al., 2018, Su et al., 2019]. However, strong in-benchmark performance does not guarantee generalization. Multiple analyses show that models can overfit ligand biases, struggle on out-of-distribution (OOD) targets, or even partially fit to noise [Volkov et al., 2022, Scantlebury et al., 2023, Yang et al., 2020a, Crusius et al., 2025]. This limits their reliability in prospective campaigns and underscores the need for approaches that encode biophysical constraints, reduce dataset shortcuts, and validate on OOD benchmarks.

Compounding these challenges is data scarcity: structure-based learning ideally requires reliable affinity measurements paired with high-resolution 3D protein–ligand complexes. Although data augmentation is a mainstay in computer vision and NLP [Paulin and Ivašić-Kos, 2023, Pellicer et al., 2023], generating meaningful molecular data that respect stereochemistry, conformational physics, and pocket geometry remains non-trivial. However, combining ChEMBL and PDBbind through comparative complex structure and enhanced template-based modeling resulted in the BindingNet resource, comprising *ca.* 690k complexes. This significantly densifies the bioactivity landscape compared to the PDBbind alone [Li et al., 2024, Zhu et al., 2025].

A recent advancement is Boltz-2, a co-folding foundation model that predicts complex structures and based on that binding affinity, approaching FEP-level accuracy on certain targets while running orders of magnitude faster, makes large-scale affinity ranking feasible [Passaro et al., 2025]. Boltz-2’s affinity module couples structural inference with potency prediction, providing a stronger supervisory signal than *post hoc* scoring and highlighting the value of unified structure–affinity modeling in end-to-end pipelines [Passaro et al., 2025].

References

Robert Abel, Lingle Wang, Edward D. Harder, B. J. Berne, and Richard A. Friesner. Advancing drug discovery through enhanced free energy calculations. *Accounts of Chemical Research*, 50(7):1625–1632, 2017. doi: 10.1021/acs.accounts.7b00083.

- Josh Abramson, Jonas Adler, Jack Dunger, Richard Evans, Tim Green, Alexander Pritzel, Olaf Ronneberger, Lindsay Willmore, Andrew J. Ballard, Joshua Bambrick, Sebastian W. Bodenstein, David A. Evans, Chia-Chun Hung, Michael O'Neill, David Reiman, Kathryn Tunyasuvunakool, Zachary Wu, Akvilė Žemgulytė, Eirini Arvaniti, Charles Beattie, Ottavia Bertolli, Alex Bridgland, Alexey Cherepanov, Miles Congreve, Alexander I. Cowen-Rivers, Andrew Cowie, Michael Figurnov, Fabian B. Fuchs, Hannah Gladman, Rishub Jain, Yousuf A. Khan, Caroline M. R. Low, Kuba Perlin, Anna Potapenko, Pascal Savy, Sukhdeep Singh, Adrian Stecula, Ashok Thillaisundaram, Catherine Tong, Sergei Yakneen, Ellen D. Zhong, Michal Zielinski, Augustin Židek, Victor Bapst, Pushmeet Kohli, Max Jaderberg, Demis Hassabis, and John M. Jumper. Accurate structure prediction of biomolecular interactions with alphafold 3. *Nature*, 630(8016):493–500, Jun 2024. ISSN 1476-4687. doi: 10.1038/s41586-024-07487-w. URL <https://doi.org/10.1038/s41586-024-07487-w>.
- Michael S. Albergo and Eric Vanden-Eijnden. Building normalizing flows with stochastic interpolants. *ICLR*, 2023. arXiv:2209.15571.
- Michael S Albergo, Nicholas M Boffi, and Eric Vanden-Eijnden. Stochastic interpolants: A unifying framework for flows and diffusions. *arXiv preprint*, 2023. arXiv:2303.08797.
- Matteo Aldeghi, Alexander Heifetz, Michael J. Bodkin, Stefan Knapp, and Philip C. Biggin. Accurate calculation of the absolute free energy of binding for drug molecules. *Chem. Sci.*, 7:207–218, 2016. doi: 10.1039/C5SC02678D. URL <http://dx.doi.org/10.1039/C5SC02678D>.
- Irfan Alibay, Aniket Magarkar, Daniel Seeliger, and Philip Charles Biggin. Evaluating the use of absolute binding free energy in the fragment optimisation process. *Communications Chemistry*, 5(1):105, Sep 2022. ISSN 2399-3669. doi: 10.1038/s42004-022-00721-4. URL <https://doi.org/10.1038/s42004-022-00721-4>.
- Michael Backenköhler, Joschka Groß, Verena Wolf, and Andrea Volkamer. Guided docking as a data generation approach facilitates structure-based machine learning on kinases. *Journal of Chemical Information and Modeling*, 64(10):4009–4020, May 2024. ISSN 1549-9596. doi: 10.1021/acs.jcim.4c00055. URL <https://doi.org/10.1021/acs.jcim.4c00055>.
- Pedro J. Ballester and John B. O. Mitchell. A machine learning approach to predicting protein–ligand binding affinity with applications to molecular docking. *Bioinformatics*, 26(9):1169–1175, 2010. doi: 10.1093/bioinformatics/btq112.
- Christoph Bannwarth, Sebastian Ehlert, and Stefan Grimme. Gfn2-xtb—an accurate and broadly parametrized self-consistent tight-binding quantum chemical method with multipole electrostatics and density-dependent dispersion contributions. *Journal of Chemical Theory and Computation*, 15(3):1652–1671, Mar 2019. ISSN 1549-9618. doi: 10.1021/acs.jctc.8b01176. URL <https://doi.org/10.1021/acs.jctc.8b01176>.
- Roberto Battistutta, Giorgio Cozza, Fabrice Pierre, Elena Papinutto, Graziano Lolli, Stefania Sarno, Sean E O'Brien, Adam Siddiqui-Jain, Mustapha Haddach, Kenna Anderes, David M Ryckman, Flavio Meggio, and Lorenzo A Pinna. Unprecedented selectivity and structural determinants of a new class of protein kinase CK2 inhibitors in clinical trials for the treatment of cancer. *Biochemistry*, 50(39):8478–8488, September 2011.
- Evan E. Bolton, Jie Chen, Sunghwan Kim, Lianyi Han, Siqian He, Wenyao Shi, Vahan Simonyan, Yan Sun, Paul A. Thiessen, Jiyao Wang, Bo Yu, Jian Zhang, and Stephen H. Bryant. Pubchem3d: a new resource for scientists. *Journal of Cheminformatics*, 3(1):32, Sep 2011. ISSN 1758-2946. doi: 10.1186/1758-2946-3-32. URL <https://doi.org/10.1186/1758-2946-3-32>.
- Stefan Boresch, Franz Tettinger, Martin Leitgeb, and Martin Karplus. Absolute binding free energies: A quantitative approach for their calculation. *The Journal of Physical Chemistry B*, 107(35):9535–9551, 2003. doi: 10.1021/jp0217839.
- Cédric Bouysset and Sébastien Fiorucci. Prolif: a library to encode molecular interactions as fingerprints. *Journal of Cheminformatics*, 13(1):72, Sep 2021. ISSN 1758-2946. doi: 10.1186/s13321-021-00548-6. URL <https://doi.org/10.1186/s13321-021-00548-6>.
- Fergus Boyles, Charlotte M. Deane, and Garrett M. Morris. Learning from the ligand: using ligand-based features to improve binding affinity prediction. *Bioinformatics*, 36(3):758–764, 2020. doi: 10.1093/bioinformatics/btz665.
- Martin Buttenschoen, Garrett M. Morris, and Charlotte M. Deane. Posebusters: Ai-based docking methods fail to generate physically valid poses or generalise to novel sequences, 2024. URL <http://dx.doi.org/10.1039/D3SC04185A>.
- Andrew Campbell, Jason Yim, Regina Barzilay, Tom Rainforth, and Tommi Jaakkola. Generative flows on discrete state-spaces: Enabling multimodal flows with applications to protein co-design, 2024. URL <https://arxiv.org/abs/2402.04997>.

- Zoe Cournia, Bryce Allen, and Woody Sherman. Relative binding free energy calculations in drug discovery: Recent advances and practical considerations. *Journal of Chemical Information and Modeling*, 57(12):2911–2937, 2017. doi: 10.1021/acs.jcim.7b00564.
- Julian Cremer, Tuan Le, Frank Noé, Djork-Arné Clevert, and Kristof T. Schütt. Pilot: equivariant diffusion for pocket-conditioned de novo ligand generation with multi-objective guidance via importance sampling. *Chem. Sci.*, 15:14954–14967, 2024. doi: 10.1039/D4SC03523B. URL <http://dx.doi.org/10.1039/D4SC03523B>.
- Julian Cremer, Ross Irwin, Alessandro Tibot, Jon Paul Janet, Simon Olsson, and Djork-Arné Clevert. Flowr: Flow matching for structure-aware de novo, interaction- and fragment-based ligand generation. *arXiv preprint*, 2025.
- Daniel Crusius, Flaviu Cipcigan, and Philip C. Biggin. Are we fitting data or noise? analysing the predictive power of commonly used datasets in drug-, materials-, and molecular-discovery. *Faraday Discussions*, 256:304–321, 2025. doi: 10.1039/D4FD00091A.
- Mindy I. Davis, Jeremy P. Hunt, Sanna Herrgard, Pietro Ciceri, Lisa M. Wodicka, Gabriel Pallares, Michael Hocker, Daniel K. Treiber, and Patrick P. Zarrinkar. Comprehensive analysis of kinase inhibitor selectivity. *Nature Biotechnology*, 29(11):1046–1051, Nov 2011. ISSN 1546-1696. doi: 10.1038/nbt.1990. URL <https://doi.org/10.1038/nbt.1990>.
- Pierre Del Moral, Arnaud Doucet, and Ajay Jasra. Sequential monte carlo samplers. *Journal of the Royal Statistical Society Series B: Statistical Methodology*, 68(3):411–436, 05 2006. ISSN 1369-7412. doi: 10.1111/j.1467-9868.2006.00553.x. URL <https://doi.org/10.1111/j.1467-9868.2006.00553.x>.
- Ian Dunn and David R. Koes. Flowmol3: Flow matching for 3d de novo small-molecule generation, 2025. URL <https://arxiv.org/abs/2508.12629>.
- Janani Durairaj, Yusuf Adeshina, Zhonglin Cao, Xuejin Zhang, Vladas Oleinikovas, Thomas Duignan, Zachary McClure, Xavier Robin, Danny Kovtun, Emanuele Rossi, Guoqing Zhou, Srimukh Veccham, Clemens Isert, Yuxing Peng, Prabindh Sundareson, Mehmet Akdel, Gabriele Corso, Hannes Stärk, Zachary Carpenter, Michael Bronstein, Emine Kucukbenli, Torsten Schwede, and Luca Naef. Plinder: The protein-ligand interactions dataset and evaluation resource. *bioRxiv*, 2024. doi: 10.1101/2024.07.17.603955. URL <https://www.biorxiv.org/content/early/2024/07/17/2024.07.17.603955>.
- Jerome Eberhardt, Diogo Santos-Martins, Andreas F. Tillack, and Stefano Forli. Autodock vina 1.2.0: New docking methods, expanded force field, and python bindings. *Journal of Chemical Information and Modeling*, 61(8):3891–3898, Aug 2021. ISSN 1549-9596. doi: 10.1021/acs.jcim.1c00203. URL <https://doi.org/10.1021/acs.jcim.1c00203>.
- Sebastian Ehlert, Marcel Stahn, Sebastian Spicher, and Stefan Grimme. Robust and efficient implicit solvation model for fast semiempirical methods. *Journal of Chemical Theory and Computation*, 17(7):4250–4261, Jul 2021. ISSN 1549-9618. doi: 10.1021/acs.jctc.1c00471. URL <https://doi.org/10.1021/acs.jctc.1c00471>.
- Mudong Feng, Germano Heinzelmann, and Michael K. Gilson. Absolute binding free energy calculations improve enrichment of actives in virtual compound screening. *Scientific Reports*, 12(1):13640, Aug 2022a. ISSN 2045-2322. doi: 10.1038/s41598-022-17480-w. URL <https://doi.org/10.1038/s41598-022-17480-w>.
- Yu Feng, Yuyao Yang, Wenbin Deng, Hongming Chen, and Ting Ran. Syntalinker-hybrid: A deep learning approach for target specific drug design. *Artificial Intelligence in the Life Sciences*, 2:100035, 2022b. ISSN 2667-3185. doi: <https://doi.org/10.1016/j.ailesci.2022.100035>. URL <https://www.sciencedirect.com/science/article/pii/S266731852200006X>.
- Richard A. Friesner, Jay L. Banks, Robert B. Murphy, Thomas A. Halgren, Jasna J. Klicic, Daniel T. Mainz, Matthew P. Repasky, Eric H. Knoll, Mee Shelley, Jason K. Perry, David E. Shaw, Perry Francis, and Peter S. Shenkin. Glide: a new approach for rapid, accurate docking and scoring. 1. method and assessment of docking accuracy. *Journal of Medicinal Chemistry*, 47(7):1739–1749, Mar 2004. ISSN 0022-2623. doi: 10.1021/jm0306430. URL <https://doi.org/10.1021/jm0306430>.
- Haohao Fu, Haochuan Chen, Marharyta Blazhynska, Emma Goulard Coderc de Lacam, Florence Szczepaniak, Anna Pavlova, Xueguang Shao, James C. Gumbart, François Dehez, Benoît Roux, Wensheng Cai, and Christophe Chipot. Accurate determination of protein:ligand standard binding free energies from molecular dynamics simulations. *Nature Protocols*, 17(4):1114–1141, Apr 2022. ISSN 1750-2799. doi: 10.1038/s41596-021-00676-1. URL <https://doi.org/10.1038/s41596-021-00676-1>.
- Niklas W. A. Gebauer, Michael Gastegger, and Kristof T. Schütt. Symmetry-adapted generation of 3d point sets for the targeted discovery of molecules, 2020. URL <https://arxiv.org/abs/1906.00957>.
- Niklas W. A. Gebauer, Michael Gastegger, Stefaan S. P. Hessmann, Klaus-Robert Müller, and Kristof T. Schütt. Inverse design of 3d molecular structures with conditional generative neural networks. *Nature Communications*, 13(1):

- 973, Feb 2022. ISSN 2041-1723. doi: 10.1038/s41467-022-28526-y. URL <https://doi.org/10.1038/s41467-022-28526-y>.
- Mahdi Ghorbani, Leo Gendele, Paul Beroza, and Michael J. Keiser. Autoregressive fragment-based diffusion for pocket-aware ligand design. *arXiv preprint arXiv:2401.05370*, 2023.
- Michael K. Gilson and Huan-Xiang Zhou. Calculation of protein–ligand binding affinities. *Annual Review of Biophysics and Biomolecular Structure*, 36:21–42, 2007. doi: 10.1146/annurev.biophys.36.040306.132550.
- Michael K. Gilson, James A. Given, Bruce L. Bush, and J. Andrew McCammon. The statistical-thermodynamic basis for computation of binding affinities: A critical review. *Biophysical Journal*, 72(3):1047–1069, 1997. doi: 10.1016/S0006-3495(97)78866-9.
- Holger Gohlke and David A. Case. Converging free energy estimates: Mm-pb(gb)sa studies on the protein–protein complex ras–raf. *Journal of Computational Chemistry*, 25(2):238–250, 2004. doi: 10.1002/jcc.10379.
- Przemyslaw Grygier, Katarzyna Pustelny, Jakub Nowak, Przemyslaw Golik, Grzegorz M. Popowicz, Oliver Plettenburg, Grzegorz Dubin, Filipe Menezes, and Anna Czarna. Silitasertib (cx-4945), a clinically used ck2-kinase inhibitor with additional effects on gsk3b and dyrk1a kinases: A structural perspective. *Journal of Medicinal Chemistry*, 66(6):4009–4024, 2023. doi: 10.1021/acs.jmedchem.2c01887. URL <https://doi.org/10.1021/acs.jmedchem.2c01887>. PMID: 36883902.
- Przemyslaw Grygier, Katarzyna Pustelny, Filipe Menezes, Malgorzata Jemiola-Rzeminska, Piotr Suder, Grzegorz Dubin, and Anna Czarna. Structural perspective on the design of selective dyrk1b inhibitors. *International Journal of Biological Macromolecules*, 330:148124, 2025. ISSN 0141-8130. doi: <https://doi.org/10.1016/j.ijbiomac.2025.148124>. URL <https://www.sciencedirect.com/science/article/pii/S0141813025086817>.
- Jiaqi Guan, Wesley Wei Qian, Xingang Peng, Yufeng Su, Jian Peng, and Jianzhu Ma. 3d equivariant diffusion for target-aware molecule generation and affinity prediction. In *The Eleventh International Conference on Learning Representations*, 2023. URL <https://openreview.net/forum?id=kJqXEPXMsE0>.
- Jeff Guo, Franziska Knuth, Christian Margreitter, Jon Paul Janet, Kostas Papadopoulos, Ola Engkvist, and Atanas Patronov. Link-invent: generative linker design with reinforcement learning. *Digital Discovery*, 2:392–408, 2023. doi: 10.1039/D2DD00115B. URL <http://dx.doi.org/10.1039/D2DD00115B>.
- Izabella Góral, Tomasz Wichur, Emilia Sługocka, Przemysław Grygier, Monika Głuch-Lutwin, Barbara Mordyl, Ewelina Honkisz-Orzechowska, Natalia Szałaj, Justyna Godyń, Dawid Panek, Paula Zareba, Anna Sarka, Paweł Żmudzki, Gniewomir Latacz, Katarzyna Pustelny, Adam Bucki, Anna Czarna, Filipe Menezes, and Anna Więckowska. Exploring novel gsk-3 β inhibitors for anti-neuroinflammatory and neuroprotective effects: Synthesis, crystallography, computational analysis, and biological evaluation. *ACS Chemical Neuroscience*, 15(17):3181–3201, 2024. doi: 10.1021/acschemneuro.4c00365. URL <https://doi.org/10.1021/acschemneuro.4c00365>. PMID: 39158934.
- Thomas E. Hadfield, Fergus Imrie, Andy Merritt, Kristian Birchall, and Charlotte M. Deane. Incorporating target-specific pharmacophoric information into deep generative models for fragment elaboration. *Journal of Chemical Information and Modeling*, 62(10):2280–2292, May 2022. ISSN 1549-9596. doi: 10.1021/acs.jcim.1c01311. URL <https://doi.org/10.1021/acs.jcim.1c01311>.
- Jonathan Ho, Ajay Jain, and Pieter Abbeel. Denoising diffusion probabilistic models. *Advances in neural information processing systems*, 33:6840–6851, 2020a.
- Jonathan Ho, Ajay Jain, and Pieter Abbeel. Denoising diffusion probabilistic models. *NeurIPS*, 2020b. arXiv:2006.11239.
- Nadine Homeyer and Holger Gohlke. Free energy calculations by the molecular mechanics poisson–boltzmann surface area method. *Molecular Informatics*, 31(2):114–122, 2012. doi: 10.1002/minf.201100135.
- Emiel Hoogeboom, Víctor Garcia Satorras, Clément Vignac, and Max Welling. Equivariant diffusion for molecule generation in 3D. In Kamalika Chaudhuri, Stefanie Jegelka, Le Song, Csaba Szepesvari, Gang Niu, and Sivan Sabato, editors, *Proceedings of the 39th International Conference on Machine Learning*, volume 162 of *Proceedings of Machine Learning Research*, pages 8867–8887. PMLR, 17–23 Jul 2022. URL <https://proceedings.mlr.press/v162/hoogeboom22a.html>.
- Edward J Hu, yelong shen, Phillip Wallis, Zeyuan Allen-Zhu, Yuanzhi Li, Shean Wang, Lu Wang, and Weizhu Chen. LoRA: Low-rank adaptation of large language models. In *International Conference on Learning Representations*, 2022. URL <https://openreview.net/forum?id=nZeVKeeFYf9>.
- Li Hu, Matthew L. Benson, Randy D. Smith, Matthew G. Lerner, and Heather A. Carlson. Binding moad (mother of all databases). *Proteins: Structure, Function, and Bioinformatics*, 60(3):333–340, 2005. doi: 10.1002/prot.20512.

- Iliia Igashov, Hannes Stärk, Clément Vignac, Arne Schneuing, Victor Garcia Satorras, Pascal Frossard, Max Welling, Michael Bronstein, and Bruno Correia. Equivariant 3d-conditional diffusion model for molecular linker design. *Nature Machine Intelligence*, 6(4):417–427, Apr 2024. ISSN 2522-5839. doi: 10.1038/s42256-024-00815-9. URL <https://doi.org/10.1038/s42256-024-00815-9>.
- Fergus Imrie, Anthony R. Bradley, Mihaela van der Schaar, and Charlotte M. Deane. Deep generative models for 3d linker design. *Journal of Chemical Information and Modeling*, 60(4):1983–1995, Apr 2020. ISSN 1549-9596. doi: 10.1021/acs.jcim.9b01120. URL <https://doi.org/10.1021/acs.jcim.9b01120>.
- John J. Irwin, Khanh G. Tang, Jennifer Young, Chinzorig Dandarchuluun, Benjamin R. Wong, Munkhzul Khurelbaatar, Yurii S. Moroz, John Mayfield, and Roger A. Sayle. Zinc20—a free ultralarge-scale chemical database for ligand discovery. *Journal of Chemical Information and Modeling*, 60(12):6065–6073, Dec 2020. ISSN 1549-9596. doi: 10.1021/acs.jcim.0c00675. URL <https://doi.org/10.1021/acs.jcim.0c00675>.
- Ross Irwin, Alessandro Tibo, Jon Paul Janet, and Simon Olsson. Efficient 3d molecular generation with flow matching and scale optimal transport, 2024. URL <https://arxiv.org/abs/2406.07266>.
- Dejun Jiang, Chang-Yu Hsieh, Zhenxing Wang, Yue Kang, Jing Wang, Binbin Liao, Chun Shen, and Li Xu. Interaction-graphnet: A novel and efficient deep graph representation learning framework for accurate protein–ligand interaction predictions. *Journal of Medicinal Chemistry*, 64(24):18209–18232, 2021. doi: 10.1021/acs.jmedchem.1c01830.
- José Jiménez, Miha Škalič, Gerard Martínez-Rosell, and Gianni De Fabritiis. *k_DEEP*: Protein–ligand absolute binding affinity prediction via 3d-convolutional neural networks. *Journal of Chemical Information and Modeling*, 58(2):287–296, 2018. doi: 10.1021/acs.jcim.7b00650.
- Bowen Jing, Gabriele Corso, Jeffrey Chang, Regina Barzilay, and Tommi Jaakkola. Torsional diffusion for molecular conformer generation, 2023. URL <https://arxiv.org/abs/2206.01729>.
- Ryne C. Johnston, Kun Yao, Zachary Kaplan, Monica Chelliah, Karl Leswing, Sean Seekins, Shawn Watts, David Calkins, Jackson Chief Elk, Steven V. Jerome, Matthew P. Repasky, and John C. Shelley. Epik: pK_a and protonation state prediction through machine learning. *Journal of Chemical Theory and Computation*, 19(8):2380–2388, 2023. doi: 10.1021/acs.jctc.3c00044.
- Gareth Jones, Peter Willett, Robert C Glen, Andrew R Leach, and Robin Taylor. Development and validation of a genetic algorithm for flexible docking led by f. e. cohen. *Journal of Molecular Biology*, 267(3):727–748, 1997. ISSN 0022-2836. doi: <https://doi.org/10.1006/jmbi.1996.0897>. URL <https://www.sciencedirect.com/science/article/pii/S0022283696908979>.
- William L. Jorgensen. The many roles of computation in drug discovery. *Science*, 303(5665):1813–1818, 2004. doi: 10.1126/science.1096361.
- Chaitanya K. Joshi, Xiang Fu, Yi-Lun Liao, Vahe Gharakhanyan, Benjamin Kurt Miller, Anuroop Sriram, and Zachary Ward Ulissi. All-atom diffusion transformers: Unified generative modelling of molecules and materials. In *Forty-second International Conference on Machine Learning*, 2025. URL <https://openreview.net/forum?id=89QPmZjIhv>.
- Dmitry S. Karlov, Sergey Sosnin, Maxim V. Fedorov, and Petr Popov. graphdelta: Mpnn scoring function for the affinity prediction of protein–ligand complexes. *ACS Omega*, 5(10):5150–5159, 2020. doi: 10.1021/acsomega.9b04162.
- Jaihoon Kim, Taehoon Yoon, Jisung Hwang, and Minhyuk Sung. Inference-time scaling for flow models via stochastic generation and rollover budget forcing, 2025. URL <https://arxiv.org/abs/2503.19385>.
- Diederik P Kingma, Tim Salimans, Ben Poole, and Jonathan Ho. Variational diffusion models. In *Advances in Neural Information Processing Systems (NeurIPS)*, 2021.
- Peter A. Kollman, Irina Massova, Carolina Reyes, Bernd Kuhn, Shuanghong Huo, Lillian Chong, Matthew Lee, Taisung Lee, Yong Duan, Wei Wang, Oreola Donini, Piotr Cieplak, Jayaraman Srinivasan, David A. Case, and Thomas E. Cheatham. Calculating structures and free energies of complex molecules: Combining molecular mechanics and continuum models. *Accounts of Chemical Research*, 33(12):889–897, 2000. doi: 10.1021/ar000033j.
- Indrajit Kundu, Gopal Paul, and Ranjan Banerjee. A machine learning approach towards the prediction of protein–ligand binding affinity based on fundamental molecular properties. *RSC Advances*, 8(22):12127–12137, 2018. doi: 10.1039/C8RA00003D.
- Tuan Le, Julian Cremer, Frank Noé, Djork-Arné Clevert, and Kristof Schütt. Navigating the design space of equivariant diffusion-based generative models for de novo 3d molecule generation, 2023.
- Joo Youn Lee, Ji-Sook Yun, Woo-Keun Kim, Hang-Suk Chun, Hyeonseok Jin, Sungchan Cho, and Jeong Ho Chang. Structural basis for the selective inhibition of Cdc2-Like kinases by CX-4945. *Biomed Res Int*, 2019:6125068, August 2019.

- Joongwon Lee, Seonghwan Kim, and Wou Youn Kim. Fragfm: Efficient fragment-based molecular generation via discrete flow matching. *arXiv preprint*, 2025.
- Pablo Lemos, Zane Beckwith, Sasaank Bandi, Maarten van Damme, Jordan Crivelli-Decker, Benjamin J. Shields, Thomas Merth, Punit K. Jha, Nicola De Mitri, Tiffany J. Callahan, AJ Nish, Paul Abruzzo, Romelia Salomon-Ferrer, and Martin Ganahl. Sair: Enabling deep learning for protein-ligand interactions with a synthetic structural dataset. *bioRxiv*, 2025. doi: 10.1101/2025.06.17.660168. URL <https://www.biorxiv.org/content/early/2025/06/21/2025.06.17.660168>.
- Daniel S. Levine, Muhammed Shuaibi, Evan Walter Clark Spotte-Smith, Michael G. Taylor, Muhammad R. Hasyim, Kyle Michel, Ilyes Batatia, Gábor Csányi, Misko Dzamba, Peter Eastman, Nathan C. Frey, Xiang Fu, Vahe Gharakhanyan, Aditi S. Krishnapriyan, Joshua A. Rackers, Sanjeev Raja, Ammar Rizvi, Andrew S. Rosen, Zachary Ulissi, Santiago Vargas, C. Lawrence Zitnick, Samuel M. Blau, and Brandon M. Wood. The open molecules 2025 (omol25) dataset, evaluations, and models, 2025. URL <https://arxiv.org/abs/2505.08762>.
- Shuangli Li, Jingbo Zhou, Tong Xu, Liang Huang, Fan Wang, Hui Xiong, Weili Huang, and Dejing Dou. Structure-aware interactive graph neural networks for the prediction of protein–ligand binding affinity. In *Proceedings of the 27th ACM SIGKDD Conference on Knowledge Discovery and Data Mining*, pages 975–985, 2021. doi: 10.1145/3447548.3467311.
- Xuelian Li, Cheng Shen, Hui Zhu, Yujian Yang, Qing Wang, Jincai Yang, and Niu Huang. A high-quality data set of protein–ligand binding interactions via comparative complex structure modeling. *Journal of Chemical Information and Modeling*, 64(7):2454–2466, Apr 2024. ISSN 1549-9596. doi: 10.1021/acs.jcim.3c01170. URL <https://doi.org/10.1021/acs.jcim.3c01170>.
- Yan Li, Minyi Su, Zhihai Liu, Jian Li, Jie Liu, Li Han, and Renxiao Wang. Assessing protein–ligand interaction scoring functions with the casf-2013 benchmark. *Nature Protocols*, 13(4):666–680, 2018. doi: 10.1038/nprot.2017.114.
- Yaron Lipman, Ricky T. Q. Chen, Heli Ben-Hamu, Maximilian Nickel, and Matt Le. Flow matching for generative modeling. *ICLR*, 2023. arXiv:2210.02747.
- Jie Liu and Renxiao Wang. Classification of current scoring functions. *Journal of Chemical Information and Modeling*, 55(3):475–482, 2015. doi: 10.1021/ci500731a.
- Xingchao Liu, Chengyue Gong, and Qiang Liu. Flow straight and fast: Learning to generate and transfer data with rectified flow. *arXiv preprint*, 2022. arXiv:2209.03003.
- Youzhi Luo and Shuiwang Ji. An autoregressive flow model for 3d molecular geometry generation from scratch. In *International Conference on Learning Representations*, 2022. URL <https://openreview.net/forum?id=C03Ajc-NS5W>.
- Nanye Ma, Shangyuan Tong, Haolin Jia, Hexiang Hu, Yu-Chuan Su, Mingda Zhang, Xuan Yang, Yandong Li, Tommi Jaakkola, Xuhui Jia, and Saining Xie. Inference-time scaling for diffusion models beyond scaling denoising steps, 2025. URL <https://arxiv.org/abs/2501.09732>.
- James A Maier, Carmenza Martinez, Koushik Kasavajhala, Lauren Wickstrom, Kevin E Hauser, and Carlos Simmerling. ff14SB: Improving the accuracy of protein side chain and backbone parameters from ff99SB. *Journal of Chemical Theory and Computation*, 11(8):3696–3713, 2015.
- G. Manning, D. B. Whyte, R. Martinez, T. Hunter, and S. Sudarsanam. The protein kinase complement of the human genome. *Science*, 298(5600):1912–1934, 2002. doi: 10.1126/science.1075762. URL <https://www.science.org/doi/abs/10.1126/science.1075762>.
- Rocco Meli, Garrett M. Morris, and Philip C. Biggin. Scoring functions for protein–ligand binding affinity prediction using structure-based deep learning: A review. *Frontiers in Bioinformatics*, 2:885983, 2022. doi: 10.3389/fbinf.2022.885983.
- Filipe Menezes and Grzegorz M. Popowicz. Ulysses: An efficient and easy to use semiempirical library for c++. *Journal of Chemical Information and Modeling*, 62(16):3685–3694, 2022. doi: 10.1021/acs.jcim.2c00757. URL <https://doi.org/10.1021/acs.jcim.2c00757>. PMID: 35930308.
- Antonia S J S Mey, Bryce K Allen, Hannah E Bruce Macdonald, John D Chodera, David F Hahn, Maximilian Kuhn, Julien Michel, David L Mobley, Levi N Naden, Samarjeet Prasad, Andrea Rizzi, Jenke Scheen, Michael R Shirts, Gary Tresadern, and Huafeng Xu. Best practices for alchemical free energy calculations [article v1.0]. *Living J Comput Mol Sci*, 2(1), 2020.
- David L. Mobley and Pavel V. Klimovich. Perspective: Alchemical free energy calculations for drug discovery. *The Journal of Chemical Physics*, 137(23):230901, 2012.
- Farzad Molani and Art E Cho. Accurate protein-ligand binding free energy estimation using QM/MM on multi-conformers predicted from classical mining minima. *Commun Chem*, 7(1):247, October 2024.

- Thin Nguyen, Thao Minh Le, Thomas P. Quinn, Trung Nguyen, and Svetha Venkatesh. Graphdta: Predicting drug–target binding affinity with graph neural networks. *Bioinformatics*, 37(8):1140–1147, 2021. doi: 10.1093/bioinformatics/btaa921.
- Michał Nowacki, Filipe Menezes, Emilia Pykacz, Mateusz Popiołek, Valeria Napolitano, Chethan K. Krishna, Vishal C. Kalel, Ralf Erdmann, Tony Fröhlich, Oliver Plettenburg, Michael Sattler, Grzegorz M. Popowicz, and Maciej Dawidowski. Quantum mechanics-driven structure-activity relationship study of pex5-pex14 protein-protein interaction inhibitors based on a dibenzo[b,e]azepin-6(6h)-one scaffold. *European Journal of Medicinal Chemistry*, 298:117979, 2025. ISSN 0223-5234. doi: <https://doi.org/10.1016/j.ejmech.2025.117979>. URL <https://www.sciencedirect.com/science/article/pii/S0223523425007445>.
- Noel M. O’Boyle, Michael Banck, Craig A. James, Chris Morley, Tim Vandermeersch, Pierre Hutchison, Geoffrey R. Del Moral, Arnaud Doucet, and Ajay Jasra. Open babel: An open chemical toolbox. *Journal of Cheminformatics*, 3(33):1758–2946, 2011. doi: 10.1186/1758-2946-3-33.
- OpenEye Scientific Software. OMEGA. <https://docs.eyesopen.com/applications/omega/>, a.
- OpenEye Scientific Software. ROCS. <https://docs.eyesopen.com/applications/rocs/>, b.
- OpenEye Scientific Software. Szybki. <https://docs.eyesopen.com/applications/szybki/>, c.
- OpenEye Scientific Software. OEDocking. <https://www.eyesopen.com/oedocking-tk>, d.
- OpenFE. IndustryBenchmarks2024. <https://github.com/OpenFreeEnergy/IndustryBenchmarks2024>, a.
- OpenFE. IndustryBenchmarks2024. <https://omsf.substack.com/p/the-free-energy-of-everything-benchmarking-openfe>, b.
- Hakime Öztürk, Arzucan Özgür, and E. Ozkirimli. Deepdta: Deep drug–target binding affinity prediction. *Bioinformatics*, 34(17):i821–i829, 2018. doi: 10.1093/bioinformatics/bty593.
- Saro Passaro, Gabriele Corso, Jeremy Wohlwend, Mateo Reveiz, Stephan Thaler, Vignesh Ram Somnath, Noah Getz, Tally Portnoi, Julien Roy, Hannes Stark, David Kwabi-Addo, Dominique Beaini, Tommi Jaakkola, and Regina Barzilay. Boltz-2: Towards accurate and efficient binding affinity prediction. *bioRxiv*, 2025. doi: 10.1101/2025.06.14.659707. URL <https://www.biorxiv.org/content/early/2025/06/18/2025.06.14.659707>.
- Goran Paulin and Marina Ivašić-Kos. Review and analysis of synthetic dataset generation methods and techniques for application in computer vision. *Artificial Intelligence Review*, 56:9221–9265, 2023. doi: 10.1007/s10462-022-10358-3.
- Adam Pecina, Jindřich Fanfrlík, Martin Lepšík, and Jan Řezáč. Sqm2.20: Semiempirical quantum-mechanical scoring function yields dft-quality protein–ligand binding affinity predictions in minutes. *Nature Communications*, 15:1127, 2024.
- Lucas Francisco Amaral Orosco Pellicer, Taynan Maier Ferreira, and Anna Helena Reali Costa. Data augmentation techniques in natural language processing. *Applied Soft Computing*, 132:109803, 2023. doi: 10.1016/j.asoc.2022.109803.
- Danny Reidenbach, Filipp Nikitin, Olexandr Isayev, and Saeed Gopal Paliwal. Applications of modular co-design for de novo 3d molecule generation. In *NeurIPS 2024 Workshop on AI for New Drug Modalities*, 2024. URL <https://openreview.net/forum?id=KNTyaCNG7Y>.
- Jean-Louis Reymond, Ruben van Deursen, Lorenz C. Blum, and Lars Ruddigkeit. Chemical space as a source for new drugs. *MedChemComm*, 1:30–38, 2010. doi: 10.1039/C0MD00020E.
- Benjamin Ries, Irfan Alibay, Nithishwer Mouroug Anand, Philip C. Biggin, and Aniket Magarkar. Automated absolute binding free energy calculation workflow for drug discovery. *Journal of Chemical Information and Modeling*, 64(14):5357–5364, Jul 2024. ISSN 1549-9596. doi: 10.1021/acs.jcim.4c00343. URL <https://doi.org/10.1021/acs.jcim.4c00343>.
- Robin Rombach, Andreas Blattmann, Dominik Lorenz, Patrick Esser, and Björn Ommer. High-resolution image synthesis with latent diffusion models. In *CVPR*, 2022. arXiv:2112.10752.
- Gregory A. Ross, Chao Lu, Guido Scarabelli, Steven K. Albanese, Evelyne Houang, Robert Abel, Edward D. Harder, and Lingle Wang. The maximal and current accuracy of rigorous protein-ligand binding free energy calculations. *Communications Chemistry*, 6(1):222, Oct 2023a. ISSN 2399-3669. doi: 10.1038/s42004-023-01019-9. URL <https://doi.org/10.1038/s42004-023-01019-9>.
- Gregory A. Ross, Chao Lu, Guido Scarabelli, and Lingle Wang. The maximal and current accuracy of rigorous protein–ligand binding free energy calculations. *Communications Chemistry*, 6:222, 2023b. doi: 10.1038/s42004-023-01019-9.

- G. Madhavi Sastry, Matvey Adzhigirey, Tyler Day, Ramakrishna Annabhimoju, and Woody Sherman. Protein and ligand preparation: parameters, protocols, and influence on virtual screening enrichments. *Journal of Computer-Aided Molecular Design*, 27(3):221–234, 2013. doi: 10.1007/s10822-013-9644-8.
- Jack Scantlebury, Lucy Vost, Adam Carbery, Tristan E. Hadfield, Oliver M. Turnbull, Nathan Brown, Vijil Chenthamarakshan, Payel Das, Hugues Grosjean, Frank von Delft, and Charlotte M. Deane. A small step toward generalizability: Training a machine learning scoring function for structure-based virtual screening. *Journal of Chemical Information and Modeling*, 63(10):2960–2974, 2023. doi: 10.1021/acs.jcim.3c00322.
- Arne Schneuing, Yuanqi Du, Charles Harris, Arian Jamasb, Ilia Igashov, Weitao Du, Tom Blundell, Pietro Lió, Carla Gomes, Max Welling, Michael Bronstein, and Bruno Correia. Structure-based drug design with equivariant diffusion models, 2023. URL <https://arxiv.org/abs/2210.13695>.
- Arne Schneuing, Ilia Igashov, Adrian W. Dobbelstein, Thomas Castiglione, Michael M. Bronstein, and Bruno Correia. Multi-domain distribution learning for de novo drug design. In *The Thirteenth International Conference on Learning Representations*, 2025. URL <https://openreview.net/forum?id=g3VCIM94ke>.
- Kristof T. Schütt, Oliver T. Unke, and Michael Gastegger. Equivariant message passing for the prediction of tensorial properties and molecular spectra, 2021. URL <https://arxiv.org/abs/2102.03150>.
- Amrith Setlur, Chirag Nagpal, Adam Fisch, Xinyang Geng, Jacob Eisenstein, Rishabh Agarwal, Alekh Agarwal, Jonathan Berant, and Aviral Kumar. Rewarding progress: Scaling automated process verifiers for llm reasoning, 2024. URL <https://arxiv.org/abs/2410.08146>.
- Raghav Singhal, Zachary Horvitz, Ryan Teehan, Mengye Ren, Zhou Yu, Kathleen McKeown, and Rajesh Ranganath. A general framework for inference-time scaling and steering of diffusion models. In *Forty-second International Conference on Machine Learning*, 2025. URL <https://openreview.net/forum?id=Jp988ELppQ>.
- Charlie Snell, Jaehoon Lee, Kelvin Xu, and Aviral Kumar. Scaling llm test-time compute optimally can be more effective than scaling model parameters, 2024. URL <https://arxiv.org/abs/2408.03314>.
- Jascha Sohl-Dickstein, Eric Weiss, Niru Maheswaranathan, and Surya Ganguli. Deep unsupervised learning using nonequilibrium thermodynamics. In *International conference on machine learning*, pages 2256–2265. PMLR, 2015.
- Yang Song, Jascha Sohl-Dickstein, Diederik P. Kingma, Abhishek Kumar, Stefano Ermon, and Ben Poole. Score-based generative modeling through stochastic differential equations. *ICLR*, 2021. arXiv:2011.13456.
- W. Clark Still, Anna Tempczyk, Ronald C. Hawley, and Thomas Hendrickson. Semianalytical treatment of solvation for molecular mechanics and dynamics. *Journal of the American Chemical Society*, 112(16):6127–6129, 1990. doi: 10.1021/ja00172a038.
- Minyi Su, Qifan Yang, Yun Du, Guoli Feng, Zhihai Liu, Yan Li, and Renxiao Wang. Comparative assessment of scoring functions: The casf-2016 update. *Journal of Chemical Information and Modeling*, 59(2):895–913, 2019. doi: 10.1021/acs.jcim.8b00545.
- Jian Tang, Andrzej Szwajda, Shweta Shakyawar, Tianyun Xu, Pekka Hintsanen, Krister Wennerberg, and Tero Aittokallio. Drug–target interaction prediction with the kiba dataset. *PLoS Computational Biology*, 10(12):e1003765, 2014a. doi: 10.1371/journal.pcbi.1003765.
- Jian Tang, Andrzej Szwajda, Sumeet Shakyawar, Tianyun Xu, Perttu Hintsanen, Krister Wennerberg, and Tero Aittokallio. Making sense of large-scale kinase inhibitor bioactivity data sets: A comparative and integrative analysis. *Journal of Chemical Information and Modeling*, 54(3):735–743, 2014b. doi: 10.1021/ci400709d.
- Alexander Tong, Kilian FATRAS, Nikolay Malkin, Guillaume Hugué, Yanlei Zhang, Jarrid Rector-Brooks, Guy Wolf, and Yoshua Bengio. Improving and generalizing flow-based generative models with minibatch optimal transport. *Transactions on Machine Learning Research*, 2024. ISSN 2835-8856. URL <https://openreview.net/forum?id=CD9Snc73AW>.
- Jos Torge, Charles Harris, Simon V. Mathis, and Pietro Lió. Diffhopp: A graph diffusion model for novel drug design via scaffold hopping. In *ICML Workshop on Computational Biology*, 2023.
- Andreas Tosstorff, Markus G. Rudolph, Jason C. Cole, Michael Reutlinger, Christian Kramer, Hervé Schaffhauser, Agnès Nilly, Alexander Flohr, and Bernd Kuhn. A high quality, industrial data set for binding affinity prediction: performance comparison in different early drug discovery scenarios. *Journal of Computer-Aided Molecular Design*, 36(10):753–765, 2022. doi: 10.1007/s10822-022-00478-x.
- Oleg Trott and Arthur J. Olson. Autodock vina: improving the speed and accuracy of docking with a new scoring function, efficient optimization, and multithreading. *Journal of Computational Chemistry*, 31(2):455–461, 2010.

- Ísak Valsson, Matthew T. Warren, Charlotte M. Deane, Aniket Magarkar, Garrett M. Morris, and Philip C. Biggin. Narrowing the gap between machine learning scoring functions and free energy perturbation using augmented data. *Communications Chemistry*, 8(1):41, Feb 2025. ISSN 2399-3669. doi: 10.1038/s42004-025-01428-y. URL <https://doi.org/10.1038/s42004-025-01428-y>.
- Clément Vignac, Nagham Osman, Laura Toni, and Pascal Frossard. Midi: Mixed graph and 3d denoising diffusion for molecule generation. In *Machine Learning and Knowledge Discovery in Databases: Research Track - European Conference, ECML PKDD 2023, Turin, Italy, September 18-22, 2023, Proceedings, Part II*, volume 14170 of *Lecture Notes in Computer Science*, pages 560–576. Springer, 2023. doi: 10.1007/978-3-031-43415-0_33. URL https://doi.org/10.1007/978-3-031-43415-0_33.
- Mikhail Volkov, James A. Turk, Nicolas Drizard, Nicolas Martin, Bernd Hoffmann, Martine Stahl, Nikolay P. Todorov, Gianni De Fabritiis, John D. Chodera, Gilles Marcou, and Didier Rognan. On the frustration to predict binding affinities from protein–ligand structures with deep neural networks. *Journal of Medicinal Chemistry*, 65(11): 7946–7958, 2022. doi: 10.1021/acs.jmedchem.2c00487.
- Sergei Voloboev. A review on fragment-based de novo 2d molecule generation. *arXiv preprint*, 2024.
- Chenyang Wang, Shiqi Xu, Yiheng Wang, et al. Molcraft: Structure-based drug design in continuous parameter space. *arXiv preprint*, 2024. arXiv:2404.12141.
- Lingle Wang, Yujie Wu, Yuqing Deng, Byungchan Kim, Levi Pierce, Goran Krilov, Dmitry Lupyan, Shaughnessy Robinson, Markus K. Dahlgren, Jeremy Greenwood, Donna L. Romero, Craig Masse, Jennifer L. Knight, Thomas Steinbrecher, Thijs Beuming, Wolfgang Damm, Ed Harder, Woody Sherman, Mark Brewer, Ron Wester, Mark Murcko, Leah Frye, Ramy Farid, Teng Lin, David L. Mobley, William L. Jorgensen, Bruce J. Berne, Richard A. Friesner, and Robert Abel. Accurate and reliable prediction of relative ligand binding potency in prospective drug discovery by way of a modern free-energy calculation protocol and force field. *Journal of the American Chemical Society*, 137(7):2695–2703, Feb 2015. ISSN 0002-7863. doi: 10.1021/ja512751q. URL <https://doi.org/10.1021/ja512751q>.
- Renxiao Wang, Xueliang Fang, Yipin Lu, Chao-Yie Yang, and Shaomeng Wang. The pdbbind database: methodologies and updates. *Journal of medicinal chemistry*, 48(12):4111–4119, 2005.
- Yingze Wang, Kunyang Sun, Jie Li, Xingyi Guan, Oufan Zhang, Dorian Bagni, Yang Zhang, Heather A. Carlson, and Teresa Head-Gordon. A workflow to create a high-quality protein–ligand binding dataset for training, validation, and prediction tasks. *Digital Discovery*, 4:1209–1220, 2025. doi: 10.1039/D4DD000357H. URL <http://dx.doi.org/10.1039/D4DD000357H>.
- Jeremy Wohlwend, Gabriele Corso, Saro Passaro, Mateo Reveiz, Ken Leidal, Wojtek Swiderski, Tally Portnoi, Itamar Chinn, Jacob Silterra, Tommi Jaakkola, and Regina Barzilay. Boltz-1 democratizing biomolecular interaction modeling. *bioRxiv*, 2024. doi: 10.1101/2024.11.19.624167. URL <https://www.biorxiv.org/content/early/2024/11/20/2024.11.19.624167>.
- Maciej Wójcikowski, Michał Kukielka, Marta M. Stepniewska-Dziubińska, and Paweł Siedlecki. Development of a protein–ligand extended connectivity (plec) fingerprint and its application for binding affinity predictions. *Bioinformatics*, 35(8):1334–1341, 2019. doi: 10.1093/bioinformatics/bty757.
- Luhuan Wu, Brian L. Trippe, Christian A Naesseth, John Patrick Cunningham, and David Blei. Practical and asymptotically exact conditional sampling in diffusion models. In *Thirty-seventh Conference on Neural Information Processing Systems*, 2023. URL <https://openreview.net/forum?id=eWKqrlzcrv>.
- Ming-Hsiu Wu, Ziqian Xie, and Degui Zhi. A folding-docking-affinity framework for protein-ligand binding affinity prediction. *Communications Chemistry*, 8(1):108, Apr 2025. ISSN 2399-3669. doi: 10.1038/s42004-025-01506-1. URL <https://doi.org/10.1038/s42004-025-01506-1>.
- Minkai Xu, Lantao Yu, Yang Song, Chence Shi, Stefano Ermon, and Jian Tang. Geodiff: a geometric diffusion model for molecular conformation generation, 2022. URL <https://arxiv.org/abs/2203.02923>.
- Jincai Yang, Cheng Shen, and Niu Huang. Predicting or pretending: Artificial intelligence for protein–ligand interactions lack of sufficiently large and unbiased datasets. *Frontiers in Pharmacology*, 11:69, 2020a. doi: 10.3389/fphar.2020.00069.
- Yujia Yang, Kyle Yao, Matthew P. Repasky, Karl Leswing, Robert Abel, Brian K. Shoichet, and Spencer V. Jerome. Efficient exploration of chemical space with docking and deep learning. *Journal of Chemical Theory and Computation*, 17(11):7106–7119, 2021. doi: 10.1021/acs.jctc.1c00793.
- Yuyao Yang, Shuangjia Zheng, Shimin Su, Chao Zhao, Jun Xu, and Hongming Chen. Syntalinker: automatic fragment linking with deep conditional transformer neural networks. *Chem. Sci.*, 11:8312–8322, 2020b. doi: 10.1039/D0SC03126G. URL <http://dx.doi.org/10.1039/D0SC03126G>.

Kiwoong Yoo, Owen Oertell, Junhyun Lee, Sanghoon Lee, and Jaewoo Kang. Turbohopp: Accelerated molecule scaffold hopping with consistency models. In *NeurIPS*, 2024.

Odin Zhang, Yufei Huang, Shichen Cheng, Mengyao Yu, Xujun Zhang, Haitao Lin, Yundian Zeng, Mingyang Wang, Zhenxing Wu, Huifeng Zhao, Zaixi Zhang, Chenqing Hua, Yu Kang, Sunliang Cui, Peichen Pan, Chang-Yu Hsieh, and Tingjun Hou. Fragg: towards 3d geometry reliable fragment-based molecular generation. *Chem. Sci.*, 15: 19452–19465, 2024. doi: 10.1039/D4SC04620J. URL <http://dx.doi.org/10.1039/D4SC04620J>.

Hui Zhu, Xuelian Li, Baoquan Chen, and Niu Huang. Augmented bindingnet dataset for enhanced ligand binding pose predictions using deep learning. *npj Drug Discovery*, 2(1):1, Jan 2025. ISSN 3005-1452. doi: 10.1038/s44386-024-00003-0. URL <https://doi.org/10.1038/s44386-024-00003-0>.

Robert W. Zwanzig. High-temperature equation of state by a perturbation method. i. nonpolar gases. *The Journal of Chemical Physics*, 22(8):1420–1426, 1954. doi: 10.1063/1.1740409.